

**Engineering the Couplings to the Continuum:  
Controlling the Fundamental Properties of  
Radiation and Enabling Forbidden Light-Matter  
Interactions**

by

Nicholas Rivera

Submitted to the Department of Physics  
in partial fulfillment of the requirements for the degree of

Bachelor of Science in Physics

at the

MASSACHUSETTS INSTITUTE OF TECHNOLOGY

June 2016

© Massachusetts Institute of Technology 2016. All rights reserved.

**Signature redacted**

Author .....

Department of Physics

May 6, 2016

**Signature redacted**

Certified by .....

Marin Soljacic

Professor of Physics and MacArthur Fellow

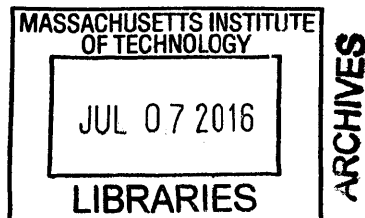
Thesis Supervisor

**Signature redacted**

Accepted by .....

Nergis Mavalvala

Senior Thesis Coordinator





**Engineering the Couplings to the Continuum: Controlling  
the Fundamental Properties of Radiation and Enabling  
Forbidden Light-Matter Interactions**

by

Nicholas Rivera

Submitted to the Department of Physics  
on May 6, 2016, in partial fulfillment of the  
requirements for the degree of  
Bachelor of Science in Physics

**Abstract**

In this thesis, I consider the general question: what new dynamics can be realized by engineering the coupling between a discrete state and a continuum of states?

In the first part of the thesis, we choose bound states in the continuum (BICs) as our starting point for answering this question. We construct a large class of BICs associated with separable Hamiltonians and show that by designing special perturbations of these systems, the dimensionality and propagation direction of waves can be controlled. We present potential realizations of this physics in potentials for ultracold atoms, optically induced potentials for photons, and lattice systems. Such resonances with easily reconfigurable radiation allows for applications such as the storage and release of waves at a controllable rate and direction and systems that switch between different dimensions of confinement.

In the second part of the thesis, we look at the same question in a different physical setting: the coupling of electrons to the electromagnetic fields of polaritons such as plasmon and phonon-polaritons. We consider the potential for 2D materials such as graphene, thin films of SiC, and hBN to enable atomic and molecular transitions that have, to this date been either very difficult to observe, or have not yet been observed.

Examples of such transitions include high-order multipolar transitions (as high as E5), multi-photon spontaneous emission, and intercombination processes such as spin-flip phosphorescence transitions. We find that plasmon polaritons in graphene can speed up spin-flip phosphorescence process by 7 orders of magnitude, that they can speed up two-photon spontaneous emission processes by 15 orders of magnitude, and that they can speed up multipolar transitions by over 20 orders of magnitude. This brings the lifetimes of all of these transitions to the nanosecond scale, comparable with the speed of the single-plasmon dipole transitions which have traditionally been thought to be the only transitions worth considering in most circumstances. The potential applications of this work include: spectroscopy for inferring electronic transitions which cannot be determined with photons, sensors based on forbidden transitions, organic-light sources arising from fast singlet-triplet transitions, fast entangled light generation, and fast generation of broadband light with tunable width in the visible or IR.

From there, we ask: is it possible to engineer couplings between an electron and its radiative continuum such that it prefers to spontaneously emit via a conventionally forbidden transition? We find an affirmative answer. In particular, we show that in these systems, it is possible to have an electron *prefer* to change its orbital angular momentum by more than one. Processes that normally take years to happen are typically considered negligible become dominant processes which happen on the scale of nanoseconds. Going beyond processes at first order, we find that it is also possible to have an electron *prefer* to decay by the emission of two near-field photons, even when it is possible for the electron to decay via the emission of a far-field photon. In the process of showing these results, we arrive at a general result connecting the enhancement of N-photon emission to the Purcell factor, which has been of fundamental importance in quantum nanophotonics. Our results have direct implications for the design of fundamentally new types of emitters in the mid and far IR: ones which

prefer to change their angular momentum by large amounts and also ones that prefer to emit a relatively broad spectrum of entangled photons. Our results may allow for the possibility of ushering in new classes of quantum emitters with tunable multipolarity and/or tunable emission spectra, in addition to new materials for broad-band absorption and emission, new capabilities for IR spectroscopy, sensing platforms, and many other applications.

Thesis Supervisor: Marin Soljacic

Title: Professor of Physics and MacArthur Fellow



## Acknowledgments

Over the past four years, I have become a better approximation to a physicist (see?). I see the world in a much different way than I used to. Approximations. Limiting cases. Physical pictures in place of complicated mathematics. Order of magnitude estimates. These are the things I think about daily now. And I have a lot of people to thank for helping me develop this beautiful way of seeing the world. In particular, I would like to thank Prof. Allan Adams (8.04), Prof. Aram Harrow (8.06), Prof. Steven Johnson (18.369), Prof. Liang Fu (8.231), and Prof. Matthew Schwartz (Phys 253a) for contributing especially to the development of these skills. You all have made me a better physicist.

But there's much more to physics than having physics skills. And that is where Prof. Marin Soljagic, my research advisor, comes in. Marin taught me to ask very critical questions about the significance of the calculations that I do and has inspired me to think about how to translate QED calculations and theorems about wave equations into potential applications. I personally find this to be one of the most fun and imaginative parts of research, and I thank him showing me this side of research.

Another person who has taught me these skills and many more is Dr. Ido Kaminer. If there's one thing that I can say he taught me (of course there are many), I would say that he taught me to "smell the roses", so to speak. In particular, talking to and working with Ido is a constant reminder to appreciate the inherent beauty that lies in physical calculations.

I could go on for about the length of the rest of the thesis discussing the way in which various people have shaped my development. But I probably shouldn't. So with that said, I would also like to acknowledge the various postdocs, graduate students, and undergraduate students who I have collaborated with, either through writing papers with them, or simply having stimulating discussions. These people include, in no particular order: Prof. John Joannopoulos, Prof. Hrvoje Buljan, Prof. Steven Johnson, Dr. Bo Zhen, Dr. Chia Wei Hsu, Dr. Xiao Lin, Josue Lopez, Francisco Machado, Hengyun (Harry) Zhou, Jamison Sloan, Cyuan-Han (Kenny) Chang, and

Chitraang Murdia. Last, but not least, I would like to acknowledge my family and friends for always supporting me in my endeavors.

I acknowledge the various agencies which have financially supported me as an undergraduate and will financially support me as a graduate student: the Materials Processing Center, the Center for Materials Science and Engineering, the MIT Energy Initiative, the Institute for Soldier Nanotechnology, the MIT UROP office, the School of Science, and finally the Department of Energy.



# Contents

<b>1</b>	<b>Introduction</b>	<b>21</b>
<b>2</b>	<b>Separable Bound States in the Continuum: Controlling the Directionality and Dimensionality of Radiation</b>	<b>25</b>
2.1	Introduction . . . . .	25
2.2	General Condition for Separable BICs . . . . .	26
2.3	Properties of the Degenerate Continua . . . . .	28
2.4	Proposals for the experimental realizations of separable BICs . . . . .	32
2.5	Summary . . . . .	36
<b>3</b>	<b>2D Plasmonics: Shrinking the Wavelength of Light to Allow Forbidden Transitions</b>	<b>37</b>
3.1	Introduction . . . . .	37
3.2	2D Plasmons and Light-Matter Interaction: Model and Assumptions	40
3.3	Multipolar Transitions . . . . .	44
3.4	Spin Flip Transitions and the Singlet-to-Triplet Transition . . . . .	47
3.5	Two-Plasmon Spontaneous Emission . . . . .	50
3.6	Summary and Outlook . . . . .	53
<b>4</b>	<b>Phonon Polaritons: Turning Forbidden Transitions into Dominant Transitions</b>	<b>57</b>
4.1	Introduction . . . . .	57

4.2	Quantum Electrodynamics of Phonon Polaritons and General Scheme for High-Efficiency Forbidden Transitions . . . . .	59
4.3	Phonon-polaritons allow for creating preferentially non-dipolar emitters	62
4.4	Phonon-polaritons allow for creating emitters which preferentially emit entangled pairs of photons with a highly tunable frequency and angular spectrum . . . . .	65
4.5	Summary . . . . .	70
<b>5</b>	<b>Summary and Outlook</b>	<b>73</b>
<b>A</b>	<b>Light-Matter Interactions in Photonics: Macroscopic Quantum Electrodynamics</b>	<b>79</b>
A.1	Maxwell's Equations: Basic Properties . . . . .	80
A.2	Quantization of Lossless Electromagnetic Modes: Heuristic Approach	81
A.3	Quantization in Lossy Electromagnetic Media . . . . .	83
A.3.1	Limiting Case: A Transparency Window . . . . .	84
<b>B</b>	<b>Supplementary Materials for: Shrinking the Wavelength of Light to Allow Forbidden Transitions</b>	<b>89</b>
B.1	Introduction . . . . .	89
B.2	Macroscopic QED of 2D Conductors . . . . .	90
B.3	First Order Processes . . . . .	93
B.3.1	Electric Multipole Transitions . . . . .	93
B.3.2	Spin Flip Magnetic Multipole Transitions . . . . .	98
B.4	Second Order Processes - Intercombination Transitions and Two Plasmon Emission . . . . .	100
B.4.1	Electric Dipole (Intercombination) Mechanism . . . . .	100
B.4.2	Two Plasmon Spontaneous Emission . . . . .	101
B.5	Summary of Results . . . . .	107
<b>C</b>	<b>Supplementary Materials for: Turning Forbidden Transitions into Dominant Transitions</b>	<b>109</b>

C.1	Introduction . . . . .	109
C.2	Optical Response of Phonon-Polariton Materials . . . . .	111
C.2.1	Lossless Limit: Effective Mode Expansion . . . . .	112
C.3	Macroscopic QED of PhPs at First Order in Perturbation Theory . .	113
C.4	Macroscopic QED at Higher Order in Perturbation Theory: Emission of N Polaritons . . . . .	114
C.4.1	N=2 and the Angular Spectrum of Emitted Radiation. . . . .	116
<b>D</b>	<b>List of Related Publications</b>	<b>131</b>



# List of Figures

2-1	<b>Concept of Separable BICs.</b> A schematic illustration demonstrating the concept of a separable BIC in two dimensions. . . . .	27
2-2	<b>Controlling the Directionality of Radiation with Separable BICs.</b> (a) A separable potential which is a sum of a purely $x$ -dependent Gaussian well and a purely $y$ -dependent Gaussian well. (b) The relevant states of the spectrum of the $x$ -potential, $y$ -potential, and total potential. (c) A BIC supported by this double well. (d,e) Continuum states degenerate in energy to the BIC. (f) A $y$ -delocalized continuum state resulting from an even- $y$ -parity perturbation of the BIC supporting potential. (g). An $x$ -delocalized continuum state resulting from an odd- $x$ -parity perturbation. . . . .	29
2-3	<b>Proposals for Realizations of Separable BICs.</b> (a) A photorefractive optical crystal whose index is weakly modified by two detuned intersecting light sheets with different intensities. (b) An optical potential formed by the intersection of three slightly detuned light sheets with different intensities. (c) A tight-binding lattice. . . . .	33
3-1	<b>2D Plasmons Coupled to an Emitter.</b> A schematic of an emitter (not-necessarily dipolar) above a 2D material of conductivity $\sigma(\omega)$ supporting plasmons with wavelength, $\lambda_{pl}$ far shorter than the photon wavelength, $\lambda_0$ (by a factor of $\eta_0$ ) and approaching the atomic size, $a_0$ . . . . .	40

3-2	<p><b>Convergence of the Multipoles.</b> (a) Rates of radiation into surface plasmons for various multipolar transitions in Hydrogen. The transition series considered here is <math>6\{p, d, f, g, h\} \rightarrow 4s</math>. The emitter is situated 5 nm above the surface of graphene. (b). Total rates (radiative + non-radiative) of decay for the same transition series in Hydrogen. Dashed lines show radiative rates, which agree with the total rates at high confinement. . . . .</p>	43
3-3	<p><b>Enabling singlet to triplet transitions.</b> Purcell factors for a dipolar singlet-triplet transition as a function of confinement factor <math>\eta_0</math> for (a,b) plasmons in graphene and (c,d) plasmons in 2D silver, for different atom-plane separations, <math>z_0</math> and quality factors, <math>Q</math>. These results also apply to other kinds of intercombination transitions, such as those in which the spin of an atomic emitter is flipped due to radiation. . .</p>	48
3-4	<p><b>Enabling Two-Plasmon Radiative Energy Transfer.</b> (a) Emission spectrum of two-plasmon spontaneous emission (2PSE) as a function of frequency and atom-surface separation for the Hydrogen <math>4s \rightarrow 3s</math> transition above Graphene. <math>\eta_0</math> is chosen to be 150. (b). Line-cuts of (a) for atom-surface separations of 0, 5, and 15 nm. (c) Total decay rate (in <math>\text{sec}^{-1}</math>) for this transition as a function of confinement and atom-surface separation. (d) Comparison of two-plasmon emission rate to the emission rate for a single plasmon <math>4s \rightarrow 3p</math> transition as a function of confinement and separation. . . . .</p>	56

- 4-1 **General scheme for accessing forbidden transitions at very high efficiency:** (Left) Typical situation for an emitter (even when coupled to plasmons): an emitter may have many choices for a transition, but the relatively high-frequency single-photon dipole transition is chosen. (Right) When coupling that same excited electron to SPhPs in a (potentially anisotropic) polar dielectric, the electron can be made to prefer a forbidden transition in the IR (e.g; two-polariton spontaneous emission). . . . . 60
- 4-2 **High-Efficiency Access to Multipolar Transitions:** Comparison of the potential for phonon-polariton materials to force an electron to prefer decay via multipolar transitions in hBN (hyperbolic) and SiC (non-hyperbolic). (a,d) Purcell factors for a z-polarized dipole 10 nm away from hBN (a)/SiC (d), which is used to estimate the rates of competing dipole transitions. (b, e) Decay rates for multipolar transitions E1-E5 for an emitter 8 and 10 nm away from the surface of hBN (b)/SiC (e).(c,f) Radiative efficiencies of multipolar transitions in hBN (c) and SiC (f) for an emitter 10 nm away from the surface. . 62
- 4-3 **Making two-polariton emission dominant through phonon-polaritons.** (a) Purcell spectra for a z-polarized dipole above cBN at atom-surface separations of 5, 10, and 25 nm. (b, c, d). Two-photon Purcell spectra for a spherical emitter as a function of photon frequency  $\omega$  for the same set of atom-surface separations. Blue denotes the Purcell spectra with losses accounted for and the orange denotes the Purcell spectra with 100x weaker losses. In each of (b,c,d) both the overall two-photon transition rate between the 5s and 4s states of hydrogen and the radiative ratio of the transition are noted. . . . . 65

4-4	<b>General Features of Two-Polariton Emission: Purcell Spectra.</b> Two-polariton Purcell spectra defined as in Equation (3) for a spherical emitter as a function of emitter frequency (1600 (left), 2300 (center), and 3000 (right) $\text{cm}^{-1}$ ) and emitter separation (5 (top), 10 (center), and 15 (bottom) nm). Hyperbolicity allows for enhancement over a large range of frequencies compared to isotropic systems. Moreover, distance can be used to tune the width of the spectrum. . . . .	66
4-5	<b>Wavefunction shaping and the Angular Spectrum of Entangled Radiation:</b> Plots of the angular spectrum $S(\omega_0/2, \theta, \theta')$ as a function of the initial state of the electron for initial states $s, d_{xy}, d_{xz}, d_{yz}$ . 67	67
B-1	Comparison of matrix elements computed exactly (solid) with polynomial approximations (dashed) for different transitions in the Hydrogen $5 \leftrightarrow 6$ transition series as a function of $\eta_0$ for $\lambda_0 = 7.45\mu\text{m}$ . These curves overlap completely in this range. . . . .	94
B-2	<b>Ratio of total decay rate to decay rate into plasmons - Multipolarity and Confinement Dependence:</b> plotted as a function of on-resonance confinement factor $\eta_0$ at different atom-surface separations for E(1-5) transitions in the Hydrogen $6 \leftrightarrow 5$ transition series. The minimum confinement factor considered in this figure is 20. . . .	96
B-3	<b>Effect of Confinement and Multipolarity on Radiative and Non-Radiative Decay Rates:</b> Integrand of Eq. (14) plotted for dipole (top), quadrupole (middle), and octupole (bottom) transitions at three different on-resonance confinements ( $\eta_0 = \{25, 100, 300\}$ ) and atom-surface separations ( $z_0 = \{5 \text{ nm}, 10 \text{ nm}, 15 \text{ nm}\}$ ). . . . .	97



**B-4 Effect of Losses on Two Plasmon Spontaneous Emission:** Differential decay rate  $d\Gamma/dy$  plotted as a function of  $y$  for lossless (dashed blue) and lossy (solid orange) 2D conductors. A Drude model to describe Graphene is assumed. The lossless version of these differential decay plots are plotted for the same transition as Fig. 4b in the main text. . . . . 106



# List of Tables

- 3.1 A summary of derived scalings of rates and rate enhancements for emitters on top of lossless 2D plasmons at zero displacement from the plasmon supporting surface. The rates for an emitter at finite distance from the plasmon are suppressed by  $e^{-2\eta_0 k z_0}$ , which is of order unity for an emitter within a reduced plasmon wavelength of the surface. Note that these scalings are still a good approximation even in the presence of high losses provided that the confinement is large, as shown in Fig. 2. 53
  
- 4.1 A summary of the dependence of the angular spectrum of two-polariton radiation as a function of initial and final electronic states for a few selected initial electronic states. . . . . 70



# Chapter 1

## Introduction

One of the most fundamental and general processes in quantum mechanics and in the physics of waves is one in which a state couples to a continuum of states through a perturbation. Abstract as it may sound, it underlies the description of a diverse set of scattering and decay processes such as Rayleigh scattering, Compton scattering, Bremsstrahlung, Cerenkov radiation, absorption, spontaneous emission, stimulated emission, radioactive decay, autoionization of atoms and many others. Because of this, the coupling of states to a continuum of underlies the description of atomic spectra, the color of the sky, the production of X-ray sources, and the scattering experiments which reveal the fundamental nature of our universe.

From the examples above, it should be clear that a lot of physics comes out of states coupling to continua. It sounds plausible then that if we can engineer the coupling between a state and its continua, we can change the nature of seemingly fixed fundamental processes, like the rate at which an atom spontaneously emits light.

In fact, people as far back as Purcell knew this. In his 1946 paper, he showed that the decay rate of excited electrons due to spontaneous emission can be substantially (20 orders of magnitude!) be reduced by coupling the electrons to small metallic nanoparticles. Purcell claimed that this mechanism couple potentially allow for atoms to spontaneously emit light at radio frequencies. That is *remarkable* because in free

space, the spontaneous emission rate of a dipole scales as  $\omega^3$ , making it negligible compared to spontaneous emission at vis-UV frequencies. The modification of spontaneous emission rates due to photonic structures is known to this day as the Purcell effect. The Purcell effect, from a high level, can be seen as a consequence of modifying the continuum of electromagnetic modes (photons) that an excited electron can couple to. This modification can come from modifying the wavelength, polarization, or even phase profile of the photon.

Despite the significance of Purcell's claim, it was a subject of comparatively little interest for roughly another 50 years. What happened in the 1990s? The rise of nanophotonics (and in particular, the discovery and development of nanophotonic platforms). Nanophotonics refers to the discipline that studies light (both classically and quantum mechanically) that is confined on the scale of nanometers (10 nm - 1000 nm). As we will now show, the recent developments of nanophotonics allow for the ability to modify light-matter interactions that even Purcell likely would not have expected.

In this thesis, we ask the question: *what physics can be realized by engineering the coupling between a state and its degenerate continuum?* We consider applications to the Schrodinger wave equation, Maxwell's equations, and quantum electrodynamics as relevant to nanophotonics.

In chapter two, we ask this question in the context of wave equations such as the Schrodinger equation for a single particle, Maxwell's equations, and in tight-binding models of coupled resonators. In order to get analytical insights into this problem, we focus on bound states in the continuum (infinite quality factor cavities) in systems with separable wave operators. We show for the first time that by applying tailored perturbations to these separable BICs, one can control not only the directionality of radiation but also the dimensionality of it. This may potentially lead to applications such as switches which trap waves and release them in controllable directions and

devices that can be switched between quantum dot, quantum well, and quantum wire modes of operation.

In the second part of this thesis (chapters three and four), we consider this question in the context of quantum electrodynamics, and in particular, the spontaneous emission of polaritons such as plasmon and phonon polaritons. In these parts of the thesis, the engineering of the coupling to the continuum is arising by swapping out coupling to free-space photons by coupling to polaritons (i.e; near-field photons), which are quanta of evanescent waves that can exist in dielectrics with negative permittivity.

In chapter three, we develop the general theory of light-matter interactions with 2D systems that support plasmons, exploring multipolar transitions, spin-flip transitions, and multi-photon emission processes for the first time. This theory reveals that conventionally forbidden light-matter interactions, such as extremely high-order multipolar transitions, two-plasmon spontaneous emission, and singlet-triplet phosphorescence processes can occur on very short time-scales - comparable to those of conventionally fast transitions. In fact, transitions whose normal lifetimes are on the order of the age of the universe can be made to happen in nanosecond time scales. This is the first report of such a drastic violation of the electronic selection rules (for the emission of light) over a broad range of frequencies and in atomic-scale emitters. Our findings enable new platforms for spectroscopy, sensing, broadband light generation, a potential testing ground for quantum electrodynamics in the ultrastrong coupling regime, and most generally the ability to take advantage of the full electronic spectrum of an emitter.

In the last part of the thesis (chapter four), we develop a general theory of the interactions between excited electrons and phonon-polaritons. Surface phonon polaritons are hybrid modes of photons and optical phonons that can propagate on the surface of a polar dielectric. These polaritons have generated significant excitement over the past couple of years due to their very high confinement, weak dissipation, and

narrow bandwidth. We show that the precise combination of confinement and bandwidth offered by surface phonon polaritons allows for the unprecedented ability to take forbidden transitions and turn them into dominating transitions. In particular, we show that high-order multipolar transitions, and two-photon emission processes can happen with quantum efficiencies above 90%, as opposed to a value in free-space of order  $10^{-10}\%$ . In the process of showing these results, we arrive at a general result connecting the enhancement of N-photon emission to the Purcell factor, which has been of fundamental importance in quantum nanophotonics. Our results have direct implications for the design of fundamentally new types of emitters in the mid and far IR: ones which prefer to change their angular momentum by large amounts and also ones that prefer to emit a relatively broad spectrum of entangled photons. This is the first report of a method by which to take a very wide range forbidden radiative transitions and turn them into dominant transitions.

The machinery by which we perform our analysis in chapter three and four is that of macroscopic quantum electrodynamics. Macroscopic QED is a formalism by which to quantize the fields in a dielectric medium which may be inhomogeneous, dissipative, dispersive, and anisotropic. The validity of this approach comes from experiments in cavity QED and verification of the Purcell effect in plasmonic cavities. We discuss field quantization in the general case, and in the low-loss case in Appendix A. The primary type of calculation that we perform in chapters three and four are decay rate calculations beyond the dipole approximation and at higher-order in quantum mechanical perturbation theory. These calculations are in general lengthy and not particularly illuminating, and so we relegate the detailed derivations to appendices (B and C, corresponding to chapters three and four). In chapters three and four, we focus on the intuition for the equations we derive, and the physical consequences of these equations.



# Chapter 2

## Separable Bound States in the Continuum: Controlling the Directionality and Dimensionality of Radiation

### 2.1 Introduction

In most wave systems which support bound states, the bound states do not exist at the same frequency as the delocalized waves. However, there exist special systems for which a bound state can be embedded inside a continuum of delocalized waves [1]. Such bound states in the continuum (BICs) do not forbid coexistence with propagating waves at the same frequency, unlike traditional methods of localizing waves such as conventional potential wells in quantum mechanics, conducting mirrors in optics, band-gaps in periodic systems, and Anderson localization. BICs were first shown to exist predicted theoretically in quantum mechanics by von Neumann and Wigner [2]. However, their BIC-supporting potential was highly oscillatory and

could not be implemented in reality. More recently, other examples of BICs have been proposed theoretically in quantum mechanics [3, 4, 5, 6, 7, 8, 9, 10], electromagnetism [11, 12, 13, 14, 15, 16, 17, 18, 19, 20, 21, 22, 23, 24], acoustics [17], and water waves [25], with some experimentally realized [26, 27, 28, 29, 30, 31]. A number of mechanisms explain most examples of BICs that have been discovered [1]. One of the

Among them, BICs due to separability [4, 5, 7, 12, 13, 14, 15, 6] remain relatively unexplored with a scattered literature. In this paper, we develop the most general properties of separable BICs - by providing the general criteria for the their existence of separable BICs and by characterizing the continua of these BIC-supporting systems. By doing so, we reveal properties that may lead to novel applications. *In particular, our key result is that separable BICs enable control over both the directionality and the dimensionality of resonantly emitted waves by exploiting symmetry, which is not possible in other classes of BICs.* Our findings may lead to applications such as: a new class of tunable- $Q$  directional resonators and quantum systems which can be switched between quantum dot (0D), quantum wire (1D), and quantum well (2D) modes of operation. We provide experimentally realizable examples of separable BICs in photonic systems with directionally resonant states, as well as examples in optical potentials for cold atoms. The construction of these examples has two purposes. The first is to show that it is possible to construct experimentally realistic examples of separable BICs. The second being to is experiments in the direction of realizing platforms to control the directionality and dimensionality of radiation.

## 2.2 General Condition for Separable BICs

For instructional purposes, we start by reviewing a simple example of a two-dimensional separable system - one where the Hamiltonian operator can be written as a sum of

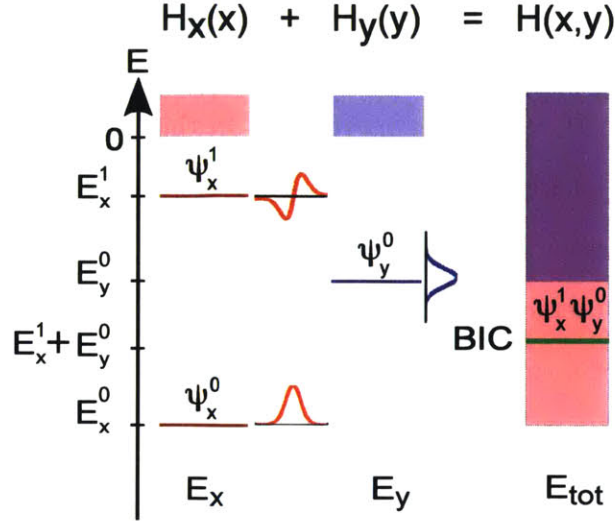


Figure 2-1: **Concept of Separable BICs.** A schematic illustration demonstrating the concept of a separable BIC in two dimensions.

Hamiltonians that each act on distinct variables  $x$  or  $y$ , i.e;

$$H = H_x(x) + H_y(y). \quad (2.1)$$

Denoting the eigenstates of  $H_x$  and  $H_y$  as  $\psi_x^i(x)$  and  $\psi_y^j(y)$ , with energies  $E_x^i$  and  $E_y^j$ , it follows that  $H$  is diagonalized by the basis of product states  $\psi_x^i(x)\psi_y^j(y)$  with energies  $E^{i,j} = E_x^i + E_y^j$ . If  $H_x$  and  $H_y$  each have a continuum of extended states starting at zero energy, and these Hamiltonians each have at least one bound state (with negative energy),  $\psi_x^0$  and  $\psi_y^0$ , respectively, then the continuum of  $H$  starts at energy  $\min(E_x^0, E_y^0)$ , where the 0 subscript denotes ground states. Therefore, if there exists a bound state satisfying  $E^{i,j} > \min(E_x^0, E_y^0)$ , then it is a bound state in the continuum. We schematically illustrate this condition being satisfied in Figure 1, where we illustrate a separable system in which  $H_x$  has two bound states,  $\psi_x^0$  and  $\psi_x^1$ , and  $H_y$  has one bound state,  $\psi_y^0$ . The first excited state of  $H_x$  combined with the ground state of  $H_y$ ,  $\psi_x^1\psi_y^0$ , is spatially bounded in both  $x$  and  $y$  but has a larger energy,  $E_x^1 + E_y^0$ , than the lowest continuum energy,  $E_x^0$ , and is therefore a BIC.

Now, we extend separability to a Hamiltonian with a larger number of separable degrees of freedom. The Hamiltonian can be expressed in tensor product notation as  $H = \sum_{i=1}^N H_i$ , where  $H_i \equiv I^{\otimes i-1} \otimes h_i \otimes I^{\otimes N-i}$ . In this expression,  $N$  is the number of separated degrees of freedom,  $h_i$  is the operator acting on the  $i$ -th variable, and  $I$  is the identity operator. The degrees of freedom may refer to the particles degree of freedom in a non-interacting multi-particle system, or the spatial and polarization degrees of freedom of a single-particle system. Denote the  $n_j$ th eigenstate of  $h_i$  by  $|\psi_i^{n_j}\rangle$  with energy  $E_i^{n_j}$ . Then, the overall Hamiltonian  $H$  is trivially diagonalized by the product states  $|n_1, n_2, \dots, n_N\rangle \equiv |\psi_1^{n_1}\rangle \otimes |\psi_2^{n_2}\rangle \otimes \dots \otimes |\psi_N^{n_N}\rangle$  with corresponding energies  $E = E_1^{n_1} + E_2^{n_2} + \dots + E_N^{n_N}$ . Denoting the ground state of  $h_i$  by  $E_i^0$  and defining the zeros of the  $h_i$  such that their continua of extended states start at energy zero, the continuum of the overall Hamiltonian starts at  $\min_{1 \leq j \leq N} \left( \sum_{i \neq j} E_i^0 \right)$ . Then, if the separated operators  $\{h_i\}$  are such that there exists a combination of separated bound states satisfying

$$E = \sum_{i=1}^N E_i^{n_i} > \min_{1 \leq j \leq N} \left( \sum_{i \neq j} E_i^0 \right), \quad (2.2)$$

this combined bound state is a BIC of the overall Hamiltonian. For such separable BICs, coupling to the continuum is forbidden by the separability of the Hamiltonian. By writing the most general criteria for separable BICs, we can extend the handful of examples of separable BICs [4, 5, 7, 12, 13, 14, 15, 6] to systems in three dimensions, multi-particle systems, and systems described by the tight-binding approximation, allowing for a systematic way to generate realistic physical systems supporting BICs.

## 2.3 Properties of the Degenerate Continua

*A unique property that holds for all separable BICs is that the delocalized modes degenerate to the BIC are always trapped in at least one direction.* In many cases, there are

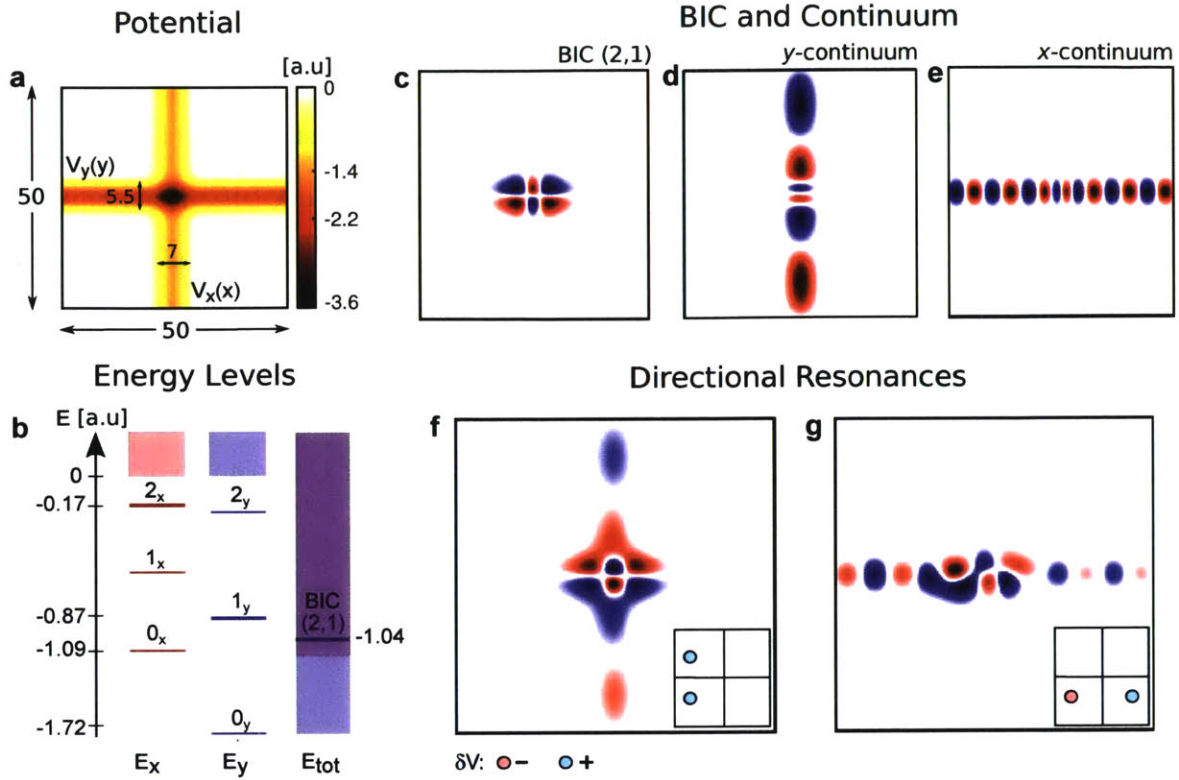


Figure 2-2: **Controlling the Directionality of Radiation with Separable BICs.**(a) A separable potential which is a sum of a purely  $x$ -dependent Gaussian well and a purely  $y$ -dependent Gaussian well. (b) The relevant states of the spectrum of the  $x$ -potential, $y$ -potential, and total potential. (c) A BIC supported by this double well. (d,e) Continuum states degenerate in energy to the BIC. (f) A  $y$ -delocalized continuum state resulting from an even- $y$ -parity perturbation of the BIC supporting potential. (g). An  $x$ -delocalized continuum state resulting from an odd- $x$ -parity perturbation.

multiple degenerate delocalized modes that are guided in different directions. When a system supporting a BIC is perturbed, this BIC generally turns into a resonance with finite lifetime. For 2D separable BICs which are perturbed into resonances, we can associate partial widths  $\Gamma_x$  and  $\Gamma_y$  to these resonances. These partial widths are the rates of coupling of the BIC to the radiation continuum (i.e., far-field) in the  $x$  and  $y$  directions under perturbation, respectively. When separability is broken, we generally can not decouple leakage in the  $x$  and  $y$  directions because the purely- $x$  and purely- $y$  delocalized continuum states mix. In this section, we show that one

can control the radiation to be towards the  $x$  (or  $y$ ) directions only, by exploiting the symmetry of the perturbation. We emphasize that although symmetry is used to realize control over directionality of radiation, separability is still generally required because the effect that we demonstrate has as the prerequisite a BIC degenerate to guided modes in different (separable) directions. As mentioned above, this is a unique property that holds for all separable BICs.

In Fig. 2(a), we show a two-dimensional potential in a Schrodinger-like equation which supports a separable BIC. This potential is a sum of Gaussian wells in the  $x$  and  $y$ -directions, given by

$$V(x, y) = -V_x e^{-\frac{2x^2}{\sigma_x^2}} - V_y e^{-\frac{2y^2}{\sigma_y^2}}. \quad (2.3)$$

This type of potential may be realized as an optical potential for ultracold atoms or a refractive index contrast profile in photonic systems. In what follows in this section, we choose arbitrary values for the parameters in the potential in Equation (3). The effects that we report can of course be observed for many other parameter choices. Solving the time-independent Schrodinger equation for  $\{V_x, V_y\} = \{1.4, 2.2\}$  and  $\{\sigma_x, \sigma_y\} = \{5, 4\}$  (in arbitrary units) gives the energy spectra shown in Fig. 2(b). This system has several BICs. Due to the  $x$  and  $y$  mirror symmetries of the system, the modes have either even or odd parity in both the  $x$  and the  $y$  directions. Here we focus on the BIC  $|n_x, n_y\rangle = |2, 1\rangle$  at energy  $E^{2,1} = -1.04$ , with the mode profile shown in Fig. 2(c); being the second excited state in  $x$  and the first excited state in  $y$ , this BIC is even in  $x$  and odd in  $y$ . It is only degenerate to continuum modes  $|0, E^{2,1} - E_x^0\rangle$  extended in the  $y$  direction (Fig. 2(d)), and  $|E^{2,1} - E_y^0, 0\rangle$  extended in the  $x$  direction (Fig. 2(e)), where an  $E$  label inside a ket denotes an extended state with energy  $E$ .

If we choose a perturbation  $\delta V$  that preserves the mirror symmetry in the  $y$ -

direction, as shown in the inset of Fig. 2(f), then the perturbed system still exhibits mirror symmetry in  $y$  but not in  $x$ . Since the BIC  $|2, 1\rangle$  is odd in  $y$  and yet the  $x$ -delocalized continuum states  $|E^{2,1} - E_y^0, 0\rangle$  are even in  $y$ , there is no coupling between the two. As a result, the perturbed state radiates only in the  $y$  direction, as shown in the calculated mode profile in Fig. 2(f). This directional coupling is a result of symmetry, and so it holds for arbitrary perturbation strengths.

On the other hand, if we apply a perturbation that is odd in  $x$  but not even in  $y$ , as shown in the inset of Fig. 2(g), then there is radiation in the  $x$  direction only to first-order in time-dependent perturbation theory. Specifically, for weak perturbations of the Hamiltonian,  $\delta V$ , the first-order leakage rate is given by Fermi's Golden Rule for bound-to-continuum coupling,  $\Gamma \sim \sum_c |\langle 2, 1 | \delta V | \psi_c \rangle|^2 \rho_c(E^{2,1})$ , where  $\rho_c(E)$  is the density of states of continuum  $c$ , and  $c$  labels the distinct continua which have states at the same energy as the BIC. Since the BIC and the  $y$ -delocalized continuum states  $|0, E^{2,1} - E_x^0\rangle$  are both even in  $x$ , the odd-in- $x$  perturbation does not couple the two modes directly, and  $\Gamma_y$  is zero to the first order. As a result, the perturbed state radiates only in the  $x$  direction, as shown in Fig. 2(g). At the second order in time-dependent perturbation theory, the BIC can make transitions to intermediate states  $k$  at any energy, and thus the second-order transition rate, proportional to  $\sum_c |T_{ci}|^2 = \sum_c \left| \sum_k \frac{\langle c | \delta V | k \rangle \langle k | \delta V | i \rangle}{E_i - E_k + i0^+} \right|^2$ , does not vanish because the intermediate state can have even parity in the  $x$ -direction. We note that although this argument relies on time-dependent perturbation theory, it is valid for any wave system provided that time evolution of the system is governed by a unitary operator and that the eigenstates of the unperturbed system form a complete basis. This is the case in the Schrodinger equation and in Maxwell's equations for lossless dielectrics.

*Another unique aspect of separability that we report here is that by using separable BICs in 3D, the number of confined dimensions of a wave can be switched between one, two, and three by tailoring perturbations applied to a single BIC mode.*

*The ability to do this allows for a device which can simultaneously act as a quantum well, a quantum wire, and a quantum dot.* We demonstrate this degree of control using a separable potential generated by the sum of three Gaussian wells (in  $x$ ,  $y$ , and  $z$  directions) of the form in Equation 2 with strengths  $\{0.4, 0.4, 1\}$  and widths  $\{12, 12, 3\}$ , all in arbitrary units. The identical  $x$  and  $y$  potentials have four bound states at energies  $E_x = E_y = -0.33, -0.20, -0.10$  and  $-0.029$ . The  $z$  potential has two bound states at energies  $E_z = -0.61$  and  $-0.059$ . The BIC state  $|1, 1, 1\rangle$  at energy  $E^{1,1,1} = -0.47$  is degenerate to twelve continuum channels:  $|0, 0, E_z\rangle, |0, 1, E_z\rangle, |1, 0, E_z\rangle, |E_x, m, 0\rangle, |n, E_y, 0\rangle$ , and  $|E_x, E_y, 0\rangle$ , where  $E_i$  denotes an energy above zero, and  $m \in \{0, 1, 2, 3\}$  and  $n \in \{0, 1, 2, 3\}$  denote bound states of the  $x$  and  $y$  wells. For perturbations which are even in the  $z$  direction, the BIC  $|1, 1, 1\rangle$  does not couple to states delocalized in  $x$  and  $y$  ( $|E_x, m, 0\rangle, |n, E_y, 0\rangle$ , and  $|E_x, E_y, 0\rangle$ ), because they have opposite parity in  $z$ , so the BIC radiates in the  $z$ -direction only. The resulting state is thus confined in two dimensions, as opposed to the BIC, which is confined in three. On the other hand, for perturbations which are even in the  $x$  and  $y$  directions, the coupling to states delocalized in  $z$  ( $|0, 0, E_z\rangle, |0, 1, E_z\rangle$ , and  $|1, 0, E_z\rangle$ ) vanishes, meaning that the BIC radiates in the  $xy$ -plane. This resulting state is confined in only in one dimension. Therefore, by tailoring perturbations to the potential, the number of confined dimensions of a wave can be switched between three, two, and one.

## 2.4 Proposals for the experimental realizations of separable BICs

BICs are generally difficult to experimentally realize because they are fragile under perturbations of system parameters. On the other hand, separable BICs are straightforward to construct and also robust with respect to changes in parameters that



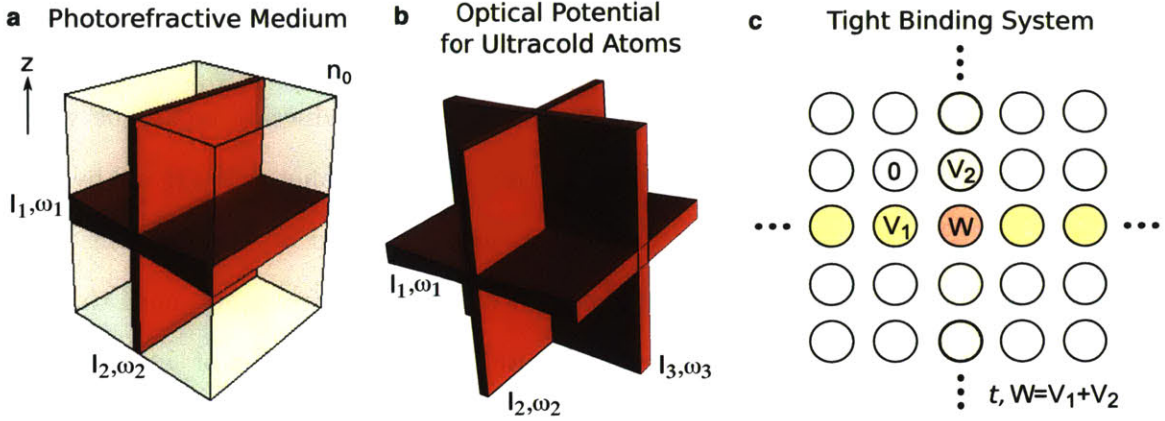


Figure 2-3: **Proposals for Realizations of Separable BICs.** (a) A photorefractive optical crystal whose index is weakly modified by two detuned intersecting light sheets with different intensities. (b) An optical potential formed by the intersection of three slightly detuned light sheets with different intensities. (c) A tight-binding lattice.

preserve the separability of the system. In the next two examples of BICs that we propose, we use detuned light sheets to generate separable potentials in photonic systems and for ultracold atoms.

*Paraxial optical systems* – As a first example of this, consider electromagnetic waves propagating paraxially along the  $z$ -direction, in an optical medium with spatially non-uniform index of refraction  $n(x, y) = n_0 + \delta n(x, y)$ , where  $n_0$  is the constant background index of refraction and  $\delta n \ll n_0$ . The slowly varying amplitude of the electric field  $\psi(x, y, z)$  satisfies the two-dimensional Schrödinger equation (see Ref. 34 and references therein),

$$i \frac{\partial \psi}{\partial z} = -\frac{1}{2k} \nabla_{\perp}^2 \psi - \frac{k \delta n}{n_0} \psi. \quad (2.4)$$

Here,  $\nabla_{\perp}^2 = \partial^2 / \partial x^2 + \partial^2 / \partial y^2$ , and  $k = 2\pi n_0 / \lambda$ , where  $\lambda$  is the wavelength in vacuum. The modes of the potential  $\delta n(x, y)$  are of the form  $\psi = A_j(x, y) e^{i\beta_j z}$ , where  $A_j$  is the profile, and  $\beta_j$  the propagation constant of the  $j$ th mode. In the simulations we use  $n_0 = 2.3$ , and  $\lambda = 485$  nm.

Experimentally, there are several ways of producing systems modeled by Equation (4) for some  $\delta n(x, y)$  ( e.g., periodic[32], random[33], and quasicrystal[34], and others). One of the very useful techniques is the optical induction technique where the potential is generated in a photosensitive material (e.g., photorefractives) by laser writing [35, 36, 37]. We consider here a potential generated by laser writing using two perpendicular light sheets, which are slightly detuned in frequency, such that the time-averaged interference vanishes and the total intensity is the sum of the intensities of the individual light sheets. The light sheets are much narrower in one dimension ( $x$  for one,  $y$  for the other) than the other two, and therefore each light sheet can be approximated as having an intensity that depends only on one coordinate, making the index contrast separable. This is schematically illustrated in Fig. 3(a). If the sheets are Gaussian along the narrow dimension, then the potential is of the form  $\delta n(x, y) = \delta n_0[\exp(-2(x/\sigma)^2) + \exp(-2(y/\sigma)^2)]$ . It is reasonable to use  $\sigma = 30 \mu\text{m}$  and  $\delta n_0 = 5.7 \times 10^{-4}$ . For these parameters, the one-dimensional Gaussian wells have four bound states, with  $\beta$  values of (in  $\text{mm}^{-1}$ ): 2.1, 1.3, 0.55, and 0.11. There are eight BICs:  $|1, 2\rangle, |2, 1\rangle, |1, 3\rangle, |3, 1\rangle, |2, 3\rangle, |3, 2\rangle, |2, 2\rangle$ , and  $|3, 3\rangle$ . Among them,  $|1, 3\rangle$  and  $|3, 1\rangle$  are symmetry protected. Additionally, the BICs  $|1, 3\rangle$  and  $|3, 1\rangle$  can be used to demonstrate directional resonance in the  $x$  or  $y$  directions, respectively, by applying perturbations even in  $x$  or  $y$ , respectively. Therefore, this photonic system serves as a platform to demonstrate both separable BICs and directional resonances.

*Optical potentials for ultracold atoms* – The next example that we consider can serve as a platform for the first experimental realization of BICs in quantum mechanics. Consider a non-interacting neutral Bose gas in an optical potential. Optical potentials are created by employing light sufficiently detuned from the resonance frequencies of the atom, where the scattering due to spontaneous emission can be neglected, and the atoms are approximated as moving in a conservative potential. As is well known experimentally, macroscopic wavefunction of the system is then de-

terminated by solving the Schrödinger equation with a potential that is proportional to the intensity of the light [38]. As an explicit example, consider an ultracold Bose gas of  $^{87}\text{Rb}$  atoms. An optical potential is produced similarly to our paraxial example by three Gaussian light sheets with equal intensity  $I_1 = I_2 = I_3$ , widths  $20\ \mu\text{m}$ , and wavelengths centered at  $\lambda = 1064\ \text{nm}$  [39]. This is schematically illustrated in Fig. 3(b). The intensity is such that this potential has depth equal to ten times the recoil energy  $E_r = \frac{\hbar^2}{2m\lambda^2}$ . By solving the Schrodinger equation numerically, we find many BICs; the continuum energy starts at a reduced energy  $\xi_c = \frac{2mEx_0^2}{\hbar^2} = -296.24$ , where  $x_0$  is chosen to be  $1\ \mu\text{m}$ . The reduced depth of the trap is  $-446.93$ . Each one-dimensional Gaussian supports 138 bound states. There are very many BICs in such a system. For concreteness, an example of one is  $|30, 96, 96\rangle$ , with reduced energy  $-146.62$ . We conclude this example by noting that in the previous section, we described a way to change the dimensionality of radiation through special perturbations in a sum of three Gaussian wells, just like the sum of three Gaussian wells considered in this example. Therefore, we propose that a shallow optical potential for ultracold atoms can be used as a platform to control the dimensionality of radiation of a macroscopic atomic wave.

*Tight Binding Models*— The final example that we consider here is an extension of the separable BIC formalism to systems which are well-approximated by a tight-binding Hamiltonian that is separable. Such systems can be experimentally achieved, as in [cite refs]. Consider the following one-dimensional tight-binding Hamiltonian,  $H_i$ , which models a one-dimensional lattice of non-identical sites:

$$H_i = \sum_k \varepsilon_i^k |k\rangle\langle k| + t_i \sum_{\langle lm \rangle} (|l\rangle\langle m| + |m\rangle\langle l|), \quad (2.5)$$

where  $\langle lm \rangle$  denotes nearest-neighbors,  $\varepsilon_i^k$  is the on-site energy of site  $k$ , and  $k, l$ , and  $m$  run from  $-\infty$  to  $\infty$ . Suppose  $\varepsilon_i^k = -V$  for  $|k| < N$ , and zero otherwise. For two

Hamiltonians of this form,  $H_1$  and  $H_2$ ,  $H = H_1 \otimes I + I \otimes H_2$  describes the lattice in Fig. 3(c). If we take  $H_1 = H_2$  with  $\{V, t, N\} = \{-1, -0.3, 2\}$ , in arbitrary units, the bound state energies of the 1D-lattices are numerically determined to be  $-0.93, -0.74, -0.46$ , and  $-0.16$ . Therefore the states  $|2, 2\rangle, |2, 3\rangle, |3, 2\rangle, |3, 3\rangle, |3, 1\rangle$  and  $|1, 3\rangle$  are BICs. The last two of these are also symmetry-protected from the continuum as they are odd in  $x$  and  $y$  while the four degenerate continuum states are always even in at least one direction. Of course, many different physical systems can be adjusted to approximate the system from Eq. (4), so this opens a path for observing separable BICs in a wide variety of systems (coupled circuits, acoustic resonators, optical resonators, etc.)

## 2.5 Summary

We have demonstrated two new properties unique to separable BICs: the ability to control the direction of emitted radiation using perturbations, and also the ability to control the dimensionality of the emitted radiation. This may lead to two applications. In the first, perturbations are used as a switch which can couple waves into a cavity, store them, and release them in a fixed direction. In the second, the number of dimensions of confinement of a wave can be switched between one, two, and three by exploiting perturbation parity. The property of dimensional and directional control of resonant radiation serves as a new and additional potential advantage of BICs over traditional methods of localization. Also, with the general criterion for separable BICs, we have extended the existing handful of examples to a wide variety of wave systems including: three-dimensional quantum mechanics, paraxial optics, and lattice models which can describe 2D waveguide arrays, quantum dot arrays, optical lattices, and solids.

# Chapter 3

## 2D Plasmonics: Shrinking the Wavelength of Light to Allow Forbidden Transitions

### 3.1 Introduction

A fundamental process of extraordinary interest in the field of light-matter interaction is spontaneous emission, in which an excited electron in an atom lowers its energy by emitting light [40, 41, 42]. Spontaneous emission is responsible for the characteristic emission spectrum of an emitter. In principle, an excited electron can fall into any unoccupied lower energy level via this process. In practice, the *vast* majority of radiative decay channels are too slow to be accessible, rendering most of the spectrum invisible and inaccessible. The wealth of forbidden light-matter interaction processes can be appreciated by considering three very general classes of forbidden transitions: multipolar processes, spin-flip processes, and multi-quanta emission processes.

Multipolar transitions are those in which the orbital angular momentum (OAM) of the electron changes by more than one unit. They are slow because the wavelength

of emitted light (around  $10^3$  to  $10^4 \text{ \AA}$ ) is typically far larger than the size of the atomic or molecular orbitals participating in the transition (around 1 to 10  $\text{ \AA}$ ). As a result of this vast difference in scales, the rates of electronic transitions as a function of change in angular momentum (OAM) vary over many orders of magnitude: the difference in rates between changing OAM by 1 and changing OAM by 5 can be over twenty orders of magnitude, making high OAM changing transitions invisible in the absorption and emission spectrum of an emitter. The ability to access these transitions would allow a multiplex and broadband spectroscopy platform, in which much more of the electronic energy level structure of an emitter can be probed using light.

A spin-flip process is one in which the spin of the electron flips as a result of the emission. Common spin-flip processes includes those in which a single electron flips its spin and those in which a pair interconverts between a singlet and triplet state. Because these processes are very slow, spin-flip processes typically occur through phosphorescence, which is fast only when the electrons experience large spin-orbit coupling [43, 44]. In systems where spin-orbit coupling is weak, such as in light atoms or hydrocarbon molecules, the radiative quantum yield of phosphorescence is low, because the singlet-triplet transition is much slower than nonradiative recombination processes. This is undesirable for applications such as organic-based LEDs where high radiative quantum efficiency is desired.

Multi-quanta emission processes are those in which an electron lowers its energy by emitting two or more quanta of light. It is a higher-order process in quantum electrodynamics. While it is not forbidden by dipole selection rules, it is typically so slow that we group it with the other two processes above. Due to the small size of the atom relative to the light it emits, and the small value of the fine-structure constant, emission of even two quanta tends to be 8-10 orders of magnitude slower than the emission of a single quantum of light. This makes two-quanta spontaneous emission processes notoriously difficult to observe. In fact, while two-photon spon-

taneous emission was predicted in the early 1930s [45], the first direct observation of two-photon spontaneous emission in Hydrogen occurred in 1996 [46]. Going beyond atomic physics, two-quanta spontaneous emission processes are also of interest in semiconductors, where they were first observed in 2008 [47, 48]. Enabling two-quanta spontaneous emission processes at a fast rate would enable generation of entangled light, which is of great interest for implementing quantum protocols [49]. It would also enable a new generation of broadband light absorbers and novel broadband light sources using atoms and molecules.

Despite the fact that there is sufficient motivation to access all of these transitions, it is in practice very difficult. Conservation of energy and angular momentum dictates that in order to access the full spectrum of an emitter, it must couple to light, which, over a broad range of frequencies in the IR-VIS range, has wavelengths on the order of 1 – 5 nm (once inside an optical material). The wavelength of light and its frequency are related by the phase velocity. It follows that in order to access forbidden transitions, phase velocities of light of order  $.001c$  are required. Recent theoretical and experimental breakthroughs have shown that systems such as graphene, silver monolayers, beryllium surfaces, and others can support precisely such strongly confined light in the form of plasmons. These 2D systems have the unique ability to squeeze the wavelength of light by over two orders of magnitude, which we now show forces us to recast the main assumptions for light-matter interactions.

Here, we report that with the recent discovery of 2D plasmons [50, 51, 52, 53, 54, 55, 56, 57, 58, 59, 60, 61, 62], we can overcome all of the mentioned conventional limitations of light-matter interactions. In particular, we show by means of a general theory of atom-plasmon interactions that the rates of high-order multipolar transitions, two-plasmon spontaneous emission, and spin-flip transitions become significantly enhanced to the point that they are comparable to dipole transition rates and thus become straightforwardly accessible. In fact, for achievable plasmon con-

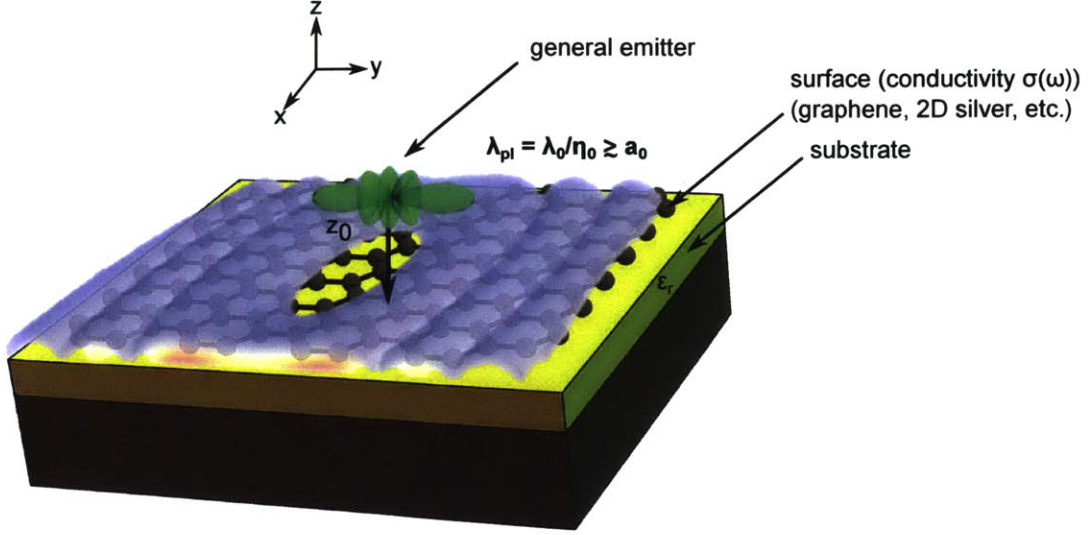


Figure 3-1: **2D Plasmons Coupled to an Emitter.** A schematic of an emitter (not-necessarily dipolar) above a 2D material of conductivity  $\sigma(\omega)$  supporting plasmons with wavelength,  $\lambda_{pl}$  far shorter than the photon wavelength,  $\lambda_0$  (by a factor of  $\eta_0$ ) and approaching the atomic size,  $a_0$ .

finements in graphene and other 2D-plasmon-supporting materials, the lifetimes of all of the above types of transitions can fall in the range of  $1 \mu\text{s}$ – $1 \text{ ns}$ .

## 3.2 2D Plasmons and Light-Matter Interaction: Model and Assumptions

Plasmons are understood in the framework of classical electrodynamics as being coherent propagation of surface charge associated with tightly confined electromagnetic fields. The dispersion relation of any plasmon can be most simply expressed as:

$$\omega = v_p q \equiv \frac{c q}{\eta(q)}, \quad (3.1)$$

where  $q$  is the plasmon wavevector,  $v_p$  is the phase-velocity and  $\eta$  is the confinement factor, which is equal to both  $c/v_p$  and  $\frac{\lambda_0}{\lambda_{pl}}$ . The fact peculiar to 2D plasmons is that

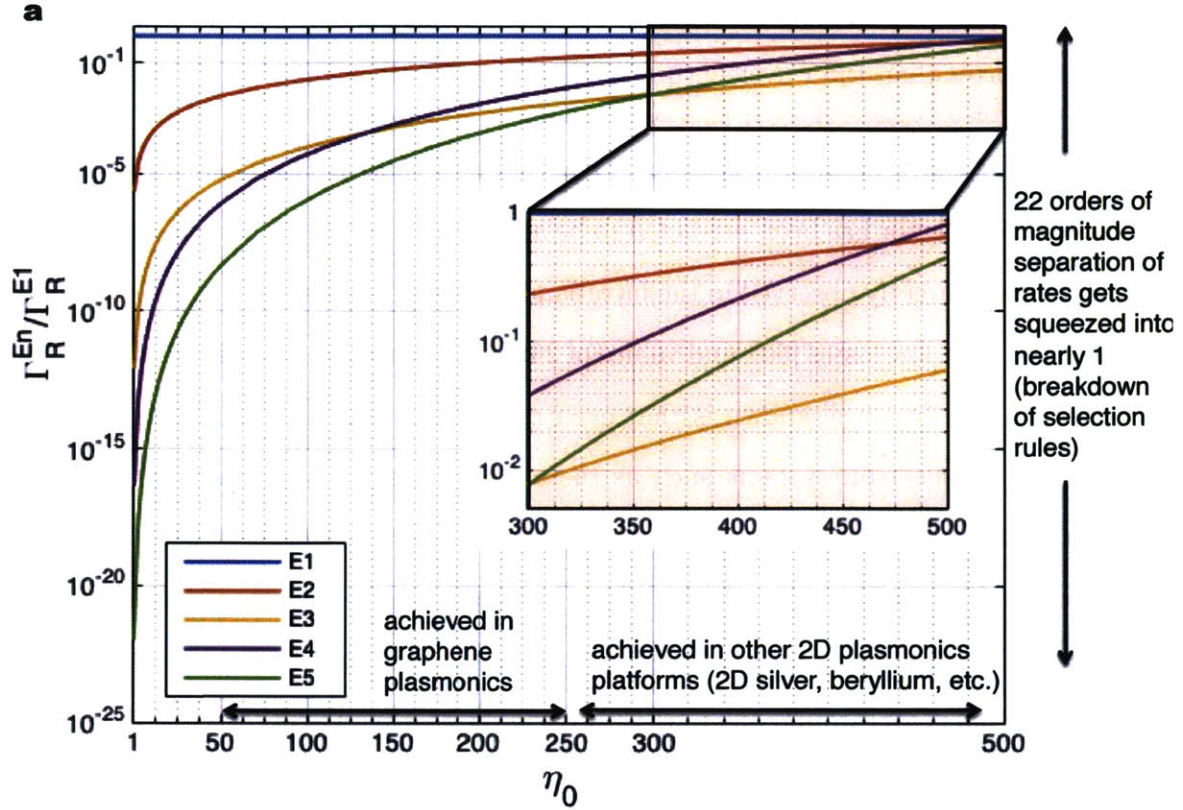


their wavelength,  $\lambda_{pl}$ , which is determined by the dispersion relation, can be 100-400 times shorter than the wavelength of a photon,  $\lambda_0$ , at the same frequency.

By far, the best known type of 2D plasmon is that in graphene, in which the confinement factor has been predicted to be as high as 300 [54], with values in excess of 200 being indirectly observed in the intraband regime [62], values of 150 being directly observed with low losses [60], and values of 240 being observed in the interband regime [52]. What is less well-known is that even more highly confined plasmons can exist in other 2D electron systems such as metallic monolayers. In other 2D plasmons such as mono-layer silver, confinement factors as high as 300 have been observed, corresponding to plasmon wavelengths of around 5 nm at photon wavelengths of 1.5  $\mu m$  [50]. On the surface of beryllium, acoustic plasmons have been observed at visible frequencies (around 560 nm) with plasmon wavelengths of merely 1.5 nm [51] - corresponding to confinement factors near 370. In our study, we look at the emission of 2D plasmons by Hydrogen-like and Helium-like atomic emitters in the vicinity of a 2D conductor given by the minimally-coupled Hamiltonian:

$$\begin{aligned}
H &= H_a + H_{em} + H_{int} \\
H_a &= \left( \sum_i \frac{\mathbf{p}_i^2}{2m_e} - \frac{e^2}{4\pi\epsilon_0 r_i} \right) + H_{e-e} + H_{SO} \\
H_{em} &= \sum_k \int d\mathbf{r} \int d\omega \hbar\omega \left( f_k^\dagger(\mathbf{r}, \omega) f_k(\mathbf{r}, \omega) + \frac{1}{2} \right) \\
H_{int} &= \sum_i \frac{e}{2m} (\mathbf{p}_i \cdot \mathbf{A}(\mathbf{r}_i) + \mathbf{A}(\mathbf{r}_i) \cdot \mathbf{p}_i) + \frac{e^2}{2m} \mathbf{A}^2(\mathbf{r}_i) + \frac{e\hbar}{2m} \boldsymbol{\sigma}_i \cdot \mathbf{B}(\mathbf{r}_i), \quad (3.2)
\end{aligned}$$

where  $e$  is the electronic charge,  $m_e$  is the electron mass,  $\mathbf{A}$ ,  $\mathbf{B}$  are the vector potential and magnetic fields,  $\mathbf{r}_i$  denotes the position of the  $i$ th electron,  $\sigma_i$  denotes the spin of the  $i$ th electron,  $H_{SO}$  is the spin-orbit coupling, and  $H_{e-e}$  is the electron-electron interaction. The  $\hat{f}_k^{(\dagger)}(\mathbf{r}, \omega)$  annihilate (create) elementary excitations of the lossy electromagnetic field. The features of the plasmon and emitter relevant to our



calculations are shown schematically in Figure 1. This Hamiltonian, with field operators that appropriately describe the (potentially very high) losses in these confined plasmons, is sufficient to describe radiative decay and nonradiative decay mediated by interactions of the electromagnetic field with orbital and spin degrees of freedom of the electron in an atom. It also describes intercombination transitions, multiplasmon emission, and other processes higher order in the perturbation theory. In this study, we examine all of these in order to provide a broad picture of atom-light interactions in plasmonics. Our calculations are discussed in greater detail in the Supplementary Materials. We choose Hydrogen and Helium-like emitters for definiteness, but the basic physics behind our results can readily be extended to any other atomic and molecular system. Although we only explicitly consider spontaneous emission in this text, our results hold equally well for the absorption of excited 2D plasmons. We note

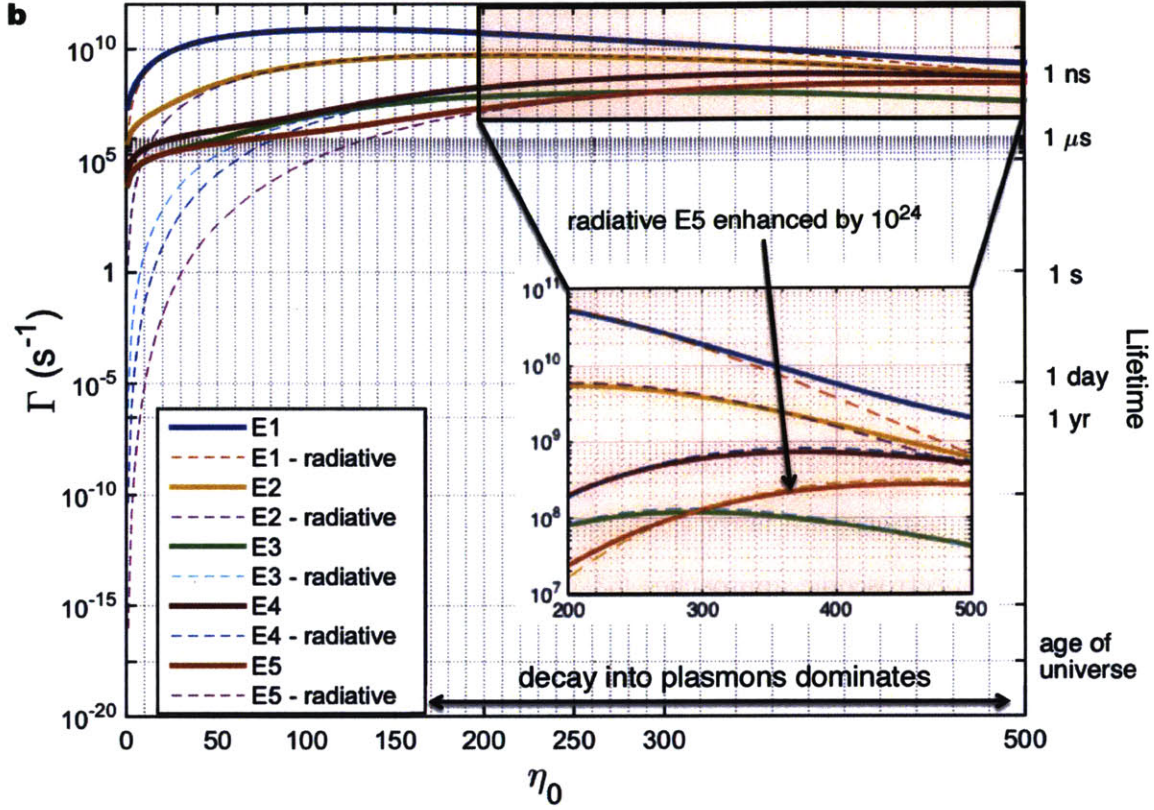


Figure 3-2: **Convergence of the Multipoles.** (a) Rates of radiation into surface plasmons for various multipolar transitions in Hydrogen. The transition series considered here is  $6\{p, d, f, g, h\} \rightarrow 4s$ . The emitter is situated 5 nm above the surface of graphene. (b). Total rates (radiative + non-radiative) of decay for the same transition series in Hydrogen. Dashed lines show radiative rates, which agree with the total rates at high confinement.

here that our approach can be applied to plasmons in 2D conductors with any general dispersion relation (for which the Drude model is a representative example that we consider). Our model can be generalized to consider nonlocal effects by modifying the Green function formalism. We expect nonlocal effects to kick in at atom-surface separations  $z_0 \leq \frac{v_f}{\omega_0}$ , where  $v_f$  is the Fermi velocity and  $\omega_0$  is the transition frequency. We operate outside of this regime when making conclusions based on our calculations.

### 3.3 Multipolar Transitions

The first class of forbidden transitions that we analyze in our study are higher-order multipolar transitions in which the orbital angular momentum of the electron changes by more than one. It is well known that in conventional photonics and even conventional plasmonics, dipole transitions are by far the fastest type of transitions, and are thus appropriately the main object of study in the field of light-matter interactions. Electric quadrupole and magnetic dipole transitions, which are the second fastest types of transitions, are fairly slow, but can occasionally be observed through conventional spectroscopic approaches [63], or in mesoscopic emitters such as quantum dots. Significant theoretical and experimental efforts have gone towards speeding up these two processes [64, 65, 66, 67, 68, 69, 70, 71]. On the other hand, electric octupole, magnetic quadrupole, and higher order multipolar transitions are far too slow to observe for small emitters such as atoms and molecules. Therefore, theoretical and experimental efforts have not been directed at speeding up such processes. Nevertheless, the high-energy spectrum of an atom mostly consists of precisely these types of transitions. As we now demonstrate, due to the high confinements achievable in 2D plasmons, the contributions to radiative decay from very high-order multipolar transitions can become comparable to those from dipole transitions in atomic systems. In fact, transitions whose lifetimes in free-space approach the age of the universe can be brought down to lifetimes of hundreds of nanoseconds, corresponding to rate enhancements (Purcell factors) of nearly  $10^{24}$ . Such lifetimes are of the same order of magnitude as dipole transitions in free space and therefore should be straightforwardly accessible through absorption spectroscopy.

To explain this, we calculate the rates of transitions where the electron orbital angular momentum changes by  $n$  (an  $En$  transition), as shown in the SI. The decay

rate  $\Gamma_n$  into plasmons scales with  $\eta_0$  as:

$$\Gamma_n \sim \eta_0^{3+2(n-1)} e^{-2\eta_0 k z_0}, \quad (3.3)$$

which makes it very clear that higher electric multipole transitions are enhanced by successively larger amounts. For achievable confinement factors of 100, when  $n$  increases by 1, the enhancement increases by a factor of roughly 10000. Therefore, one should expect that if the dipole transitions ( $n=1$ ) are enhanced by  $10^6$ , then an E2, E3, E4, and E5 transition should be enhanced by  $10^{10}$ ,  $10^{14}$ ,  $10^{18}$ , and  $10^{22}$ , respectively. One feature Equation (3) is that for high-order multipolar transitions, the decay rates have an extremely sharp dependence on the confinement. For example, with E5 transitions, where the rates of surface plasmon launching scale as  $\eta_0^{11}$ , a change in the confinement factor by a factor of 2 changes the decay rate by over three orders of magnitude.

Equation (5) above can be intuitively reasoned as follows:  $\eta_0^3$  is the enhancement resulting from the high density of states of 2D plasmons, the exponential factor is the suppression of the intensity of electromagnetic fields due to the evanescent nature of plasmons, and the extra factor of  $\eta_0^{2(n-1)}$  arises because of the well-known fact that  $E_n$  transitions are suppressed relative to E1 transitions by  $(ka)^{2(n-1)}$ , where  $a$  is the emitter size and  $k$  is the wavevector of the electromagnetic field. The plasmon wavevector is  $\eta_0$  times larger than the free-space wavevector,  $k$ , and so associated with that is an enhancement by the factor  $\eta_0^{2(n-1)}$  in addition to the  $\eta_0^3$  enhancement.

Such an intuition is confirmed in Figure 2, where we plot the exact transition rates, with and without plasmonic losses, for the series of transitions  $6\{p, d, f, g, h\} \rightarrow 4s$  in the Hydrogen atom. The free-space wavelength of the transition is  $2.6 \mu\text{m}$ . In our simulations, the emitter is kept 5 nm away from the surface <sup>1</sup>. In Figure

---

<sup>1</sup>The  $6s \rightarrow 4s$  rate is zero when the atom is well separated from the surface due to the transversality of the electromagnetic field ( $\nabla \cdot \mathbf{E} = 0$ ). The dominant decay mechanism for this process will be two-plasmon emission, which we compute in Section 5.

2(a), we plot the radiative rates (i.e; plasmon emission rates) of transitions in the Hydrogen  $6 \rightarrow 4$  series relative to the radiative rate of the dipole transition (at the same energy) as a function of confinement. This relative rate is independent of atom-surface separation, as can be seen from Equation (3). To give a particular example, conventionally the E5 transition is separated from the E1 transition by over 22 orders of magnitude. The free-space rate of the E5 transition is around  $10^{-16}$   $\text{sec}^{-1}$ , corresponding to a lifetime which is two orders of magnitude less than the age of the universe. For high confinement ( $\eta_0 \sim 200$ ), the rate is around  $10^7$   $\text{sec}^{-1}$ , which is over an order of magnitude faster than the free-space E1 transition. In addition to plotting confinement factors up to 250, we also plot confinement factors that are higher than have been observed in graphene below the interband regime. This is because such high confinement factors have been observed in plasmons in mono-layer silver, DySi<sub>2</sub>, graphene with high losses, acoustic plasmons in beryllium [50, 51, 52, 53]. We plot up to very high confinement factors of 500, corresponding to plasmon wavelengths of 5 nm. At these low wavelengths, which have been observed in the aforementioned systems, *four of the five transitions in the series lie within the same order of magnitude, corresponding to a complete breakdown of the conventional selection rules.* Furthermore, another reason to plot for high confinement factors (even for graphene) is that it has recently been suggested via a modified random-phase approximation scheme that confinement factors above 300 may be possible with relatively low losses [72].

In addition to radiation into plasmons, an excited emitter can be non-radiatively quenched by a conductor. Non-radiative quenching channels can include, but are not limited to: phonons, particle-hole excitations, and impurities. These are incorporated in our calculations through the real part of the surface conductivity. In Figure 2(b), we plot the total rates of the transitions considered in Figure 2(a), i.e; radiative+non-radiative (solid lines) in addition to the radiative decay rates (dashed lines). For low confinement, the non-radiative decay is completely dominant. This reflects the well-known fact that non-radiative energy transfer strongly depends on the ratio  $\frac{1}{kz_0}$ . What is more valuable for optical applications is the situation at high confinement  $\eta_0 > 150$ . There, the radiation into plasmons is dominant and can be harvested as far-field light through suitable outcoupling techniques such as gratings and nanoantennas [73, 74, 75, 76] <sup>2</sup>.

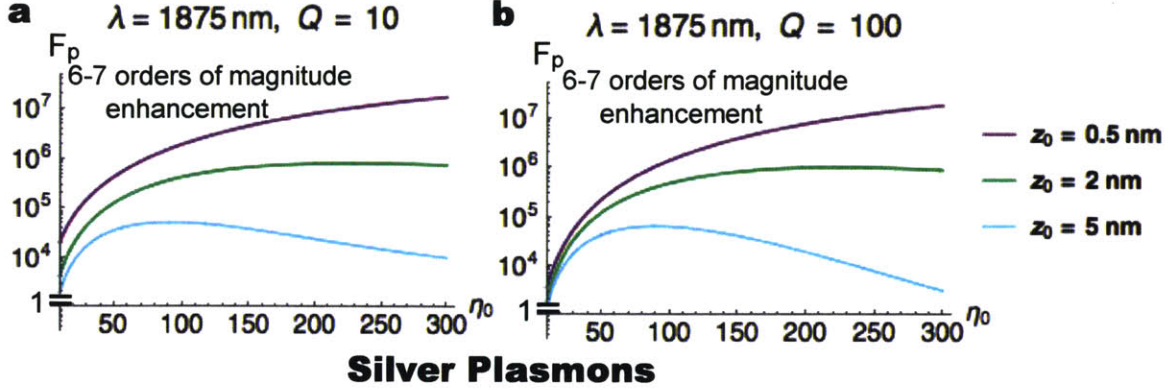
### 3.4 Spin Flip Transitions and the Singlet-to-Triplet Transition

The next type of transitions that we analyze here are those in which the initial state does not directly connect to the final state by the emission of light, but rather couples to a virtual state whose symmetry is compatible with that of the final state. Take as an example a radiative transition between a spin-singlet state, S, and a spin-triplet state, T. The dominant process for systems with large spin-orbit coupling is a second-order process in which an initial triplet state connects to a virtual singlet state,  $S_n$ ,

---

<sup>2</sup>For applications in which fast non-radiative decay is desired, we note that for considerably low wavelengths  $\frac{1}{kz_0} \approx 1$ , the non-radiative decay is much faster than one would naively expect. This is because the non-radiative decay still couples to the multipole moment relevant to the atomic transition. Therefore, the strong enhancement of rates coming from matching the atomic size to the wavelength of light compensates for the suppression of rates coming from a higher  $kz_0$ . In fact, the total rate - even when non-radiative energy transfer is dominant - increases as the wavelength shrinks. From this, we conclude that for both radiative and non-radiative decay, the high confinement of 2D plasmons helps overcome the small size of the atom.

## Graphene Plasmons



## Silver Plasmons

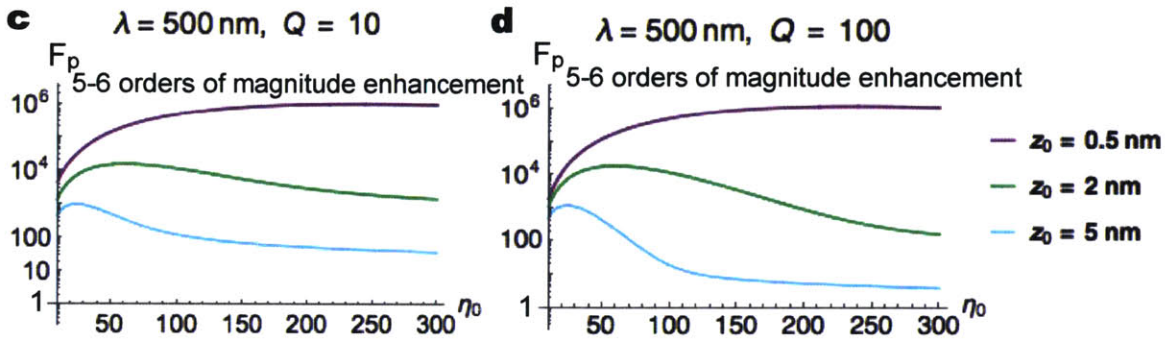


Figure 3-3: **Enabling singlet to triplet transitions.** Purcell factors for a dipolar singlet-triplet transition as a function of confinement factor  $\eta_0$  for (a,b) plasmons in graphene and (c,d) plasmons in 2D silver, for different atom-plane separations,  $z_0$  and quality factors,  $Q$ . These results also apply to other kinds of intercombination transitions, such as those in which the spin of an atomic emitter is flipped due to radiation.

through the spin-orbit coupling, and then the virtual state connects to the final singlet state and emits light. The decay rate is then given by the second-order Fermi Golden Rule:  $\Gamma(T \rightarrow S) = \frac{2\pi}{\hbar^2} \sum_{\mathbf{q}} \left| \sum_n \frac{\langle S, \mathbf{q} | H_{em} | S_n, 0 \rangle \langle S_n, 0 | H_{SO} | T \rangle}{E_T - E_{S_n}} \right|^2 \delta(\omega_{\mathbf{q}} - \omega_0)$ , where  $\omega_0$  is the transition frequency and  $\mathbf{q}$  is the wavevector of an emitted plasmon.

To calculate the decay rate using the Fermi Golden Rule, one should sum over all possible intermediate states. However, in many cases, there is an intermediate singlet state that is nearly degenerate with the triplet state, which then gives the dominant contribution to the transition. The advantage of this approximation is that the spin-orbit and electromagnetic enhancements decouple. *Our approach allows the*



*calculation of the enhancement factor without knowing anything about the spin-orbit coupling or even the structure of the atom/molecule* and thus our results can be applied to many atomic and molecular systems. The Purcell factor, defined as the emission rate into plasmons divided by the emission rate into free-space photons, in the absence of plasmon losses is proportional to

$$F_p(T \rightarrow S) \sim \eta_0^3 e^{-2\eta_0 k z_0}, \quad (3.4)$$

where  $\eta_0$  is the confinement factor at the transition frequency  $\omega_0$ , and  $z_0$  is the separation between the atomic nucleus and the surface. The three powers of confinement arise from the high density of states of 2D plasmons, and the exponential factor is simply a result of the exponentially decaying field amplitude associated with a plasmon mode. This simple formula is only weakly modified by plasmonic losses, which were taken into account in our numerical calculations (see SI for further details). These high enhancement factors are in agreement with the  $\eta^3$  decay law of pure electric dipole transitions [77, 78].

In Figure 3, we illustrate the Purcell factors for  $S \leftrightarrow T$  transitions achievable for an emitter on top of graphene and monolayer silver as a function of plasmon confinement. We show the Purcell factors at distances of 0.5, 2, and 5 nm away for two different plasmon quality factors ( $Q=10$  and  $Q=100$ ). Figure 3 demonstrates how 2D plasmons can enhance singlet to triplet transition by up to 7 orders of magnitude for realistic and experimentally readily available parameters. This enhancement is in addition to enhancements coming from increasing spin-orbit coupling. This allows one to combine approaches involving high spin-orbit couple and approaches involving plasmonics to get the highest possible enhancements. Perhaps of more interest, the independence of electric dipole and spin-orbit enhancement of spin-flip transition rates allows one to reconsider the use of emitters with weak spin-orbit coupling. For

example, by enhancing the triplet decay by 4-6 orders of magnitude, one can take a triplet state of a hydrocarbon with a typical phosphorescence time of 0.1-0.001s and make it competitive, or even faster than phosphorescence of organometallic triplet states with high spin-orbit coupling.

We conclude this section by noting that there is another method of enhancing spin-flip and singlet-triplet transitions, which is a direct emission into a plasmon through the  $\mathbf{S} \cdot \mathbf{B}$  term of the interaction Hamiltonian. Such a direct spin-flip (or singlet-triplet) transition involves an  $Mn$  transition, for which the decay rate into plasmons is slower than its electric counterpart by the ratio  $\frac{\hbar\omega_0}{m_e c^2} \sim 10^{-5} - 10^{-6}$  and is thus much slower than the intercombination mechanism for spin-orbit couplings of interest. We demonstrate this claim by deriving rates for  $Mn$  transitions in the SI.

### 3.5 Two-Plasmon Spontaneous Emission

Finally, we consider the spontaneous emission of two quanta of the electromagnetic field. The emission of two excitations of a field (photons or plasmons) is a second-order effect in perturbation theory. If the dimensionless coupling constant of atomic QED,  $g$ , is small, then the two-quanta emission will be very slow compared to the emission of a single field excitation. A good estimate for the coupling constant is given by  $g^2 = \frac{\Gamma}{\omega_0}$ . When this becomes nearly one, we expect the Fermi Golden Rule (and more generally, perturbation theory) to fail because the width of the resulting atomic resonance compares to the frequency scale of variation of the continuum matrix elements [79]. Taking this as our dimensionless coupling constant, we see that it scales as  $g_n \sim \sqrt{\alpha(k a_0)^2 \eta_0^{3+2(n-1)} e^{-\frac{4\pi\eta_0 z_0}{\lambda^h}}}$  in atomic and molecular systems, where  $a_0$  is the characteristic emitter size (for example, the Bohr radius).

For dipole transitions, this coupling constant suggests that the emission rate of two plasmons scales as  $g^4 \sim \eta_0^6$ . Our exact derivation shows this is indeed the case (see

SI for further details), for both Drude-like and linear plasmon dispersions. Similar conclusions hold for other dispersion relations. We arrive at the following analytical expression for the enhancement of the differential decay rate (in the lossless limit) for any two-plasmon  $S \rightarrow S$  transition in a Hydrogenic atom:

$$\frac{d\Gamma/dy|_{2\ pl}}{d\Gamma/dy|_{2\ ph}} = \frac{d\Gamma/d\omega|_{2\ pl}}{d\Gamma/d\omega|_{2\ ph}} = 72\pi^2 (\eta_0^3 e^{-2\eta_0 k z_0})^2 \times (y - y^2)^3 e^{8\eta_0 k z_0 y(1-y)}, \quad (3.5)$$

where  $y = \frac{\omega}{\omega_0}$ , and  $\eta_0$  is the confinement factor at the spectral peak of the emission. Said peak occurs for  $\omega = \frac{1}{2}\omega_0$ , or equivalently,  $y=1/2$ .  $\frac{d\Gamma}{d\omega}(\omega')$  corresponds to the rate of emission of two plasmons per unit frequency in which one plasmon is at frequency  $\omega'$  and the other is at frequency  $\omega_0 - \omega'$ . A quick estimate using Equation (5) reveals that at confinement factors of 100, *the Purcell factor per unit frequency tends to  $10^{15}$  as  $z_0 \rightarrow 0$ .*

In Figure 4(a), we plot the distribution of emitted plasmons as a function of normalized frequency,  $y$ . The spectral distribution narrows as a function of the atom-surface separation,  $z_0$ , which we illustrate in Figure 4(b). This arises from the  $y$  dependence of the exponential in Equation (5). Therefore, through a precise control of the position of an emitter above a surface supporting plasmons, not only can the rate of emission be tuned, but also the shape of the spectrum of emission.

In Figure 4(c), we plot an estimate of the total decay rate for the transition  $4s \rightarrow 3s$ , which is computed by summing over 10 virtual discrete states (our estimate is discussed in the SI). The rate converges sufficiently for 10 virtual states. For experimentally achievable values of  $\eta_0$  of around 100, and at atom-surface separations of 5 nm, the two-plasmon spontaneous emission rate approaches  $1\ \text{ns}^{-1}$ , in stark contrast with the typical rate of roughly  $1\ \text{min}^{-1}$  in free-space. For confinements beyond 200, it is possible to get emission rates exceeding  $1\ \text{ps}^{-1}$ . We compare the rate of this transition with that of the  $4s \rightarrow 3p$  single-plasmon dipole transition in

Figure 4(d); in the region of extreme confinement (200-500), the two-plasmon emission is only 1-2 orders of magnitude slower. At these extreme confinements – such that the two-plasmon emission is slower than the one plasmon emission by two orders of magnitude – the dimensionless coupling constant,  $g$ , is of order 0.1, *signaling the onset of the ultrastrong coupling regime.*

We find that for plasmons described by the Drude model, the ratio of the rates plotted in Figure 4(d) has a very weak distance dependence. This arises from the fact that at greater atom-surface separations, the spectrum of emitted plasmons narrows. Therefore, most of the emitted plasmons have frequencies near  $y = 1/2$ . When this happens, the distance dependence of the two-plasmon decay rate approaches  $e^{-2\eta_0 k z_0}$ , which is the same distance dependence as that of the one-plasmon decay rate. This is a feature of the  $\omega \sim \sqrt{q}$  dispersion of plasmons well-described by the Drude model. For plasmons with linear dispersion (such as acoustic plasmons), the distance dependence of the two-plasmon differential emission rate is simply  $e^{-4\eta_0 k z_0}$  (i.e; no  $y$  dependence, in contrast to that of Eq. (5)).

The results summarized in Figures 4(c) and 4(d) establish that two-plasmon spontaneous emission is very fast in the vicinity of 2D plasmons. In fact, it should already be experimentally achievable to observe lifetimes for two-plasmon processes on the order of 1 ns, which is of similar order of magnitude to that of fast dipole transitions in free-space. It is also merely 1.5 to 2.5 orders of magnitude slower than a single plasmon emission process involving a dipole transition. One may imagine an emitter such that its only decay channels are, for instance, a quadrupole transition and a two-plasmon spontaneous emission process; then, the two-plasmon spontaneous emission rate is of the same order, or faster than the quadrupole emission. This emitter would then be an efficient source of entangled light. Using low-loss plasmons, like those observed recently in graphene [60], and the results presented here, one may be able to generate and couple out entangled plasmons at a fast rate.

Transition	Free Space $\Gamma$	2D Plasmon $\Gamma$	$\eta$ Enhancement
E1	$\alpha \left( \frac{\hbar\omega}{m_e c^2} \right)$	$\alpha \left( \frac{\hbar\omega}{m_e c^2} \right) \eta^3$	3
En <sup>3</sup>	$\alpha \left( \frac{\hbar\omega}{m_e c^2} \right) (ka_0)^{2(n-1)}$	$\alpha \left( \frac{\hbar\omega}{m_e c^2} \right) (ka_0)^{2(n-1)} \eta^{3+2(n-1)}$	3+2(n-1)
Spin-Flip Ek <sup>4</sup>	$\alpha \left( \frac{\hbar\omega}{m_e c^2} \right) (ka_0)^{2(n-1)}$	$\alpha \left( \frac{\hbar\omega}{m_e c^2} \right) (ka_0)^{2(n-1)} \eta^{3+2(n-1)}$	3+2(n-1)
2PSE <sup>5</sup> (Dipole)	$\alpha^2 (ka_0)^4$	$\alpha^2 (ka_0)^4 \eta^6$	6
M1 <sup>6</sup>	$\alpha \left( \frac{\hbar\omega}{m_e c^2} \right)^2$	$\alpha \left( \frac{\hbar\omega}{m_e c^2} \right)^2 \eta$	1
Mn <sup>a</sup>	$\alpha \left( \frac{\hbar\omega}{m_e c^2} \right)^2 (ka_0)^{2(n-1)}$	$\alpha \left( \frac{\hbar\omega}{m_e c^2} \right)^2 (ka_0)^{2(n-1)} \eta^{2(n-1)+1}$	1+2(n-1)

Table 3.1: A summary of derived scalings of rates and rate enhancements for emitters on top of lossless 2D plasmons at zero displacement from the plasmon supporting surface. The rates for an emitter at finite distance from the plasmon are suppressed by  $e^{-2\eta_0 k z_0}$ , which is of order unity for an emitter within a reduced plasmon wavelength of the surface. Note that these scalings are still a good approximation even in the presence of high losses provided that the confinement is large, as shown in Fig. 2.

Finally, we note that the effect of losses is considered in our study. For simplicity, we relegate our analysis of losses into the SI. In brief, for this particular transition, second-order quenching effects are only of extreme relevance at very short atom-surface separations of below 1 nm (see Figure S4 to see how the results in Fig. 4b are modified by losses.). Below this length scale, nonlocal effects and microscopic QED effects should be considered [78], which is beyond the scope of our model. However, our consideration of losses opens up the possibility of observing and potentially using a new decay mechanism for emitters near a surface - non-radiative decay through two (entangled) lossy excitations (i.e; *double quenching*).

### 3.6 Summary and Outlook

We have shown here that 2D plasmonics, with its unprecedented level of confinement presents a unique opportunity to access radiative transitions in atomic-scale emitters that were considered inaccessible. Multi-plasmon processes, spin-flip radiation, and very high-order multipolar processes have been shown to be competitive with the fastest atomic transitions in free-space, rendering them all accessible. Our findings

have been summarized in Table I. These findings pave the way to observing and taking advantage of new light-matter interactions. In particular, our findings may force the reconsideration of many atomic, molecular, and solid-state emitters whose transitions are normally too weak and inefficient to be used, thus bringing the full variety of the periodic table to optical applications. The physics responsible for the effects reported here may also be present in optical antennas whose dimensions are of order 1 nm, although such dramatic effects have not been reported or predicted; a more detailed investigation is needed to establish if our results are achievable in these cavity systems. However, even if they are, a significant advantage of planar 2D plasmonics for accessing forbidden transitions is that the effect does not depend on the position of the emitter in the plane parallel to the 2D conductor. In cavity-based emission enhancement platforms, especially those in which fields are confined in a few nanometer gap, the (atomic-scale) emitter must be positioned very precisely in order to observe the enhancement.

With regards to applications of this work to fundamental light-matter interactions, we believe that a number of fruitful extensions are within reach. Beyond the processes that we considered in this work, one can consider combinations of these processes, such as:

1. Multi-plasmon transitions mediated by higher-order multipole virtual transitions. For example, a two-plasmon emission with a total angular momentum change of 4 for the electron, by way of an intermediate quadrupole virtual transition.
2. Three and higher order plasmon emission and absorption processes
3. A second order absorption process in which a plasmon and a far-field photon are absorbed, leading to large changes in energy and angular momentum of the electron, due to the photon and plasmon respectively.

All of these transitions should be significantly enhanced using 2D plasmonics, but beyond the reach of conventional plasmonics and photonics without extremely high intensities of light. We stress that the results we have presented in this letter are unoptimized. We performed our work with Hydrogen purely as a proof-of-concept. For example, by finding an atom with a high octupole moment, it should be possible to make the octupole transition dominant over the dipole and other multipolar transitions - paving the way for emitters with characteristic multipolarity different than dipolar. It should similarly be possible to optimize the rate of multi-plasmon spontaneous emission relative to other transitions, leading to emitters highly capable of emitting entangled light.

The potential applications of this work include: spectroscopy for inferring electronic transitions which cannot be determined with photons, sensors based on forbidden transitions, organic-light sources arising from fast singlet-triplet transitions, fast entangled light generation, and fast generation of broadband light with tunable width in the visible or IR. At the time of this submission, experiments are being performed to verify the conclusions of this theoretical study.

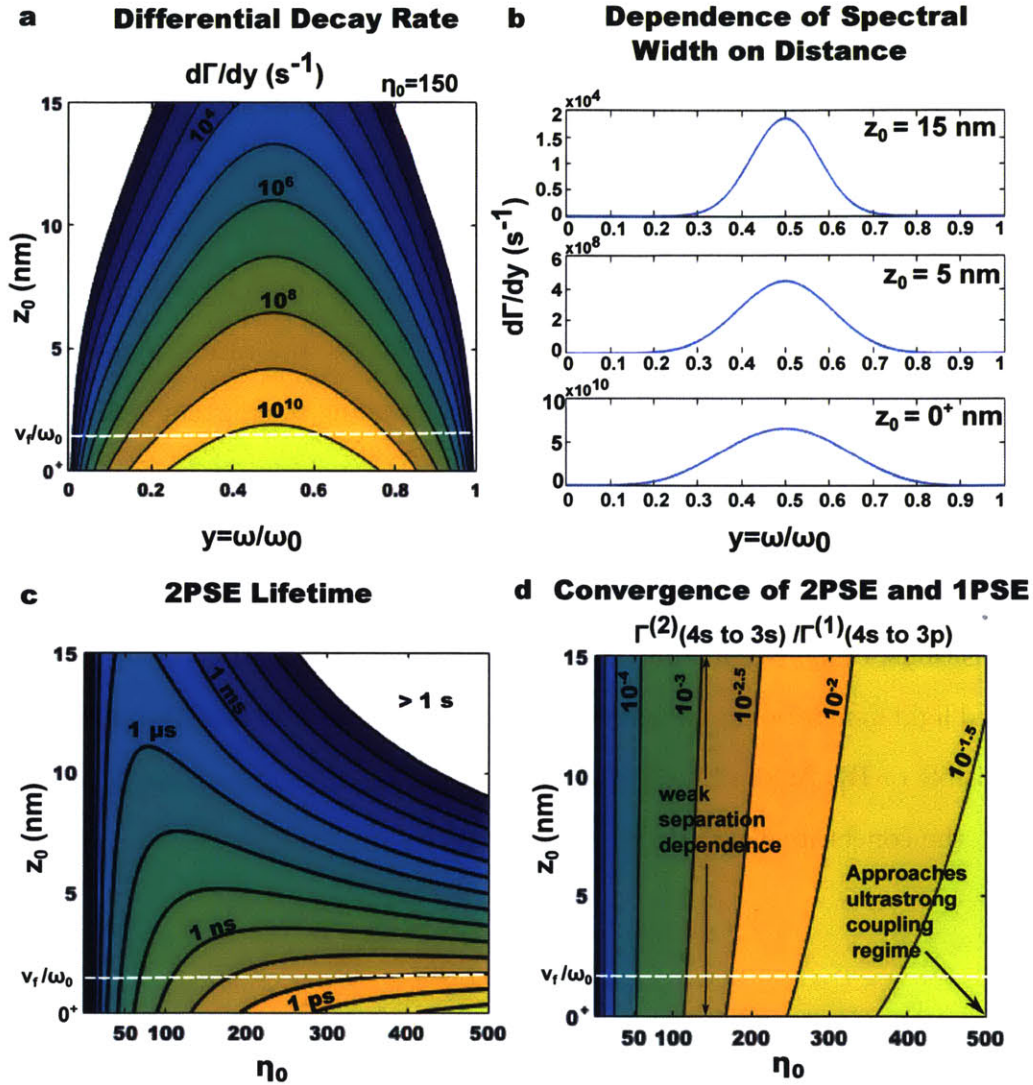


Figure 3-4: Enabling Two-Plasmon Radiative Energy Transfer. (a) Emission spectrum of two-plasmon spontaneous emission (2PSE) as a function of frequency and atom-surface separation for the Hydrogen  $4s \rightarrow 3s$  transition above Graphene.  $\eta_0$  is chosen to be 150. (b). Linecuts of (a) for atom-surface separations of 0, 5, and 15 nm. (c) Total decay rate (in  $sec^{-1}$ ) for this transition as a function of confinement and atom-surface separation. (d) Comparison of two-plasmon emission rate to the emission rate for a single plasmon  $4s \rightarrow 3p$  transition as a function of confinement and separation.



# Chapter 4

## Phonon Polaritons: Turning Forbidden Transitions into Dominant Transitions

### 4.1 Introduction

Plasmonics – an extremely active field of research for several decades – can be seen as the study of the consequences of confining electromagnetic fields to regions much smaller than the wavelength of a far-field photon at the same frequency [80]. Such confinement allows for amplification of electromagnetic fields allowing for enhanced Raman scattering [81, 82], the ability to enhance the inherently weak nonlinearities of materials [83], and even the potential to light-matter interaction processes in atomic-scale emitters which for almost a century have been considered impossible to observe [84, 85, 86, 87, 41, 88, 89, 48, 47, 90].

In particular, plasmons have been observed in 2D conductors which are so strongly confined over a broad spectral band that it is possible to access all sorts of highly forbidden transitions: high-order multipole transitions, two-plasmon spontaneous emis-

sion processes, and spin-flip phosphorescence processes [87]. However, with such a broadband enhancement of forbidden transitions comes a price: it is very difficult to pick a particular forbidden transition and make it dominant over all other competing processes. This is especially challenging if one of the competing transitions is a single-photon dipole transition, which will generally be faster by 1-2 orders of magnitude.

Control over forbidden transitions represents a fundamental challenge, which to our knowledge has not been addressed, and has almost never even been considered, mainly because it is hard to get forbidden transitions to happen in the first place. Nevertheless, it is a very attractive goal because it allows for the systematic design of new classes of emitters. It allows one to design an emitter which prefers to decay via multipolar or spin-forbidden transitions, allowing one to tune the radiation pattern of an emitter and re-shape the radiative interactions between different emitters. It allows one to create emitters which prefer to emit multiple entangled photons simultaneously, rather than a single photon, which could potentially lead to new sorts of on-demand sources of single photons and entangled photons [91]. It will also allow us to take a single emitter and use it to emit radiation with a tunable frequency and angular spectrum, giving a fundamentally new degree of freedom in the design of emitters.

As we show here, an emerging class of photonic materials may provide a route to solve this problem. Polar dielectrics like hexagonal boron nitride (hBN) and silicon carbide (SiC) have been the subject of significant attention over the past two years due to their ability to confine electromagnetic energy in small volumes (on length scales potentially as short as 1 nm), just like plasmons in 2D materials [92, 93, 94, 95, 96, 97, 98, 99, 100, 101, 102, 103, 104]. Unlike plasmon-polaritons, phonon-polaritons (SPhPs) in these materials have strong confinement over a very narrow spectral band (in planar systems) in addition to much lower losses than has been achieved in plasmonics [105].

In this work, we study the consequences of narrow-band strongly confined light for quantum nanophotonics. In particular, we show that phonon polaritons allow for the ability to access forbidden transitions with extremely high efficiency. We show that multipolar transitions and multipolariton emission processes can be made dominant over all other competing transitions. In the process, we develop a general formula to describe the emission of  $N$ -photons over a broad spectrum by an atomic or molecular emitter, with the effects of material dissipation fully incorporated. As a special case, we show how this allows for a new kind of quantum optics source, emitting entangled pairs and with efficiency above 95%, in contrast to  $10^{-10}\%$  in free-space. Our results may allow for the possibility of ushering in new classes of quantum emitters with tunable multipolarity and/or tunable emission spectra, in addition to new materials for broad-band absorption and emission, new capabilities for IR spectroscopy, sensing platforms, and many other applications.

## 4.2 Quantum Electrodynamics of Phonon Polaritons and General Scheme for High-Efficiency Forbidden Transitions

The general scheme for accessing high-efficiency forbidden transitions is illustrated in Figure 1. In free-space (or even near 2D plasmons), an emitter given a choice between different transition pathways will take the single-photon E1 transition over other choices. However, if we have strongly confined modes over a small frequency band, then we can easily create a situation in which the single-photon E1 transition is negligibly enhanced while a forbidden transition is strongly enhanced, so much so that this transition is strongly preferred.

In order to translate our intuition to an exact quantitative theory, we develop a

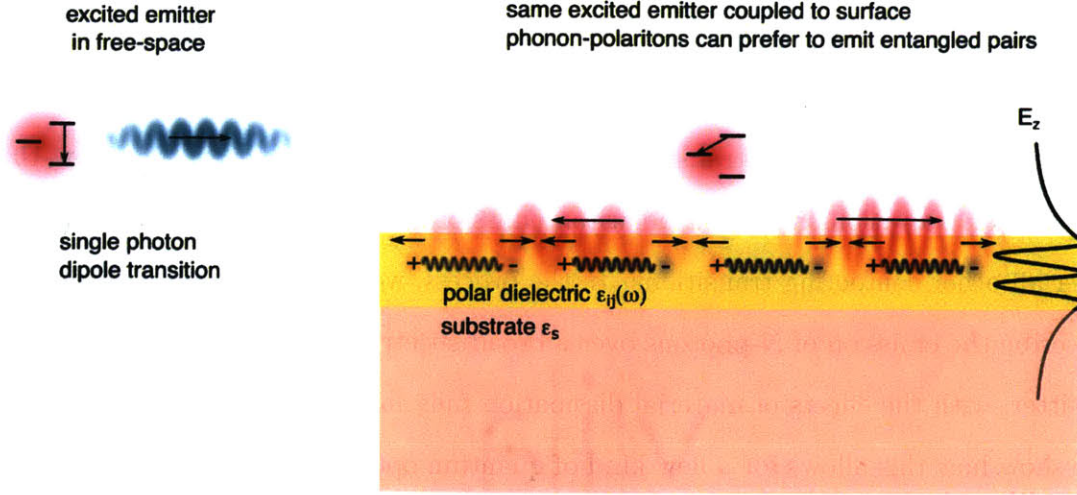


Figure 4-1: **General scheme for accessing forbidden transitions at very high efficiency:** (Left) Typical situation for an emitter (even when coupled to plasmons): an emitter may have many choices for a transition, but the relatively high-frequency single-photon dipole transition is chosen. (Right) When coupling that same excited electron to SPhPs in a (potentially anisotropic) polar dielectric, the electron can be made to prefer a forbidden transition in the IR (e.g; two-polariton spontaneous emission).

formalism to compute the rates of various forbidden transitions for emitters placed near films supporting SPhP modes and compare them to the rates of nearby non-degenerate transitions (because in multielectron atoms, the degeneracies are broken). To capture multipolar emission and multiphoton emission in the same formalism, fully quantum calculations are necessary. The results presented in this paper take losses into account rigorously through the formalism of macroscopic QED that we extend to describe SPhPs.

Light-matter interaction is characterized by an interaction Hamiltonian [42]

$$H_{int} = \frac{e}{2m}(\mathbf{p} \cdot \mathbf{A} + \mathbf{A} \cdot \mathbf{p}) + \frac{e^2}{2m} \mathbf{A}^2, \quad (4.1)$$

where the vector potential operator in the presence of losses is given by [106]:

$$A_i(\mathbf{r}) = \sqrt{\frac{\hbar}{\pi\epsilon_0}} \int d\mathbf{r}' d\omega' \frac{\omega'}{c^2} \sum_{k'} \sqrt{\text{Im } \epsilon(\mathbf{r}', \omega')} \left( G_{ik'}(\mathbf{r}, \mathbf{r}', \omega') \hat{f}_{k'}(\mathbf{r}', \omega') + \text{H.c} \right), \quad (4.2)$$

where  $G_{ik'}(\mathbf{r}, \mathbf{r}', \omega')$  is the dyadic Green function of the Maxwell equations for the system presented on the right side of Figure 1. For the low losses characteristic of phonon-polaritons (and even often plasmon-polaritons), decay rates can be obtained with reasonable accuracy by neglecting the losses and writing the field operators in the form of an expansion over plane-wave phonon-polariton modes. We discuss this effective mode expansion in more detail in the Supplementary Materials (Appendix D). The vector potential in the lossless limit takes the form:

$$\mathbf{A} = \sum_{\mathbf{q}} \sqrt{\frac{\hbar}{2\epsilon_0\omega_q}} (a_{\mathbf{q}}\mathbf{F}_{\mathbf{q}} + hc) \quad (4.3)$$

The modes  $\mathbf{F}_{\mathbf{q}}$  satisfy  $\nabla \times \nabla \times \mathbf{F}_{\mathbf{q}} = \epsilon(\omega)\frac{\omega^2}{c^2}\mathbf{F}_{\mathbf{q}}$  and are normalized such that  $\frac{\hbar\omega}{2\epsilon_0} = \int d\mathbf{r}\mathbf{F}_{\mathbf{q}} \cdot \frac{1}{2\omega} \frac{d(\epsilon\omega^2)}{d\omega} \cdot \mathbf{F}_{\mathbf{q}}$ . This normalization can be proven rigorously to be consistent with canonical commutation relations for the modes from a Green function formalism, as is done in Appendix A. In the limit where there is no dissipation, these two expressions for the vector potential operator generate equivalent decay rates, as can be shown by writing the Green function in the limit of no losses. The advantage of the Green function expression is generality and the ability to characterize the impact of quenching on decay rates. The advantage of the lossless formalism is that it emphasizes the fact that the emission is into modes, and from this, we can easily extract information such as the angular spectrum of emitted phonon-polaritons, as we do in Section 4. We use both formalisms throughout this work.

In multi-photon calculations where the dipole approximation is appropriate, a much more convenient choice of interaction Hamiltonian and is given by  $H_{int} = -\mathbf{d} \cdot \mathbf{E} + \text{self-energy}$ , where the self-energy term has no creation or annihilation operators and is thus irrelevant to our calculations. In the aforementioned gauge,  $\mathbf{E}_{\mathbf{q}} = i\omega\mathbf{A}_{\mathbf{q}}$ .

### 4.3 Phonon-polaritons allow for creating preferentially non-dipolar emitters

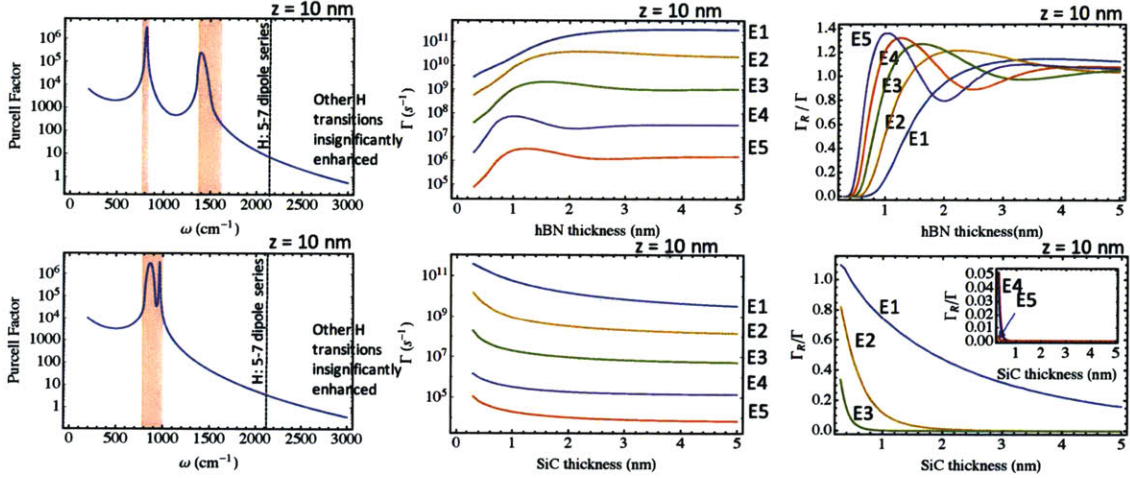


Figure 4-2: **High-Efficiency Access to Multipolar Transitions:** Comparison of the potential for phonon-polariton materials to force an electron to prefer decay via multipolar transitions in hBN (hyperbolic) and SiC (non-hyperbolic). (a,d) Purcell factors for a z-polarized dipole 10 nm away from hBN (a)/SiC (d), which is used to estimate the rates of competing dipole transitions. (b, e) Decay rates for multipolar transitions E1-E5 for an emitter 8 and 10 nm away from the surface of hBN (b)/SiC (e). (c,f) Radiative efficiencies of multipolar transitions in hBN (c) and SiC (f) for an emitter 10 nm away from the surface.

We start by showing that it is possible to have an excited electron have as its dominant decay mechanism a multipolar single photon transition (even for multiplicities as high as E5). In this section and the next, we consider a hydrogen atom for calculational simplicity. Of course, the general principle for enabling high-efficiency access to forbidden transitions is independent of whether or not the atom in question is hydrogenic, and thus our findings apply to a wide array of atoms, molecules, and artificial atoms (quantum dots/wells/wires).

In Figure 2, we compare the potential of hyperbolic (Figures 2a-2c) and non-hyperbolic (Figures 2d-2f) phonon-polariton materials for access to high-order multi-

polar transitions at high efficiency. In all of our calculations, the optic axis of hBN is taken along the direction that the thickness is measured (z-direction). For concreteness, we consider the series of hydrogenic transitions  $7\{p, d, f, g, h\} \rightarrow 6s$  at  $12.4 \mu\text{m}$ . for 4H-SiC (isotropic) and hBN (hyperbolic). These transitions are respectively E1 (dipole), E2 (quadrupole), E3 (octupole), E4 (hexadecupole), and E5 (32-pole). In Figures 2(a) and 2(d), we plot the p-polarized Purcell spectra for a dipole emitter oriented in the z-direction (perpendicular to 5 nm thick hBN (Fig. 2a) or 5 nm thick SiC (Fig. 2d)), 10 nm above hBN/SiC in order to estimate the rates of competing dipole transitions. The Purcell spectra of course has a large peak in the Reststrahlen (RS) bands (highlighted orange in the figures), but is nonzero outside of the RS bands due to losses. For both hBN and SiC, the fastest transition in competition with a 7-6 transition is the 7-5 E1 transition with a lifetime of roughly  $1 \mu\text{s}$ , which has been enhanced roughly an order of magnitude by losses.

In Figure 2(b), we plot the transition rates of E1-E5 7-6 transitions for hydrogen above hBN as a function of hBN thickness. We find that for each transition, there is an optimal thickness. At these thicknesses, even the E4 transition is faster than the 7-5 E1 transition, and the E5 transition is competitive with the 7-5 E1 transition. The 7-6 transition in hydrogen also coincides with the RS band of SiC. In Fig. 2(e), we plot the rates of E1-E5 transitions in SiC as a function of SiC thickness and we see that the decay rates decrease rapidly with increasing thickness for low thicknesses, which is consistent with our finding that the rate of a radiative  $E_n$  transition scales with thickness,  $d$ , like  $\frac{1}{d^{3+2n}}$ . The decrease stops at larger thicknesses due to losses.

It is important to understand what part of the decay comes from coupling to propagating modes and what part comes from quenching. Even though phonon polaritons have relatively low loss, the effects of losses (quenching) can be amplified by bringing an emitter sufficiently close to a surface. To this end, we define a quantity we call the radiative ratio,  $r$ , which we define as the ratio of the decay rate computed assuming

no losses to the decay rate computed with losses taken into account. It is a measure of the extent to which quenching dominates the decay dynamics. A low  $r$  value suggests strong loss-dominated decay. We note that this number can be larger than 1, and this is simply because decay into lossy channels and decay into propagating modes aren't completely independent of each other.

In Figures 2c and 2f, we consider the radiative efficiencies of multipolar decays for the  $n = 7$  states in hydrogen for hBN (Fig. 2c) and SiC (Fig. 2f) as a function of hBN and SiC thicknesses ranging from 0.3 to 5 nm. For hBN, we find that at thicknesses above 1 nm, the radiative efficiencies are around unity, while for SiC, the radiative efficiencies drop drastically as a function of SiC thickness and at 1 nm only the dipole and quadrupole transitions have efficiencies above 10%, while at 0.5 nm, only the E1, E2, E3 transitions have efficiencies above 10%. What accounts for this drastic difference between hBN and SiC? Hyperbolicity. The decay rates for transitions of any multipolar order are proportional to  $\int dq q^k e^{-2qz_0} \text{Im } r_p(q, \omega)$  where  $r_p(q, \omega)$  is the p-polarized reflectivity of the air-polar dielectric-substrate system at the transition frequency,  $q$  is a wavevector, and  $z_0$  is the emitter-surface separation. This integral splits up into two parts – a pole contribution centered at the value of  $q$  satisfying the dispersion relation, and a broad background which peaks around  $\frac{1}{z_0}$ . This broad background vanishes in the absence of dissipation and can be qualitatively understood as the part of the decay rate coming from losses. Losses dominate when  $\frac{1}{z_0} \gg q$ . In hyperbolic systems like hBN, high-order resonances can exist at  $q$  near  $\frac{1}{z_0}$ , meaning that losses do not dominate. On the other hand, in non-hyperbolic systems with thickness on the order of  $\frac{1}{z_0}$ , there are no modes there generally, and losses will dominate.



## 4.4 Phonon-polaritons allow for creating emitters which preferentially emit entangled pairs of photons with a highly tunable frequency and angular spectrum

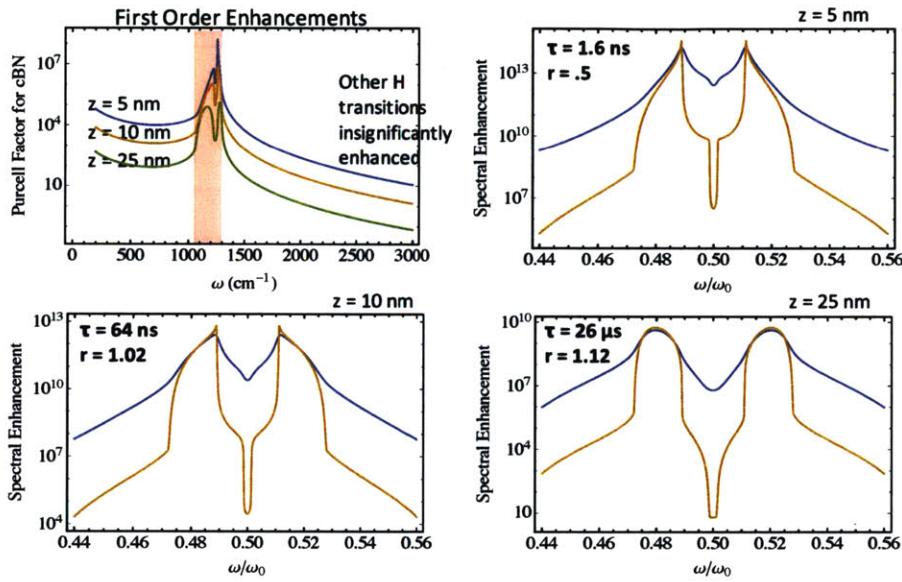


Figure 4-3: **Making two-polariton emission dominant through phonon-polaritons.** (a) Purcell spectra for a  $z$ -polarized dipole above cBN at atom-surface separations of 5, 10, and 25 nm. (b, c, d). Two-photon Purcell spectra for a spherical emitter as a function of photon frequency  $\omega$  for the same set of atom-surface separations. Blue denotes the Purcell spectra with losses accounted for and the orange denotes the Purcell spectra with 100x weaker losses. In each of (b,c,d) both the overall two-photon transition rate between the 5s and 4s states of hydrogen and the radiative ratio of the transition are noted.

In this section, we show that it is possible for an excited electron to have two-photon spontaneous emission as its dominant transition. Moreover, we show that it is possible to create a preferential emitter of entangled photons whose angular and frequency spectrum is highly tunable through knobs such as atom-surface separation, substrate index, emitter frequency, and even the detailed electronic structure of the

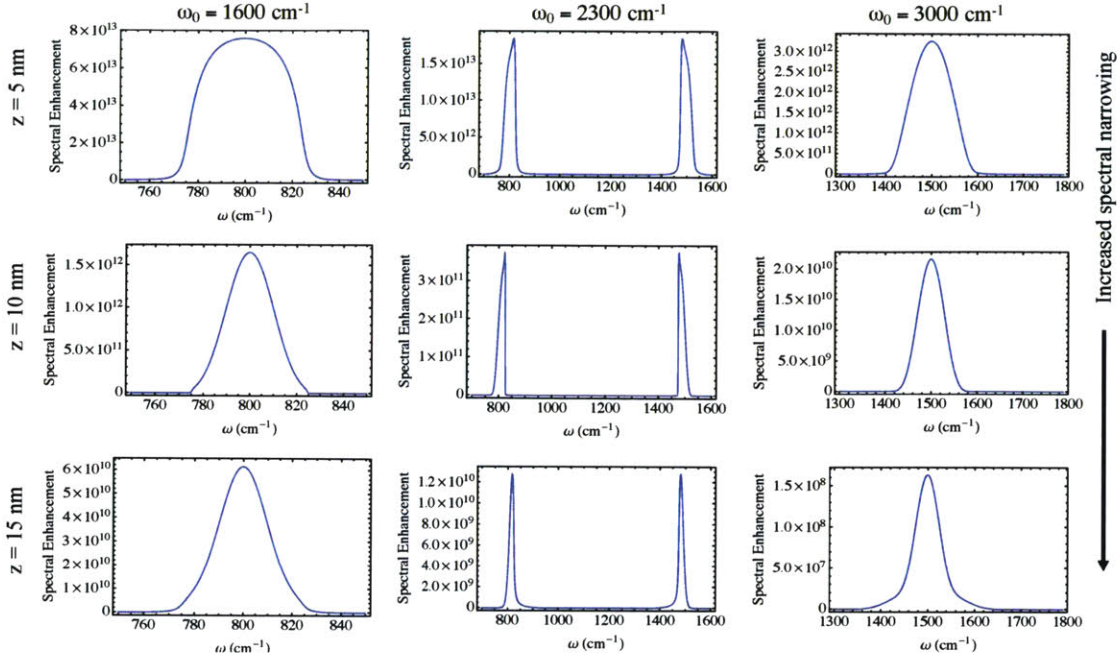


Figure 4-4: **General Features of Two-Polariton Emission: Purcell Spectra.** Two-polariton Purcell spectra defined as in Equation (3) for a spherical emitter as a function of emitter frequency (1600 (left), 2300 (center), and 3000 (right)  $\text{cm}^{-1}$ ) and emitter separation (5 (top), 10 (center), and 15 (bottom) nm). Hyperbolicity allows for enhancement over a large range of frequencies compared to isotropic systems. Moreover, distance can be used to tune the width of the spectrum.

orbitals participating in the transition.

Heuristically, a preferential emission of entangled photon pairs will happen when there is no SPhP mode at the frequency of competing one-photon transitions, while there is an SPhP mode at roughly half of the frequency of the transition in question. We consider an electron which is first put into the hydrogenic 5s state and we consider the rate of decay into the 4s state by two-polariton spontaneous emission into cBN phonon polaritons. The frequency of the transition is  $2468 \text{ cm}^{-1}$  while the RS band of cBN is between  $1052$  and  $1303 \text{ cm}^{-1}$ . In Figure 3a, we compute the Purcell-spectra for a first-order dipole transition for atom-surface separations of 5, 10, and 25 nm to get an order of magnitude estimate for the rates of the competing dipole transitions at first order. At 5 nm, the fastest competing transition occurs with a lifetime of

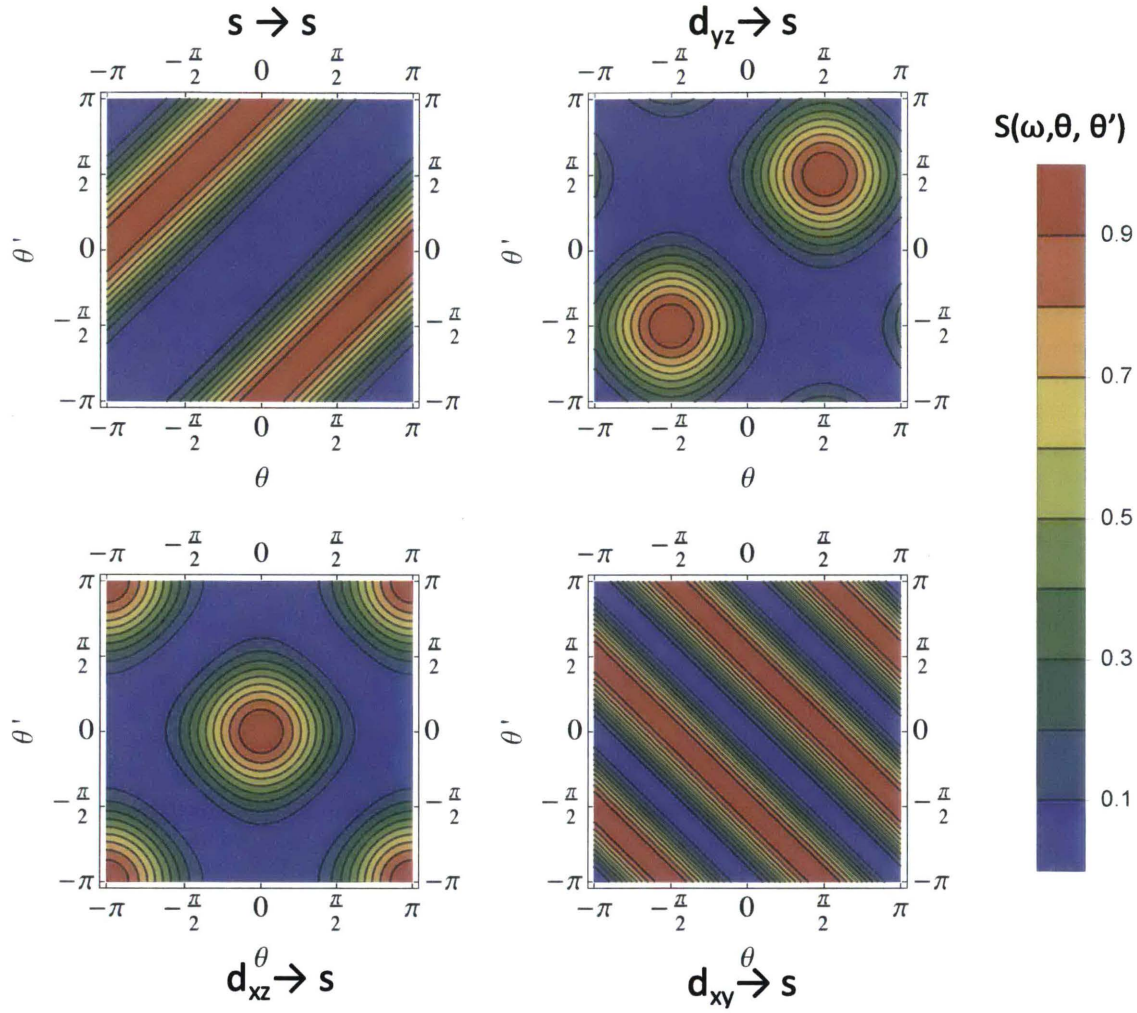


Figure 4-5: **Wavefunction shaping and the Angular Spectrum of Entangled Radiation:** Plots of the angular spectrum  $S(\omega_0/2, \theta, \theta')$  as a function of the initial state of the electron for initial states  $s, d_{xy}, d_{xz}, d_{yz}$ .

order 100 ns. At 10 and 25 nm, the order of magnitude is closer to 1 us. In Figures 3(b-d), we compute the spectrum of two-photon emission from 5s-4s (due to cBN phonon-polaritons), in addition to the lifetime of the two-photon transition and the radiative efficiency.

To do this computation, we make use of the general result that for an  $s \rightarrow s$  transition, the spectral enhancement factor, defined as the ratio of the SPhP emission

spectra,  $\frac{d\Gamma}{d\omega}$ , to the free-space emission spectrum  $\frac{d\Gamma_0}{d\omega}$  is given by:

$$\text{Spectral Enhancement} = \frac{\frac{d\Gamma}{d\omega}}{\frac{d\Gamma_0}{d\omega}} = \frac{1}{2} F_p(\omega) F_p(\omega_0 - \omega), \quad (4.4)$$

where  $F_p(\omega)$  is the Purcell factor for a dipole perpendicular to the surface and is related to the imaginary part of the reflectivity of the air-polar dielectric-substrate system by  $F_p(\omega) = \frac{3}{2k_0^3} \int dq q^2 e^{-2qz_0} \text{Im } r_p(q, \omega)$ , where  $k_0$  is the free-space photon wavevector,  $\frac{\omega}{c}$  [107]. We derive this result in the Supplementary Information by computing the spectrum of emission of  $N$  photons (with losses included) and taking the special case  $N = 2$ .

In Figures 3(b-d), we see that the lifetimes of two-photon spontaneous emission for an emitter 5, 10, and 25 nm away from the surface of 10 nm thick cBN are 1.6 ns, 65 ns, and 25  $\mu$ s, respectively. Their radiative efficiencies are 0.5, 1.02, and 1.12, respectively. Thus, two-photon spontaneous emission into phonon-polaritons can have an over 95% quantum efficiency. In free-space, two-photon spontaneous emission is roughly 10 orders of magnitude slower. We thus conclude that using phonon-polaritons, it is possible to create a source of a pair of entangled photons at very high efficiency. We now move on to describing the spectral properties of this new quantum light source, both in frequency and angle.

In Figure 4, we consider the spectral enhancement defined above in hBN as a function of emitter frequency ( $\omega_0 = 1600, 2300, 3000 \text{ cm}^{-1}$ ) and emitter-surface separation ( $z_0 = 5, 10, 15 \text{ nm}$ ). We choose a different material than that of Figure 3 to show that two-photon spectral enhancements similar to those in thin cBN are achievable in other materials and also to show a large number of frequency bands where a two-photon emitter can be created. What we see from Figure 4 is that hBN offers very high spectral enhancement in three different frequency bands, as opposed to one in isotropic polar dielectrics. The spectral enhancement at 5 nm is of the same order

of magnitude as that in cBN. The reason is intercombination: a two-photon emission through near-field polaritons can occur via two photons in the lower RS band, two photons in the upper RS band, or one in the upper RS band and one in the lower RS band. A material having three separate RS bands would offer six frequency ranges for two-photon emission. We also find from Figure 4 that increasing the emitter separation causes the emission spectrum not only to be weaker, but also narrower (by about a factor of 2 when goes from 5 nm to 15 nm) . This allows one to tune not only the emission rate but also the emission spectrum with atom-surface separation.

Finally, we consider the angular spectrum of emitted photons. In the supplementary information, we derive the general result that the angle and frequency spectrum of two-photon emission,  $S(\omega, \theta, \theta')$  is proportional to:

$$S(\omega, \theta, \theta') \sim \left| \sum_{ij} \hat{e}_i^*(\theta) \hat{e}_j^*(\theta') T_{ij}(\omega) \right|^2, \quad (4.5)$$

where  $T_{ij}(\omega) = T_{ji}(\omega_0 - \omega) = \sum_n \left( \frac{d_i^{gn} d_j^{ne}}{E_e - E_n - \hbar\omega} + \frac{d_j^{gn} d_i^{ne}}{E_e - E_n - \hbar(\omega_0 - \omega)} \right)$ , where  $d^{ab}$  denotes a dipole matrix element between states  $a$  and  $b$ ,  $n$  denotes an intermediate atomic state,  $g$  denotes the ground state,  $e$  denotes the excited state, and  $E_i$  is the energy of the  $i$ th state. The  $\hat{e}_i(\theta)$  are the phonon-polariton polarizations in the vicinity of the emitter, given by  $\frac{1}{\sqrt{2}}(\cos \theta, \sin \theta, i)$

This dependence will lead to qualitatively different angular spectra for different transitions. In Table 4.1, we show the angular spectrum as a function of different transitions. Strictly speaking, the angular spectrum is frequency dependent. However, due to the narrowness of the Reststrahlen band, this can be neglected. Remarkably, simply by changing the initial state of the system, one can change whether the entangled pairs are preferentially emitted in the same direction, as in Fig. 5(b,c) or in opposite directions, as in Fig. 5a. The key results of this section is that: using highly confined, narrow-band phonon-polaritons, it is possible to have an electron prefer to

Transition	Angular Spectrum
$s \rightarrow s$	$\sin^4\left(\frac{\theta-\theta'}{2}\right)$
$d_{xy} \rightarrow s$	$\sin^2(\theta + \theta')$
$d_{xz} \rightarrow s$	$(\cos \theta + \cos \theta')^2$
$d_{yz} \rightarrow s$	$(\sin \theta + \sin \theta')^2$

Table 4.1: A summary of the dependence of the angular spectrum of two-polariton radiation as a function of initial and final electronic states for a few selected initial electronic states.

decay via the emission of a pair of entangled photons. Moreover, it is possible to do this at many frequency ranges in the mid IR, especially in anisotropic materials such as hBN, due to their multiple Reststrahlen bands. The frequency spectrum of such a source of entangled near-field photons can be reshaped by emitter frequency and emitter-surface separation. Finally, coherent effects arising from electronic structure give us a surprisingly rich degree of freedom to tune the angular shape of the radiation. For some initial and final orbital configurations, it is possible to have the entangled pairs prefer to go in the same direction, while in others, pairs strongly prefer to travel in opposite directions.

## 4.5 Summary

In summary, we have shown that the unique combination of extremely high confinement factors (over 200) and a narrow, but not too narrow spectral range allows for the design of emitters fundamentally different than any that have been realized before. We can use phonon-polaritons to design emitters which preferentially emit via multipolar transitions at quantum efficiencies exceeding 90%, allowing us to reshape the radiation of emitters and the radiative interaction between different emitters. We found that this effect can happen both in hBN and in thin polar dielectrics, although in hBN, the emission is much more radiatively pure, due to hyperbolicity. Moreover, using this general technique of extremely high confinement over a narrow spectral

range, we can also design emitters which preferentially decay via the emission of entangled pairs of near-field photon, again with quantum efficiencies exceeding 90%. We found that this can be realized over many frequency ranges in the mid-IR, that the frequency spectra are relatively broad and tunable, and that coherent quantum effects can completely reshape the angular spectrum of emission of these entangled pairs.

As all atoms have electronic transitions in the mid-IR, our results should apply to a large portion of the periodic table. It may also be possible that vibrational transitions may be used to observe these effects, although one obstacle towards realizing these effects with molecular vibrations is the generally low multipole moments associated with vibrational transitions (1 D dipole moments for example). We believe that these results have direct implications for: spectroscopy for inferring electronic transitions which cannot be determined with photons, sensors based on forbidden transitions, quantum optics (on-demand generation of single photons and entangled pairs of photons), turning narrow-band emitters into broadband emitters, turning narrow-band absorbers into broadband absorbers, and fundamentally being able to reshape the optical properties of materials.





# Chapter 5

## Summary and Outlook

Tying everything back together, the aim of this thesis was to address the fundamental question:

*What physics can be realized by tailoring the coupling between a state and a continuum?*

We explored this fundamental question in the context of resonances associated with separable bound states in the continuum and showed that using tailored perturbations of bound states in the continuum associated with separable Hamiltonians, it is possible to control the directionality by which radiation propagates, and also the number of dimensions that the radiation is confined in. In terms of applications, we can say that by tailoring the couplings between a BIC and its degenerate continuum, it is possible to tailor the fundamental properties of radiation. By controlling the directionality of radiation, we can create a switch that traps a wave and releases it into a direction of choice. Moreover, by controlling the dimensionality of radiation, it should be possible to create an electronic system which can be switched between being confined in 1D, 2D, and 3D (i.e; having quantum well, quantum wire, and quantum dot modes of operation). Our findings can be realized both in Schrodinger or Maxwell equations. We showed that this physics can be realized in optical potentials

for ultracold atoms, photonic lattices, and in photorefractive media.

We also explored this fundamental question in the context of nonrelativistic quantum electrodynamics. We showed that we could shape the continuum that an excited electron couples to by changing the properties of the electromagnetic mode quanta (photons or polaritons, depending on your taste). These properties include wavelength, the dispersion relation (equivalently, density of modes), polarization, and phase. In chapters three and four, on plasmon-polaritons and phonon-polaritons, we were primarily concerned with the modification of wavelength.

In particular, we showed for the first time that because of the extremely short wavelength plasmons associated with plasmons in 2D materials such as graphene, monolayer silver, DySi<sub>2</sub>, and others, that it is possible to overcome all of the basic selection rules of atomic physics: electric multipole transitions, multiplasmon spontaneous emission, and spin-flip transitions can all be made to occur fast. Certainly faster than many dipole transitions in free-space. The potential applications of this work include: spectroscopy for inferring electronic transitions which cannot be determined with photons, sensors based on forbidden transitions, organic-light sources arising from fast singlet-triplet transitions, fast entangled light generation, and fast generation of broadband light with tunable width in the visible or IR.

We then showed for the first time that using highly confined phonon-polaritons over a narrow frequency range, it is not only possible to allow forbidden transitions (as we showed also with plasmons) but that it is possible to make them the fastest decay process for an excited electron. We showed this with multipolar transitions and two-photon spontaneous emission processes. We showed that multipole transitions like E3 transitions and two-photon spontaneous emission processes can be up to 20 times faster than a competing dipole transition when phonon-polaritons become involved.

This is remarkable when you realize that in free-space and in most photonic systems, these same processes are roughly  $10^8 - 10^{12}$  times slower than competing dipole

transitions and can always be neglected. Now, we can design quantum emitters of light based on these transitions! We characterized the properties of a potential high-efficiency source of entangled pairs of photons and found that their frequency spectra can be tuned and even that their angular spectra can be drastically altered. We can either make a source where the emitted pairs of photons prefer to be 180 degrees apart, or where they prefer to move together. This shows us that the power spectrum of emission depends strongly on the detailed shape of the electron wavefunction.

In the process of arriving at these results, we derive a general formula for the emission of  $N$ -photons in a lossy medium in terms of the Purcell factor for one-photon emission, establishing a link between the huge literature on the Purcell effect and multiphoton processes in nanophotonics. This allows us not only to estimate the rates of multiphoton processes in many systems, but also to derive exactly the effect of quenching at higher-order in perturbation theory, which to our knowledge has not been explored.

By the way, on a fundamental note, having multiphoton spontaneous emission as a dominant (or even competing process) is interesting, because it goes against one of the fundamental things that we learn about atomic spectra (coming from atomic bound states), which is that they are discrete. Usually their discreteness is attributed to the discreteness of atomic levels, but that is an insufficient criterion when multiphoton processes cannot be neglected. This realization gives us a hint that we can manipulate the seemingly fundamental optical properties of atoms, molecules, and more complicated materials via nanophotonics.

There are many directions that one could conceivably pursue as a result of this work. For example, the work done here focused purely on atomic emitters as a proof-of-concept. But this is not necessary. I believe that combining this work in nanophotonics with the great variety of electronic systems afforded by molecular and solid-state systems should almost certainly lead to developments in observing new

light-matter interactions.

I conclude this thesis by presenting a vast frontier of exploration that would logically follow the developments presented in this thesis. The basic theme that I want to explore here is that the optical properties of materials are strongly dependent on the allowed transitions in those materials. By enabling many more transitions, the optical response of materials at nanometer distances from plasmon-polaritons and phonon-polaritons should be drastically altered. Here are some interesting questions based on this intuition that I think are worth exploring:

Is it possible to allow materials to absorb over a much wider range of frequencies because of the availability of forbidden transitions? Remember, most transitions are forbidden by electronic selection rules. On the more applied side, it is possible using this enhanced absorption over many more frequencies to create an absorbing material which absorbs strongly over only a few nanometers?

Is it possible to turn a system that absorbs over discrete frequencies and make it absorb over a continuum due to highly enhanced two-photon absorption? This is interesting because it allows us to turn a narrow-band absorber into a broad-band absorber, potentially leading to new materials for the absorption and conversion of solar energy.

If it is possible to have an atom prefer to emit two-photons over one, then is it possible to create a material out of these atoms that has a higher nonlinear susceptibility than its linear susceptibility? This would allow us to take make nonlinear materials out of conventionally linear materials.

There are many more questions we could ask, but we'll stop here. I truly believe that the work done here is pointing to the possibility of developing a new field: nanophotonics-enabled tailoring of the optical response of materials. One where the (optical) properties of materials aren't a fixed thing, but things that we can control and perhaps even deform in a way such that the new properties hardly resemble the

old properties.



# Appendix A

## Light-Matter Interactions in

## Photonics: Macroscopic Quantum

## Electrodynamics

In this section, we outline the formalism for considering the interaction between electrons and the electromagnetic modes of spatially inhomogeneous, dispersive, dissipative, and potentially anisotropic media. We start by discussing the minimal coupling Hamiltonian by which light and matter interact and then we discuss the construction of field operators based on the modes of the underlying Maxwell equations. We start by presenting our results in the case of lossless dielectric media to provide the reader with intuition. Then, we briefly discuss quantization in the lossy dielectric media.

The interaction Hamiltonian,  $H_{int}$  between light and matter (such as an electron in an atom) is given by the minimal coupling Hamiltonian:

$$H_{int} = \frac{e}{2m}(\mathbf{p} \cdot \mathbf{A} + \mathbf{A} \cdot \mathbf{p}) + \frac{e^2}{2m} \mathbf{A}^2, \quad (\text{A.1})$$

where  $\mathbf{p}$  is the electron momentum operator and  $\mathbf{A}$  is the vector potential operator. In order to describe effects where the quantum nature of the fields are important

(such spontaneous emission processes, which are a main focus of our work), we need a quantized vector potential operator. This is the purpose of this appendix.

## A.1 Maxwell's Equations: Basic Properties

The Maxwell Equations, after doing a Fourier transform in time, read:

$$\nabla \cdot \mathbf{D}(\mathbf{r}, t) = \frac{\rho_f}{\epsilon_0} \leftrightarrow \nabla \cdot \mathbf{D}(\mathbf{r}, \omega) = \frac{\rho_f}{\epsilon_0} \quad (\text{A.2})$$

$$\nabla \cdot \mathbf{B}(\mathbf{r}, t) = 0 \leftrightarrow \nabla \cdot \mathbf{B}(\mathbf{r}, \omega) = 0 \quad (\text{A.3})$$

$$\nabla \times \mathbf{E}(\mathbf{r}, t) = -\frac{\partial \mathbf{B}}{\partial t} \leftrightarrow \nabla \times \mathbf{E}(\mathbf{r}, \omega) = i\omega \mathbf{B}(\mathbf{r}, \omega) \quad (\text{A.4})$$

$$\nabla \times \mathbf{H}(\mathbf{r}, t) = \mathbf{j}_f + \frac{\partial \mathbf{D}}{\partial t} \leftrightarrow \nabla \times \mathbf{H}(\mathbf{r}, \omega) = \mathbf{j}_f - i\omega \mathbf{D}(\mathbf{r}, \omega), \quad (\text{A.5})$$

where the auxiliary fields are related to the usual fields by  $\mathbf{D} = \epsilon \mathbf{E}$  and  $\mathbf{B} = \mu \mathbf{H}$ . The  $f$  subscript denotes free quantities (i.e;  $\mathbf{D}$  and  $\mathbf{H}$  are sourced by free charge and free current). Throughout the entirety of this text we shall work in frequency-domain rather than time-domain. Using these equations and working in frequency-domain, the normal modes of the fields can be seen to be determined by an eigenvalue problem. Assume no free charge or current. It thus follows that:

$$\nabla \times \nabla \times \mathbf{E} = \epsilon \frac{\omega^2}{c^2} \mathbf{E}. \quad (\text{A.6})$$

We are mostly interested in equation (A.6). The electric-field eigenproblem, (A.6), is a generalized Hermitian eigenproblem with the following properties:

1. If  $\epsilon$  is real, and non-dispersive, then (8) is Hermitian under the inner product  $(m|n) \equiv \int d\mathbf{r} \epsilon \mathbf{E}_m^* \cdot \mathbf{E}_n$  for square-integrable functions. They are typically taken to be orthonormal.



2. Completeness:  $\sum_m \epsilon(\mathbf{r}') E_{m,i}^*(\mathbf{r}') E_{m,j}(\mathbf{r}) = \delta_{ij} \delta(\mathbf{r} - \mathbf{r}')$ ,

where  $m$  labels the modes. The completeness allows us to express any electric field in terms of these eigenfunctions. We're going to use the complex electric field. Eventually, when we need a real field operator, we'll take the real part of our complex fields, the latter of which are given by:

$$\mathbf{E} = \sum_n \alpha_n \mathbf{E}_n e^{i\omega_n t} = \alpha_n(t) \mathbf{E}_n. \quad (\text{A.7})$$

The real electric field is given by  $\text{Re } \mathbf{E} = \frac{1}{2} \sum_n \alpha_n \mathbf{E}_n e^{i\omega_n t} + \alpha_n^* \mathbf{E}_n^* e^{-i\omega_n t}$ .

## A.2 Quantization of Lossless Electromagnetic Modes: Heuristic Approach

In what follows, we're going to canonically quantize the fields of complex dielectric media (with no loss or dispersion) by establishing an analogy between the dynamics of these field modes and the dynamics of harmonic oscillators. First, we notice that:

$$\dot{\alpha}_n + i\omega_n \alpha_n = \dot{\alpha}_n^* + i\omega_n \alpha_n^* = 0 \quad (\text{A.8})$$

Notice that these are extremely similar to the Heisenberg equations of motion for the annihilation and creation operators of a harmonic oscillator of frequency  $\omega_n$  (just with expansion coefficients instead of operators). We thus guess that *that in order to canonically quantize the electromagnetic field, we should replace  $\alpha_n$  by  $a_n$  and  $\alpha_n^*$  by  $a_n^\dagger$* . As a consistency check, let's attempt to derive the Hamiltonian of the system. For our time-invariant optical system (epsilon doesn't depend on t), we expect that the conserved time-averaged energy should be the classical Hamiltonian of the free field.

The time-averaged energy is given by [108]

$$\frac{1}{2} \int d\mathbf{r} \epsilon_0 \epsilon_r(\omega) |N_n|^2 |\mathbf{E}_n|^2, \quad (\text{A.9})$$

where  $N_n$  is a normalization constant which gives the modes units of field (currently, the modes were normalized to 1). Using mode orthogonality, the classical Hamiltonian of the free field is:

$$H = \sum_n \frac{1}{2} \epsilon_0 |N_n|^2 \alpha_n^* \alpha_n \quad (\text{A.10})$$

Replacing the classical expansion coefficients with operators, we get the Hamiltonian of the free field up to a zero-point energy which is irrelevant for our purposes:

$$H = \sum_n \frac{1}{2} \epsilon_0 |N_n|^2 a_n^\dagger a_n \quad (\text{A.11})$$

There is an ordering ambiguity when going from classical quantities to quantum operators. Using the standard normal ordering prescription, we put the creation operators on the left.

What we now have is a Hamiltonian describing infinitely many decoupled oscillators - one for each mode. The excitations of each mode are excitations of the field (called photons). They can also be called dressed photon, because their mode profiles are different than those of free-space photons. Intuitively, each photon has energy  $\hbar\omega_n$ . Setting this equal to  $\frac{1}{2}\epsilon_0|N_n|^2$ , we have that  $|N_n|^2 = \frac{2\hbar\omega_n}{\epsilon_0}$ . Plugging this into the definition of the real-valued electric field, we have that

$$\text{Re } \mathbf{E} = \sum_n \sqrt{\frac{\hbar}{2\epsilon_0}} (a_n \mathbf{E}_n + a_n^\dagger \mathbf{E}_n^*) \quad (\text{A.12})$$

We'll need the real-valued vector potential since it is what appears in the interaction Hamiltonian. Choosing a gauge in which  $\phi = 0$ , the frequency domain vector potential comes from the frequency domain electric field via:  $\mathbf{E} = -\frac{\partial \mathbf{A}}{\partial t}$ .

Later in this appendix, we extend the above to dispersive media. The canonical quantization derivation done here does not apply because the modes can not be shown to be orthogonal in general, which we used to compute the classical Hamiltonian. However, later in this appendix, we show that this problem can be solved in systems with translational symmetry by redefining the inner product. Before doing this, we say a few words about when losses are present.

### A.3 Quantization in Lossy Electromagnetic Media

In lossy media, modes are not a well-defined concept. While there are solutions to the Maxwell equations at complex frequencies, they are not orthogonal, and they are not complete, rendering our above derivation useless. Much attention has been paid to the quantization of electromagnetic fields in lossy media. It is well-reviewed in [106, 109]. The primary physical difference between a formalism which considers losses and one which does not lies in the elementary excitations of the system. In the lossless medium, the elementary excitations can be seen as the modes of the Maxwell equations for that medium. In the lossy situation, modes are not a useful means by which to describe the electric and magnetic fields. On the other hand, they can be still described using Green functions. In particular, the notion of current density is still well-defined in the lossy case, and the fields (after a temporal Fourier transform) are simply given by:

$$E_i(\mathbf{r}, \omega) = \int d\mathbf{r}' G_{ij}(\mathbf{r}, \mathbf{r}', \omega) j_j(\mathbf{r}', \omega). \quad (\text{A.13})$$

As we can see, the fields are completely specified by knowing the polarization, position, and frequency of current density at every point in space. Therefore, it seems natural for the elementary (bosonic) excitations of the lossy problem to be excitations of current density with position, frequency, and polarization as the degrees of

freedom. As is shown in [106, 109], the field operators, such as the vector potential operator, can be expressed as:

$$A_i(\mathbf{r}) = \sqrt{\frac{\hbar}{\pi\epsilon_0}} \int d\mathbf{r}' d\omega' \frac{\omega'}{c^2} \sum_{k'} \sqrt{\text{Im } \epsilon(\mathbf{r}', \omega')} \left( G_{ik'}(\mathbf{r}, \mathbf{r}', \omega') \hat{f}_{k'}(\mathbf{r}', \omega') + \text{H.c.} \right). \quad (\text{A.14})$$

$G_{ik'}(\mathbf{r}, \mathbf{r}', \omega')$  is the classical Green function of the Maxwell equations, and the  $f$  operators create and annihilate excitations with known position, frequency, and polarization – consistently with the intuition provided above that the elementary excitations are currents and that they are related to the fields by the Green function.

### A.3.1 Limiting Case: A Transparency Window

Here we derive rigorously the result that for quantized electric fields in dispersive media with negligible loss (a transparency window), that they should be normalized such that:

$$\frac{1}{2\omega} \int d\mathbf{r} \frac{d(\epsilon_r \omega^2)}{d\omega} |\mathbf{E}(\mathbf{r})|^2 = \frac{\hbar\omega}{2\epsilon_0} \quad (\text{A.15})$$

A result like this was derived for surface plasmons in [77] and it was shown that this result is consistent with the classical Green's function approach in the lossless limit when both formalisms are used to compute the rate of spontaneous emission of an excited electron in a two-level system. We now show from a quantum Green's function formalism that this needs to be the case not only for plasmons, but also for any 1D, 2D, or 3D translationally invariant system, and that the energy normalization arises from the form of the Green's function in the lossless limit.

We first examine the Green's tensor in the case of 2D translationally invariant media and then extend our results to 1D and 3D (examining all of the cases at once is notationally cumbersome). The Green tensor with outgoing radiation boundary

conditions is defined by:

$$\left( \nabla \times \nabla \times -\epsilon(\mathbf{r}, \omega) \frac{\omega^2}{c^2} + i0^+ \right) \mathbf{G}_i = \hat{e}_i \delta(\mathbf{r} - \mathbf{r}') \quad (\text{A.16})$$

In this equation, we are allowing  $\epsilon$  to be spatially varying, dispersive, and potentially anisotropic. This allows for quantization of plasmons in films and nanowires, modes of hyperbolic metamaterials, and modes of naturally hyperbolic materials like hBN, which support phonon-polariton modes. Writing

$$\begin{aligned} \mathbf{G}_i &= \int \frac{d\mathbf{q}}{(2\pi)^2} e^{i\mathbf{q}\cdot\rho} g_i(\mathbf{q}) \mathbf{F}(\mathbf{q}, z) \equiv \int \frac{d\mathbf{q}}{(2\pi)^2} \mathbf{E}(\mathbf{q}, \mathbf{r}) \\ \delta(\mathbf{r} - \mathbf{r}') &= \int \frac{d\mathbf{q}}{(2\pi)^2} e^{i\mathbf{q}\cdot\rho} \delta(\mathbf{q}, z), \end{aligned} \quad (\text{A.17})$$

where  $\nabla \times \nabla \times \mathbf{E}(\mathbf{q}, \mathbf{r}) = \epsilon(\omega_q) \frac{\omega_q^2}{c^2} \mathbf{E}(\mathbf{q}, \mathbf{r})$  and defining the inner product  $(\mathbf{A}, \mathbf{B}) = \int d\mathbf{r} \mathbf{A}^* \cdot \mathbf{B}$ , we get that:

$$g_i(\mathbf{q}) = c^2 \frac{\hat{e}_i \cdot \mathbf{E}(\mathbf{q})}{\int d\mathbf{r} \mathbf{E}(\mathbf{q})^* \cdot (\epsilon(\omega_q) \omega_q^2 - \epsilon(\omega) \omega^2 + i0^+) \cdot \mathbf{E}(\mathbf{q})}. \quad (\text{A.18})$$

For light-matter interaction processes involving transitions (such as dipole transitions, multipole transitions, many-photon emission processes, etc.), the imaginary part of the Green tensor determines the rates at which these processes happen. In what follows, we will be interested in transparency windows of a material, where dispersion can be high, but the dissipation can be neglected. We refer to this situation as the lossless limit. Physically, the lossless limit of transition rates describes the rate of mode launching, i.e; the rate of the transition not coming from direct coupling to dissipative modes.

In the lossless limit, we have that  $\frac{1}{x+i0^+} = \mathcal{P}(\frac{1}{x}) + i\pi\delta(x)$ . For very low losses, the imaginary part of the Green's function is negligible except in a small window of wave

vectors such that  $\omega_q \approx \omega_0$ . In this limit,  $\text{Im } G$  is well-approximated by

$$\text{Im } G_{ij} = \frac{c^2}{2} \int dq q \frac{F_{\mathbf{q}}^{*i}(\mathbf{r}') F_{\mathbf{q}}^j(\mathbf{r})}{\left| \int dz \mathbf{F}_{\mathbf{q}}^* \cdot \frac{d(\epsilon\omega^2)}{d\omega} \cdot \mathbf{F}_{\mathbf{q}} \right|} \delta(\omega_{\mathbf{q}} - \omega_0). \quad (\text{A.19})$$

Noting that the integral in the denominator is:

$$\omega \int d\mathbf{r} \mathbf{E}_{\mathbf{q}}^* \cdot \left( \frac{d(\epsilon\omega)}{d\omega} + \epsilon \right) \cdot \mathbf{E}_{\mathbf{q}},$$

the fact that  $\nabla \times \mathbf{H} = i\omega\epsilon\mathbf{E}$ , the fact that the fields vanish at  $|z| = \infty$ , and the periodic boundary conditions on  $\mathbf{E}$  and  $\mathbf{H}$ , we have that the denominator is nothing but:

$$\omega \int d\mathbf{r} \mathbf{E}_{\mathbf{q}}^* \cdot \frac{d(\epsilon_r\omega)}{d\omega} \cdot \mathbf{E}_{\mathbf{q}} + |\mathbf{H}_{\mathbf{q}}|^2 \sim U_{EM}, \quad (\text{A.20})$$

Equation (42) thus establishes a general connection between the Greens function, the Purcell factor, and the electromagnetic energy in a transparency window of a dispersive medium. Equation (42) resolves an apparent issue associated with a derivation of the correct normalization for electromagnetic field modes to be used in quantum calculations. The primary issues with a canonical quantization approach in which the energy is written in terms of a sum over modes is that the formula for the energy which appears in equation (42) is invalid for fields with a broad frequency spectrum (relative to the range over which the permittivity varies). This follows from the derivation of the Brillouin formula (equation (42)), which assumes a nearly time-harmonic field [110, 111, 112]. As a result, it is unclear that a quantization scheme based on the energy can apply to broadband electromagnetic fields.

In spontaneous emission processes where a single photon is emitted, the line width is typically much smaller than the emission frequency, and thus it is not so surprising that a quantization scheme based directly on the energy is applicable to describing these processes. On the other hand, when one moves to multi-photon emission pro-

cesses, or even emission by a free electron (as in Cerenkov radiation), both of which cover a broad spectrum of frequencies (comparable to the center of the emission spectrum), it is unclear that this quantization scheme can be applied. By deriving the correct mode normalization based on a quantum Greens function formalism which accounts for dispersion, dissipation, and broadband fields, we show without a doubt that such a quantization scheme is (surprisingly) valid beyond what one might expect.

We conclude by discussing the generalization of our result to other system geometries such as 1D and 3D translationally invariant media. For 1D translationally invariant systems such as nanowires, the Greens function takes the same form as an eigenmode expansion, except over a 1D wavevector space. The z-integral in the denominator in the 2D case turns into an integral over 2D in the 1D case, but the integrand remains the same. In a 3D translationally invariant system, the integral is over all three directions.





# Appendix B

## Supplementary Materials for: Shrinking the Wavelength of Light to Allow Forbidden Transitions

### B.1 Introduction

In this appendix, we outline the use of QED for computing decay rates of atomic excited states due to the vacuum macroscopic electromagnetic fields associated with 2D conductors. We consider atom-field interactions governed by the non-relativistic Pauli-Schrodinger Hamiltonian  $H$ :

$$\begin{aligned} H &= H_a + H_{em} + H_{int} \\ H_a &= \left( \sum_i \frac{\mathbf{p}_i^2}{2m_e} - \frac{e^2}{4\pi\epsilon_0 r_i} \right) + H_{e-e} + H_{SO} \\ H_{em} &= \sum_k \int d\mathbf{r} \int d\omega \hbar\omega \left( f_k^\dagger(\mathbf{r}, \omega) f_k(\mathbf{r}, \omega) + \frac{1}{2} \right) \\ H_{int} &= \sum_i \frac{e}{2m} (\mathbf{p}_i \cdot \mathbf{A}(\mathbf{r}_i) + \mathbf{A}(\mathbf{r}_i) \cdot \mathbf{p}_i) + \frac{e^2}{2m} \mathbf{A}^2(\mathbf{r}_i) + \frac{e\hbar}{2m} \boldsymbol{\sigma}_i \cdot \mathbf{B}(\mathbf{r}_i), \end{aligned} \quad (\text{B.1})$$

where  $H_{e-e}$  is the electron-electron interaction,  $H_{SO}$  is the spin-orbit coupling,  $H_a$  is the atomic Hamiltonian,  $H_{int}$  is the atom-field interaction,  $\mathbf{A}$  is the vector potential operator, and  $\mathbf{B}$  is the magnetic field operator. The operators (and notation) appearing in the field energy, given by  $H_{em}$ , will be explained in Sec. II. The minimal-coupling interaction Hamiltonian presented above is related to the more well-known dipole interaction Hamiltonian:  $-\mathbf{d} \cdot \mathbf{E}$  + self-energy, by a unitary transformation in the long-wavelength (dipole) approximation[79].

Because the atoms that we consider are interacting with dissipative media, the canonical quantization based on the mode expansion of the electromagnetic field is not valid. Instead we must use the formalism of macroscopic QED. For more information about macroscopic QED, see Refs. [106, 109]. We also discuss conditions for which a canonical quantization scheme based on the expansion of lossless modes is a suitable approximation for the decay rate of an excited atom. We choose a fully quantum mechanical approach rather than the well known phenomenological approach based on the LDOS not only because it takes into account the orbital degrees of freedom of the emitter, but also because it provides an elegant way to computing rates of transitions with varying multipolarity.

## B.2 Macroscopic QED of 2D Conductors

Choosing a gauge in which the scalar potential is identically zero, the vector potential operator is given by:

$$A_i(\mathbf{r}) = \sqrt{\frac{\hbar}{\pi\epsilon_0}} \int d\omega' \frac{\omega'}{c^2} \int d\mathbf{r}' \sqrt{\text{Im } \epsilon(\mathbf{r}', \omega')} \mathbf{G}_{ij}(\mathbf{r}, \mathbf{r}'; \omega') \hat{f}_j(\mathbf{r}', \omega') + \text{H.c.}, \quad (\text{B.2})$$

where  $\mathbf{G}_{ij}$  is the dyadic Green function of the Maxwell equations, satisfying  $\nabla \times \nabla \times \mathbf{G}_i - \epsilon(\mathbf{r}, \omega) \frac{\omega^2}{c^2} \mathbf{G}_i = \delta(\mathbf{r} - \mathbf{r}') \hat{e}_i$ . Physically it represents the field at point  $\mathbf{r}$  produced by a time-harmonic dipole at  $\mathbf{r}'$  oriented along direction  $i$ .  $\hat{\mathbf{f}}_j^{(\dagger)}(\mathbf{r}, \omega)$  annihilates (creates)

a lossy excitation of frequency  $\omega$ , at position  $\mathbf{r}$ , and in direction  $j$ . It satisfies bosonic commutation relations, namely:  $[\hat{f}_i(\mathbf{r}, \omega), \hat{f}_j^\dagger(\mathbf{r}', \omega')] = \delta_{ij}\delta(\omega - \omega')\delta(\mathbf{r} - \mathbf{r}')$ . When applying the Fermi Golden Rule, the initial state is  $|e, 0\rangle$ , while the final states are of the form  $|g, \mathbf{x}\omega k\rangle \equiv \hat{f}_k^\dagger(\mathbf{r}, \omega)|g, 0\rangle$  [106]. Using these final states in addition to the commutation relations, we get that

$$\Gamma = \frac{2\pi}{\hbar^2} \frac{e^2 \hbar}{\pi \epsilon_0 m_e^2 c^2} \int d\mathbf{x} \sum_k \frac{\omega_0^2}{c^2} \text{Im} \epsilon(\mathbf{x}) \left| \langle e | G_{ik} p_i(\mathbf{r}, \mathbf{x}, \omega_0) | g \rangle \right|^2.$$

Expanding the matrix element yields:

$$\Gamma = \frac{2\pi}{\hbar^2} \frac{e^2 \hbar}{\pi \epsilon_0 m_e^2 c^2} \int \int d\mathbf{r} d\mathbf{r}' \psi_e^*(\mathbf{r}) \psi_e(\mathbf{r}') (\text{Im} G_{ij}(\mathbf{r}, \mathbf{r}', \omega_0)) (p_i \psi_g(\mathbf{r})) (p_j^* \psi_g^*(\mathbf{r}')),$$

where we have used the identity:  $\frac{\omega_0^2}{c^2} \int d\mathbf{x} \text{Im} \epsilon(\mathbf{x}, \omega_0) (G(\mathbf{r}, \mathbf{x}, \omega_0) G^\dagger(\mathbf{r}', \mathbf{x}, \omega_0))_{ij} = \text{Im} G_{ij}(\mathbf{r}, \mathbf{r}', \omega_0)$  [109]. To proceed, we will substitute in the reflected part of the Green function for the system in Figure 1. An exact expression can be written in terms of the reflection and transmission coefficients of the interface between the conductor and air [113]. In the air region ( $z > 0$ ):

$$G_{ij}(\mathbf{r}, \mathbf{r}', \omega_0) = \frac{i}{2} \frac{1}{(2\pi)^2} \int d\mathbf{q} (C_{ij}^s + C_{ij}^p) e^{i\mathbf{q}\cdot\boldsymbol{\rho} + ik_\perp z} e^{-i\mathbf{q}\cdot\boldsymbol{\rho}' + ik_\perp z'}, \quad (\text{B.3})$$

where  $C^s$  and  $C^p$  are tensors describing the s- and p-polarized parts of the reflected fields. Choosing the atomic wavefunctions to be real (which can always be done) and defining  $M_i = \int d\mathbf{r} \psi_g e^{i\mathbf{q}\cdot\boldsymbol{\rho} + ik_\perp z} p_i \psi_e$ , and  $M_i^- = \int d\mathbf{r} \psi_g e^{-i\mathbf{q}\cdot\boldsymbol{\rho} + ik_\perp z} p_i^* \psi_e$ , we arrive at a generalized Fermi Golden Rule:

$$\Gamma = \frac{e^2}{\hbar \epsilon_0 m_e^2 c^2} \text{Re} \left[ \frac{1}{(2\pi)^2} \int d\mathbf{q} M_i (C_{ij}^s + C_{ij}^p) M_j^- \right]. \quad (\text{B.4})$$

The part of the decay rate coming from surface plasmons comes from the p-polarized waves, and accordingly, we will only work with that part of the reflected Green function. Performing a rotation:  $\{x, y, z\} \rightarrow \{q, q_\perp, z\}$ ,  $C_p$  can be expressed as

$$-c^2 \frac{r_p q}{\omega_0^2} \begin{pmatrix} \frac{k_\perp}{q} & 0 & 1 \\ 0 & 0 & 0 \\ -1 & 0 & -\frac{q}{k_\perp} \end{pmatrix} = -c^2 \frac{r_p q}{\omega_0^2} \begin{pmatrix} \frac{k_\perp}{q} \\ 0 \\ -1 \end{pmatrix} \otimes \begin{pmatrix} 1 & 0 & \frac{q}{k_\perp} \end{pmatrix} \equiv -2ic^2 \frac{r_p q}{\omega_0^2} \hat{\epsilon}_i(\mathbf{q}) \hat{\epsilon}_j(\mathbf{q})^*,$$

where the polarization vectors are defined by:  $\hat{\epsilon}(\mathbf{q}) \equiv \frac{\hat{\mathbf{q}} + i\hat{\mathbf{z}}}{\sqrt{2}}$ . We make our first approximation here: the electrostatic limit. Namely, that the main contribution to this integral comes from  $q \gg \frac{\omega}{c}$  (i.e., the confinement factor of the emitted plasmons is much larger than 1). This is an excellent approximation in all of our calculations. To lowest order in this approximation:  $k_\perp = iq$ , and  $M_i^- = M_i^*$ . Thus,

$$\Gamma = \frac{2e^2}{\hbar \epsilon_0 m_e^2 \omega_0^2} \text{Im} \left[ \frac{1}{(2\pi)^2} \int d\mathbf{q} q |\langle g | (\hat{\epsilon}(\mathbf{q}) \cdot \mathbf{p}) e^{i\mathbf{q} \cdot \boldsymbol{\rho} - qz} | e \rangle|^2 r_p \right].$$

The Fresnel reflection coefficient in the electrostatic limit is given by  $\frac{(\epsilon_r - 1)i - \frac{\sigma_R}{\omega_0 \epsilon_0}}{(\epsilon_r + 1)i - \frac{\sigma_R}{\omega_0 \epsilon_0}}$  [78]. Performing a non-dimensionalization on  $q$  with respect to  $q_0$ :  $q = q_0 u$ , where  $q_0 \equiv \frac{(\epsilon_r + 1)\epsilon_0 \omega_0}{\sigma_I(\omega_0)}$ , we arrive at a relatively simple final result:

$$\Gamma = \frac{4\alpha\omega_0}{m_e^2 c^2 (\epsilon_r + 1)} \eta_0^3 \int d\theta du u^2 e^{-2\eta_0 k z_0 u} |\langle g | (\hat{\epsilon}(\mathbf{q}) \cdot \mathbf{p}) e^{i\mathbf{q} \cdot \boldsymbol{\rho} - q(z-z_0)} | e \rangle|^2 \left( \frac{1}{\pi} \frac{\frac{\sigma_R u}{\sigma_I}}{(\frac{\sigma_R u}{\sigma_I})^2 + (1-u)^2} \right), \quad (\text{B.5})$$

where  $\eta_0$  is the resonant confinement factor of the plasmon  $\frac{\lambda_0}{\lambda_{pl}}$ ,  $\sigma_R(\sigma_I)$  are the real (imaginary) parts of the (local) conductivity at the resonant frequency, and  $\alpha = \frac{e^2}{4\pi\epsilon_0 \hbar c}$  is the fine-structure constant. In the lossless limit ( $\frac{\sigma_R}{\sigma_I} \rightarrow 0$ ), the lineshape in parentheses becomes  $\delta(u - 1)$ . The decay rate in the lossless limit can be understood as the decay rate into surface plasmons (SPs).

Note that in the lossless limit, we arrive at the same expression for the decay

rate as would be obtained had we written  $\mathbf{A}$  based on a canonical quantization scheme. Namely:  $\mathbf{A} = \sum_n \sqrt{\frac{\hbar}{2\epsilon_0\omega_n}} (\mathbf{F}_n a_n + \mathbf{F}_n^* a_n^\dagger)$ , where the  $\mathbf{F}_n$  are the orthonormal modes of the Maxwell equations. In this case, the modes  $\mathbf{F}(\mathbf{q})$  are given by:  $\sqrt{\frac{2\kappa}{1+\epsilon_r}} e^{i\mathbf{q}\cdot\rho - \kappa z} \left( \frac{\kappa\hat{\mathbf{q}} + iq\hat{\mathbf{z}}}{\sqrt{\kappa^2 + q^2}} \right)$ . In the electrostatic limit,  $\kappa \approx q$ , reproducing the results that we arrive at using the Green function formalism.

## B.3 First Order Processes

In this section, we consider processes that can be described at first-order in perturbation theory: direct emission into a single lossy excitation of the macroscopic electromagnetic field. In particular, we examine electric and magnetic multipolar transitions. We provide a detailed discussion of how losses modify the decay rates computed from canonical quantization based on modal expansion and show the regimes in which non-radiative or radiative decay dominates. By radiative decay, we do not mean decay into far-field photons, but rather into propagating plasmons. This is in contrast to the non-radiative decay into the other lossy channels of the 2D conductor, which, for example, is the mechanism responsible for the strong decay rate enhancement of emitters adsorbed onto a conducting surface.

### B.3.1 Electric Multipole Transitions

The calculations below are presented for the case for which the initial and final wavefunctions have their z-projected angular momentum to be zero (i.e;  $m_i = m_f = 0$ ). In this case, the angular integral is simply  $2\pi$ , and we can pick  $\mathbf{q}$  to be in a particular direction, called  $x$ . Frequently, it is the case that in the matrix element in Equation (S5) there is one main contributing term from the series expansion of the exponential.

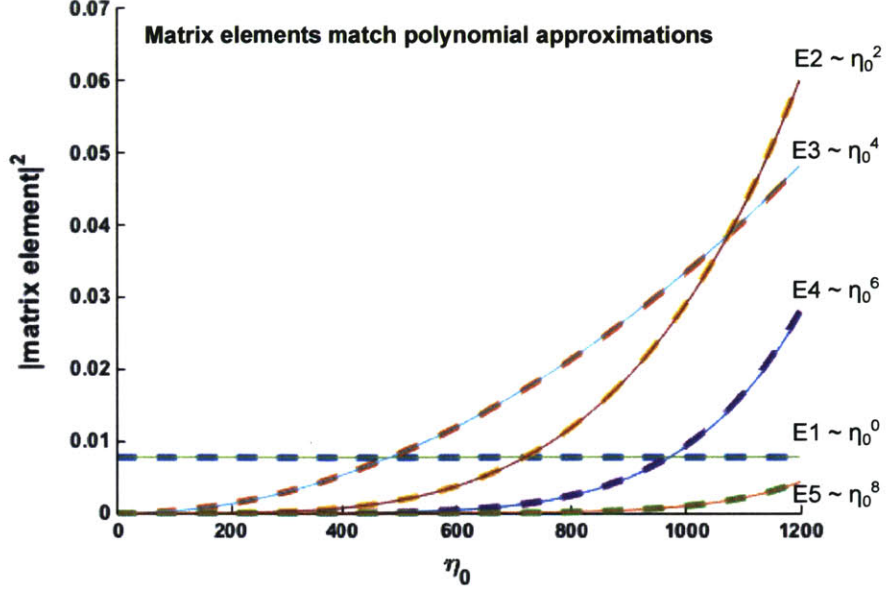


Figure B-1: Comparison of matrix elements computed exactly (solid) with polynomial approximations (dashed) for different transitions in the Hydrogen  $5 \leftrightarrow 6$  transition series as a function of  $\eta_0$  for  $\lambda_0 = 7.45\mu\text{m}$ . These curves overlap completely in this range.

That is to say:

$$\left| \langle e | e^{\eta_0 k(-ix - (z-z_0))} \hat{e}_\theta^* \cdot \nabla | g \rangle \right|^2 = C \ell \eta_0^{2(n-1)} u^{2(n-1)} \quad (\text{B.6})$$

where  $n = 1$  for dipole (E1) transitions,  $n = 2$  for quadrupole (E2) transitions, and so on. In Figure S1, we demonstrate the validity of (6), where we plot exact matrix elements involving the full exponential (solid lines) and their respective polynomial approximations (dashed lines) for E1-E5 transitions in the Hydrogen  $6\{p, d, f, g, h\} \rightarrow 5s$  transition series as a function of confinement  $\eta_0$ . The wavelength of the transition is  $7.45 \mu\text{m}$ . This transition series is different than that considered in the main text ( $4s \leftrightarrow 6\{p, d, f, g, h\}$ ). We choose a different transition series in the SI in order to give the reader a more complete picture of how confinement, separation, vacuum wavelength, and losses affect the decay rates of excited emitters.

When the approximation in Equation (S6) is satisfied, the radiative rate of emission (into surface plasmons) scales with  $\eta_0$  as:

$$\Gamma_r^{En} = \eta_0^{3+2(n-1)} \times \frac{4\pi\alpha\omega_0}{(m_e c)^2(\epsilon_r + 1)} e^{-2\eta_0 k z_0} C_n. \quad (\text{B.7})$$

and the ratio of total decay rate to decay rate into SPs is:

$$\frac{\Gamma_{TOT}^{En}}{\Gamma_R^{En}} = \int du u^{2+2(n-1)} e^{-2\eta_0 k z_0 (u-1)} \left( \frac{1}{\pi} \frac{\frac{\sigma_R u}{\sigma_I}}{(\frac{\sigma_R u}{\sigma_I})^2 + (1-u)^2} \right) \quad (\text{B.8})$$

To gain insight into the typical values of decay rates given by Equations (S7) and (S8), it is useful to write the momentum matrix element in units of  $\frac{\hbar}{a_0}$ , where  $a_0$  is some characteristic size of the emitter. When considering atomic systems, it is reasonable to take  $a_0$  to be the Bohr radius, in which case  $C_l$  is dimensionless and the resulting factor  $\left(\frac{\hbar}{m_e c a_0}\right)^2$  is identified as  $\alpha^2$ . Our formulas summarized at the end of the SI reflect this choice of units.

### Effect of Losses

In Figure S2, we plot this ratio for five Hydrogen atom transitions:  $5s \leftrightarrow 6\{p, d, f, g, h\}$ . For each transition, we plot the ratio as a function of on-resonance confinement factor  $\eta_0$  at atom-surface separations of 5 nm, 10 nm, and 15 nm. Note that only the dipole case is not plotted on a logarithmic scale - indicating that losses only weakly modify decay rates of dipole emitters, even for  $\eta_0$  as low as 20. At very low plasmon confinement, the emission into lossy channels dominates the emission into plasmons. As can be seen in Figure S2, emission into lossy channels far exceeds emission into SPs for higher-order angular momentum transitions. For a Hydrogen atom 5 nm above the a surface undergoing an E5 transition ( $6h \rightarrow 5s$ ), the lossy channel emission can exceed the SP emission by nearly 12 orders of magnitude at  $\eta_0 = 20$ , leading to a total Purcell factor of roughly  $10^{26}$ . This leads to a total decay lifetime of roughly 10

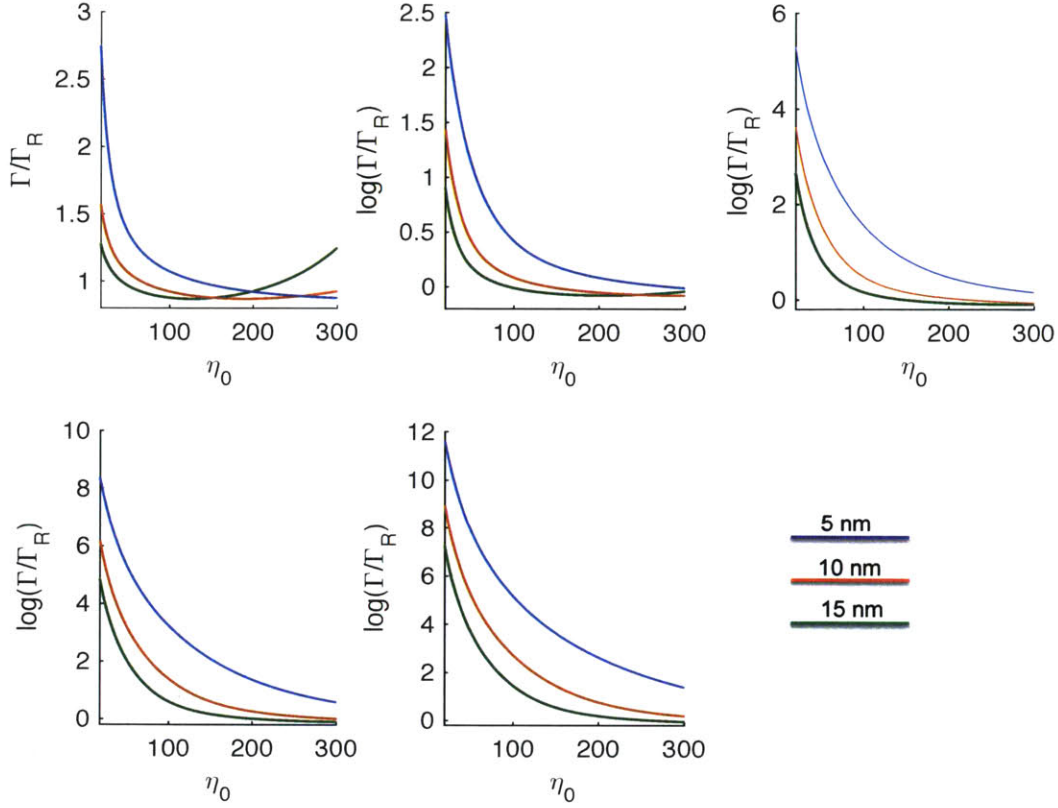


Figure B-2: **Ratio of total decay rate to decay rate into plasmons - Multipolarity and Confinement Dependence:** plotted as a function of on-resonance confinement factor  $\eta_0$  at different atom-surface separations for E(1-5) transitions in the Hydrogen  $6\leftrightarrow 5$  transition series. The minimum confinement factor considered in this figure is 20.

ns, which is typical of many dipole emitters in free space.

At higher values of confinement ( $\eta_0 > 150$ ) and atom-surface separation ( $z_0 > 10$  nm), the SP and lossy channel decay rates are within the same order of magnitude. While the non-radiative enhancement decreases precipitously at these confinements and separations, the more rapidly increasing enhancement of emission into propagating SPs ensures that the total decay rate is increasing as a function of  $\eta_0$ . To give the reader further intuition for the phenomena discussed in this section, we present in Figure S3 the integrand of Equation (S8) for different values of confinement and atom-surface separation. We place a high-wavevector cutoff in the integrand at 5 nm



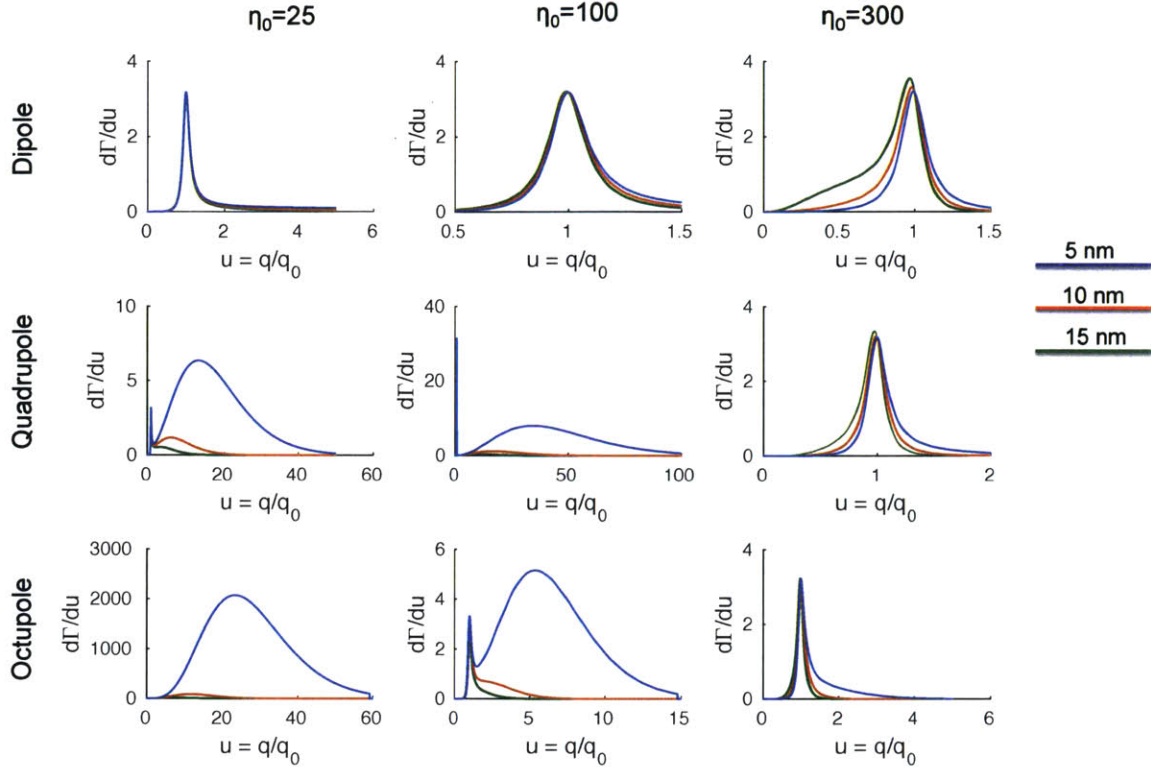


Figure B-3: **Effect of Confinement and Multipolarity on Radiative and Non-Radiative Decay Rates:** Integrand of Eq. (14) plotted for dipole (top), quadrupole (middle), and octupole (bottom) transitions at three different on-resonance confinements ( $\eta_0 = \{25, 100, 300\}$ ) and atom-surface separations ( $z_0 = \{5 \text{ nm}, 10 \text{ nm}, 15 \text{ nm}\}$ ).

due to the fact that the use of macroscopic electrodynamics becomes questionable at these distances. The choice of 5 nm is somewhat arbitrary, but we choose it because averaging microscopic fields over a  $5 \text{ nm} \times 5 \text{ nm}$  area corresponds to averaging over several hundred unit cells. 5 nm is a somewhat conservative cutoff, and yet it doesn't affect the integrand in Figure S3 significantly.

From Figure S3, it is clear that for higher multipole transitions, the integrand peaks at values of  $u$  far greater than  $u = 1$ , which is the value associated with the surface plasmon pole [78]. When this happens, we can approximate the lineshape

function in the integrand of Equation (S8) by  $\frac{1}{\pi Q u}$ . The decay rate (which is in this limit purely nonradiative) is therefore

$$\Gamma_{nr}^{En} = \eta_0 \times \frac{4(2n-1)! \alpha \omega_0}{(m_e c)^2 (\epsilon_r + 1) Q} (2kz_0)^{-(2+2(n-1))} C_n. \quad (\text{B.9})$$

We can thus see that the decay rate is a purely increasing function of  $\eta_0$ . In fact, once non-radiative decay becomes unimportant, the decay rate transitions from increasing with  $\eta_0$  to increasing as  $\eta_0^{3+2(n-1)}$ . We conclude therefore that higher confinement is always beneficial to achieving increasing decay rates.

We conclude this section by noting that for the parameters that we investigated, emission into SPs tends to be the dominant contribution to the decay rate for dipole transitions. Thus, for investigations into two-plasmon spontaneous emission mediated by dipole transitions and singlet-triplet transitions, one is justified in using ossless QED based on mode expansion.

### B.3.2 Spin Flip Magnetic Multipole Transitions

In this section, we derive the rate at which an excited state flips its spin due to vacuum fluctuations in the magnetic field. We look at both radiative and non-radiative decays into 2D plasmons as a function of their confinement factor. The part of the Hamiltonian governing this behavior is  $\frac{e\hbar}{2m_e} \boldsymbol{\sigma} \cdot \mathbf{B}$  [79]. The magnetic field operator is given by

$$\begin{aligned} B_i(\mathbf{r}) &= (\nabla \times \mathbf{A})_i \\ &= \sqrt{\frac{\hbar}{\pi \epsilon_0}} \int d\omega' \frac{\omega'}{c^2} \int d\mathbf{r}' \sqrt{\text{Im } \epsilon(\mathbf{r}', \omega')} \epsilon_{ilm} \partial_l G_{mj}(\mathbf{r}, \mathbf{r}'; \omega') \hat{f}_j(\mathbf{r}', \omega') + \text{H.c.}, \end{aligned} \quad (\text{B.10})$$

where  $\epsilon_{ilm}$  is the Levi-Civita symbol, and  $\partial_l$  is a shorthand for  $\frac{\partial}{\partial x_l}$ . Applying the Fermi Golden Rule in a manner similar to that in Section II, the decay rate is given by:

$$\Gamma = \frac{2\pi}{\hbar^2} \frac{e^2 \hbar^3}{4\pi\epsilon_0 m_e^2 c^2} \sigma_i^{eg} \sigma_r^{*eg} \int \int d\mathbf{r} d\mathbf{r}' \psi_g^*(\mathbf{r}) \psi_g(\mathbf{r}) [\text{Im} \epsilon_{ilm} \epsilon_{rst} \partial_l \partial'_s G_{mt}(\mathbf{r}, \mathbf{r}', \omega_0)] \psi_e(\mathbf{r}) \psi_e^*(\mathbf{r}'),$$

where  $\sigma_k^{eg}$  denotes the k-th component of the overlap of the spin part of the excited and ground states, and  $\partial'$  denotes partial derivatives with respect to  $\mathbf{r}'$ . Simplifying further, the decay rate is given by:

$$\Gamma = -\frac{e^2 \hbar}{4\epsilon_0 m_e^2 c^2} \text{Re} \left[ \frac{1}{(2\pi)^2} \int d\mathbf{q} M_i M_r^- \epsilon_{ilm} \epsilon_{rst} k_i k_s^- (C_{mt}^s + C_{mt}^p) \right],$$

where:  $k = (\mathbf{q}, k_\perp)$ ,  $k^- = (-\mathbf{q}, k_\perp)$  and  $\mathbf{M} = \sigma^{eg} \int d\mathbf{r} \psi_g e^{i\mathbf{q}\cdot\rho + ik_\perp z} \psi_e$  and  $\mathbf{M}^- = \sigma^{eg*} \int d\mathbf{r} \psi_g e^{-i\mathbf{q}\cdot\rho + ik_\perp z} \psi_e$ . Once again, we consider only the p-polarized contribution in the electrostatic limit. This further simplifies to

$$\Gamma = \frac{\alpha\omega_0}{2(\epsilon_r + 1)} \left( \frac{\hbar\omega_0}{m_e c^2} \right)^2 \eta_0 \int d\theta du e^{-2\eta_0 k z_0 u} \times |\langle g | \sigma_\perp e^{-i\mathbf{q}\cdot\rho - q(z-z_0)} | e \rangle|^2 \left( \frac{1}{\pi} \frac{\frac{\sigma_R u}{\sigma_I}}{(\frac{\sigma_R u}{\sigma_I})^2 + (1-u)^2} \right), \quad (\text{B.11})$$

For a transition with a change in orbital angular momentum of  $(n-1)$  (an Mn transition), the matrix elements in Equation (S21) can be expressed as  $C_n \eta_0^{2(n-1)} u^{2(n-1)}$ . When the change in the z-projected orbital angular momentum is zero, the radiative and non-radiative decay rates are respectively:

$$\Gamma_r^{Mn} = \eta_0^{1+2(n-1)} \times \frac{\pi\alpha\omega_0}{(\epsilon_r + 1)} \left( \frac{\hbar\omega_0}{m_e c^2} \right)^2 e^{-2\eta_0 k z_0} C_n \quad (\text{B.12})$$

and

$$\Gamma_{nr}^M = \eta_0 \frac{(2n-3)! \alpha\omega_0}{Q(\epsilon_r + 1)} \left( \frac{\hbar\omega_0}{m_e c^2} \right)^2 (2kz_0)^{-2(n-1)} C_n \quad (\text{B.13})$$

Note that Equation (S13) does not hold for  $n = 1$  (magnetic dipole transition). In this case, the formula for the rate is more complicated, and we do not derive it here.

## B.4 Second Order Processes - Intercombination Transitions and Two Plasmon Emission

### B.4.1 Electric Dipole (Intercombination) Mechanism

The rate of the singlet-triplet transition is generally limited by the weakness of the spin-orbit interaction. However, in atoms and molecules near 2D conductors, the rate of the singlet-triplet transition can be greatly enhanced due to the strong enhancement of electric-dipole transitions. For instructional purposes, we consider here a situation in which the ground state is a singlet with no nearly degenerate triplet states, and the excited state is a triplet state, which has nearly degenerate singlet states nearby. In this case, the transition rate from an triplet state  $|T_1, 0\rangle$  to a singlet state  $|S_0, \mathbf{q}\rangle$  under the influence of a perturbation  $H_{SO} + (\mathbf{d}_1 \cdot \mathbf{E}_1 + \mathbf{d}_2 \cdot \mathbf{E}_2)$  is given by

$$\Gamma = \frac{2\pi}{\hbar^2} \sum_{\mathbf{q}} \left| \sum_n \frac{\langle S_0, \mathbf{q} | (\mathbf{d}_1 \cdot \mathbf{E}_1(\mathbf{r}_1) + \mathbf{d}_2 \cdot \mathbf{E}_2(\mathbf{r}_2)) | S_n, 0 \rangle \langle S_n, 0 | H_{SO} | T_1, 0 \rangle}{E_{T_1} - E_{S_n}} \right|^2 \delta(\omega(\mathbf{q}) - \omega_0) \quad (\text{B.14})$$

Taking the approximation of one main contributing intermediate singlet state,  $|S'\rangle$ , the spin-orbit and electromagnetic effects separate as follows:

$$\Gamma = \frac{2\pi}{\hbar^2} \sum_{\mathbf{q}} |\langle S_0, \mathbf{q} | (\mathbf{d}_1 \cdot \mathbf{E}_1(\mathbf{r}_1) + \mathbf{d}_2 \cdot \mathbf{E}_2(\mathbf{r}_2)) | S', 0 \rangle|^2 \left| \frac{\langle S_n, 0 | H_{SO} | T_1, 0 \rangle}{E_{T_1} - E_{S'}} \right|^2 \delta(\omega(\mathbf{q}) - \omega_0).$$

In Helium-like atoms (and many other atoms and molecules), the spatial parts of singlet and triplet states are well-described by (resp.) antisymmetrized or symmetrized combinations of two single-particle states. Taking two single-particle states  $|\alpha\rangle$  and  $|\beta\rangle$ , we can write spatial wavefunctions such as:  $|\alpha\rangle|\beta\rangle + |\beta\rangle|\alpha\rangle$  and  $|\alpha\rangle|\gamma\rangle + |\gamma\rangle|\alpha\rangle$

to describe spin-singlets  $|S_0\rangle$  and  $|S'\rangle$  (As an example, take  $\alpha = 2S$  and  $\beta = 2S$ ,  $\gamma = 2P$ . This example corresponds to a two states in the Helium atom separated by a wavelength of  $2.06 \mu m$  [63]). When considering the Purcell enhancement associated with placing an excited spin-triplet or spin-singlet near plasmons, the same spin-orbit coupling factor shows up as that which shows up in the free-space decay rate. Therefore, the spin-orbit coupling does not show up in the Purcell factor, which we show is given by:

$$F_p^{S \rightarrow T} = \eta_0^3 \times \frac{3\pi f}{(\epsilon_r + 1)} e^{-2\eta_0 k z_0} \times \int du u^2 e^{-2\eta_0 k z_0 (u-1)} \left( \frac{1}{\pi \left( \frac{\sigma_R u}{\sigma_I} \right)^2 + (1-u)^2} \right), \quad (\text{B.15})$$

where  $f = \frac{1}{2}$  if the dipole is oriented parallel to the surface of the conductor, and  $f = 1$  if the dipole is oriented perpendicular to the surface. In the lossless limit, the integral over  $u$  is one, giving a result in agreement with the well-known  $\eta_0^3$  decay law for dipolar emitters [77, 78].

## B.4.2 Two Plasmon Spontaneous Emission

Finally, we consider situations in which an emitter above a 2D conductor can emit two lossy excitations of the electromagnetic field, a process that is second-order in the perturbation theory. We consider an initial state  $|e, 0\rangle$  and a final state  $|g, \mathbf{r}\omega k, \mathbf{r}'\omega' k\rangle \equiv \hat{f}_k^\dagger(\mathbf{r}, \omega) \hat{f}_{k'}^\dagger(\mathbf{r}', \omega') |g, 0\rangle$ . The atom is coupled to the field through a perturbation,  $V$ . Fermi's Golden Rule for this decay reads:

$$\Gamma = \frac{2\pi}{\hbar^2} \frac{1}{2} \int d\mathbf{r} d\mathbf{r}' \int d\omega d\omega' \sum_{k, k'} \left| \sum_{i_1} \frac{\langle g, \mathbf{r}\omega k, \mathbf{r}'\omega' k | V | i_1 \rangle \langle i_1 | V | e, 0 \rangle}{E_i - E_{i_1} + i0^+} \right|^2 \delta(\omega_0 - \omega - \omega'), \quad (\text{B.16})$$

where  $|i_1\rangle$  are intermediate states containing both the atom and field degrees of freedom. The sum is understood to be a sum over discrete degrees of freedom and an integral over continuous ones. The factor of  $1/2$  comes from the fact that when we

sum over all  $\{\mathbf{r}\omega k, \mathbf{r}'\omega'k\}$  pairs, each pair of excitations appears twice.

For simplicity, we work in the dipole approximation, in which  $V = -\mathbf{d} \cdot \mathbf{E}(\mathbf{r}_0)$ , where  $\mathbf{r}_0$  is the atom position which we define as  $(0, 0, z_0)$ , using the coordinate system in Figure 1. The electric-field operator is:

$$\mathbf{E}(\mathbf{r}_0) = i\sqrt{\frac{\hbar}{\pi\epsilon_0}} \int d\omega \frac{\omega^2}{c^2} \int d\mathbf{r}' \sqrt{\text{Im } \epsilon(\mathbf{r}')} \mathbf{G}(\mathbf{r}_0, \mathbf{r}'; \omega) \cdot \hat{\mathbf{f}}(\mathbf{r}', \omega) + \text{H.c.} \quad (\text{B.17})$$

Using the above electric-field operator and the dipole interaction Hamiltonian, the decay rate into two lossy excitations is given by the general formula:

$$\frac{32\pi\alpha^2}{c^2} \int_0^{\omega_0} d\omega \omega^2 (\omega_0 - \omega)^2 \text{Im } G_{ri}(\mathbf{r}_0, \mathbf{r}_0, \omega) \text{Im } G_{sj}(\mathbf{r}_0, \mathbf{r}_0, \omega_0 - \omega) \times \sum_{m,n} \left( \frac{x_j^{gn} x_i^{ne}}{\omega_e - \omega_n - \omega} + \frac{x_i^{gn} x_j^{ne}}{\omega_e - \omega_n - (\omega_0 - \omega)} \right) \left( \frac{x_s^{gm} x_r^{me}}{\omega_e - \omega_m - \omega} + \frac{x_r^{gm} x_s^{me}}{\omega_e - \omega_m - (\omega_0 - \omega)} \right)^*, \quad (\text{B.18})$$

where  $x_i^{ab} \equiv \langle a | \hat{\epsilon}_i \cdot \mathbf{r} | b \rangle$ .

As discussed in Section II,  $\text{Im } G_{ij}$  can be expressed in terms of the imaginary part of the reflectivity  $\text{Im } r_p$  and polarization vectors,  $\hat{\epsilon}(\theta) = \frac{\hat{\mathbf{q}} + i\hat{\mathbf{z}}}{\sqrt{2}}$ , where  $\theta$  is the angle between  $\hat{\mathbf{q}}$  and the x-axis of  $q$ -space. Also as discussed in Sec. II, the imaginary part of the reflectivity can be expressed as  $\text{Im } r_p(u, \omega) = \frac{2\pi}{\epsilon_r + 1} \left( \frac{1}{\pi} \frac{u/Q(\omega)}{(1-u)^2 + (u/Q(\omega))^2} \right)$ , where  $u = q/q_0$ , with  $q_0(\omega) = \frac{(\epsilon_r + 1)\omega\epsilon_0}{\text{Im } \sigma(\omega)}$ , just as in Sec. II. The lossless limit of the two-excitation spontaneous emission rate per unit frequency (also known as the differential decay rate) is found to be:

$$\frac{d\Gamma}{dy} = \frac{16\pi\omega_0\alpha^2 k^4}{(\epsilon_r + 1)^2} \times [y(1-y)\eta(y)\eta(1-y)]^3 e^{-2kz_0[y\eta(y) + (1-y)\eta(1-y)]} \times \left\langle \left| \sum_n \frac{(\mathbf{r}^{gn} \cdot \hat{\epsilon}(\theta))(\mathbf{r}^{ne} \cdot \hat{\epsilon}(\theta'))}{y_e - y_n - y} + \frac{(\mathbf{r}^{gn} \cdot \hat{\epsilon}(\theta))(\mathbf{r}^{ne} \cdot \hat{\epsilon}(\theta'))}{y_e - y_n - (1-y)} \right|^2 \right\rangle_{\theta, \theta'}, \quad (\text{B.19})$$

where  $k = \frac{\omega_0}{c}$  and  $\Gamma \equiv \int_0^1 dy \frac{d\Gamma}{dy}$ . In writing the previous equation, we have performed the non-dimensionalizations:  $\eta(y) = \frac{\omega(y)}{\omega_0}$ , and  $y = \frac{\omega}{\omega_0}$ .<sup>1 2</sup> A relatively simple case of this expression occurs when the initial and final states are  $s$  states. The intermediate states are then of the form  $|i_1\rangle = |np_j\rangle$  for  $j = x, y, z$ . In the electrostatic limit,  $\hat{\epsilon}(\theta) = \frac{\cos(\theta)\hat{x} + \sin(\theta)\hat{y} + i\hat{z}}{\sqrt{2}}$ . The angular average is  $3/8$  and the differential decay rate can be expressed in terms of matrix elements of  $z$ ,  $z_{gn} \equiv \langle g|z|n\rangle$ , as:

$$\frac{6\pi\omega_0\alpha^2k^4}{(\epsilon_r + 1)^2} \times [y(1-y)\eta(y)\eta(1-y)]^3 e^{-2k\frac{z_0}{c}[y\eta(y)+(1-y)\eta(1-y)]} \times \left| \sum_n z_{gn}z_{ne} \left( \frac{1}{y_i - y_n + y - 1} + \frac{1}{y_i - y_n - y} \right) \right|^2.$$

The two-photon differential emission rate in free-space, by comparison is [114]

$$\frac{4}{3\pi}\alpha^2k^4y^3(1-y)^3 \left| \sum_n z_{gn}z_{ne} \left( \frac{1}{y_i - y_n + y - 1} + \frac{1}{y_i - y_n - y} \right) \right|^2.$$

Therefore, the enhancement factor per unit frequency in free-space is

$$\frac{d\Gamma/dy|_{pl}}{d\Gamma/dy|_{fs}} = \frac{9\pi^2}{2(\epsilon_r + 1)^2} \eta^3(y)\eta^3(1-y) e^{-2\frac{z_0}{c}[y\eta(y)+(1-y)\eta(1-y)]}. \quad (\text{B.20})$$

Equation (S20) can be re-expressed in terms of the Purcell factor,  $F_p(\omega)$ , for the single plasmon emission of a dipole polarized perpendicular to the 2D conductor as

$$\frac{d\Gamma/dy|_{pl}}{d\Gamma/dy|_{fs}} = \frac{1}{2} F_p(y) F_p(1-y). \quad (\text{B.21})$$

<sup>1</sup>Although the angular integrals could have already been performed, we express our answer in terms of polarization vectors to make the result resemble that which would be obtained through mode expansion over the lossless field operator presented at the end of Section 3.A.

<sup>2</sup>Another useful non-dimensionalization for atomic systems, that allows for quick estimation of the decay rate is  $\mathbf{r} \equiv a_0\mathbf{x}$ .

## Effect of Dispersion on Lossless Rates

In the main text, we use the Drude dispersion in order to evaluate the two-plasmon spontaneous emission rate. In the Drude model, the dispersion relation implies that  $\eta(y) = \frac{\omega c}{\beta^2} = \frac{\omega_0 c}{\beta^2} y$ , where  $\beta$  is a constant determined by the plasma frequency and thickness of the metal. We define the characteristic squeezing  $\eta_0 = \frac{\omega_0 c}{2\beta^2}$ . The factor of 2 in the definition of  $\eta_0$  is natural because most of the emission comes from frequencies near  $\omega = \frac{\omega_0}{2}$ . It thus follows that the differential decay rate is:

$$\left. \frac{d\Gamma}{dy} \right|_{\text{Drude}} = 384 \frac{\pi\omega_0}{(\epsilon_r + 1)^2} \alpha^2 k^4 \eta_0^6 \times y^6 (1-y)^6 \left| \sum_n z_{gn} z_{ne} \left( \frac{1}{y_i - y_n + y - 1} + \frac{1}{y_i - y_n - y} \right) \right|^2 \quad (\text{B.22})$$

In many cases, the 2D plasmon dispersion appears to be linear with wavevector, i.e;  $\eta(y) = \eta_0$ , where  $\eta_0$  is some constant squeezing that can be as high as 360 (in Beryllium for example). Values of 240 have been observed in undoped graphene [50, 51, 52]. Therefore, the differential decay rate is

$$\left. \frac{d\Gamma}{dy} \right|_{\text{const } \eta} = \frac{6\pi\omega_0}{(\epsilon_r + 1)^2} \alpha^2 k^4 \eta_0^6 \times y^3 (1-y)^3 \left| \sum_n z_{gn} z_{ne} \left( \frac{1}{y_i - y_n + y - 1} + \frac{1}{y_i - y_n - y} \right) \right|^2 \quad (\text{B.23})$$

## The Effect of Losses on Two Plasmon Spontaneous Emission

In this section, we estimate the effect of losses on the two-excitation spontaneous emission rate and show that the total decay rates computed in the main text (i.e., without losses) are not significantly altered by losses. To compute emission of two excitations in the presence of dissipation, the starting point is Equation (S18). The decay rate can be expressed as

$$\frac{6\pi\alpha^2 c^2}{(\epsilon_r + 1)^2} \int_0^{\omega_0} d\omega \omega^2 (\omega_0 - \omega)^2 I(\omega) I(\omega_0 - \omega) \left| \sum_n z_{gn} z_{ne} \left( \frac{1}{y_i - y_n + y - 1} + \frac{1}{y_i - y_n - y} \right) \right|^2, \quad (\text{B.24})$$



in which  $I(\omega)$  is a shorthand for

$$q_0^3(\omega)e^{-2q_0(\omega)z_0} \int du u^2 e^{-2q_0(\omega)z_0(u-1)} \left( \frac{1}{\pi} \frac{u/Q(\omega)}{(1-u)^2 + (u/Q(\omega))^2} \right) \equiv q_0^3(\omega)e^{-2q_0(\omega)z_0} I(u, \omega). \quad (\text{B.25})$$

In the lossless limit, the integral evaluates to 1, reproducing the results of Sec. IV.B. as expected. It can thus be seen that the ratio of the total differential decay rate to the lossless differential decay rate is

$$\frac{d\Gamma_{TOT}/dy}{d\Gamma_r/dy} = \left[ \int du u^2 e^{-2q_0(y)z_0(u-1)} \left( \frac{1}{\pi} \frac{u/Q(y)}{(1-u)^2 + (u/Q(y))^2} \right) \right] \times \left[ \int du u^2 e^{-2q_0(1-y)z_0(u-1)} \left( \frac{1}{\pi} \frac{u/Q(1-y)}{(1-u)^2 + (u/Q(1-y))^2} \right) \right] \quad (\text{B.26})$$

In Fig. S4, we compare the differential decay rates with losses to those without losses for atom-surface separations of 0.5, 1, 5, and 10 nm. The transition under consideration is the  $4s \rightarrow 3s$  transition in Hydrogen, just as in the main text. The model assumed to hold through the entire decay spectrum is the Drude model, in which  $Q(\omega) = \omega\tau \implies Q(y) = (\omega_0\tau)y$ , where  $\tau$  is the frequency-independent relaxation time. Although a slightly more realistic model for the conductivity can be adopted, we choose the Drude model for instructional purposes. In the simulations resulting in Fig. S4, we chose the confinement factor at  $y = 0.5$  to be 150, just as in the main text. We also chose the quality factor at  $y = 0.5$  to be 20. We can see that for distances between 5 and 15 nm, the decay is mostly through plasmons. However, for distances below 1 nm, we can see two phenomena. The first being that the dominant mode of decay is through the loss mechanisms that determine the relaxation time. The second is that the peak of the emission is no longer at  $y = 0.5$ . From these last two observations, we arrive at two conclusions. The first is that at short atom-surface separations, entangled lossy excitations (such as particle-hole excitations or phonons) can be produced at high rates. The second is that the spectral shape of an emitter

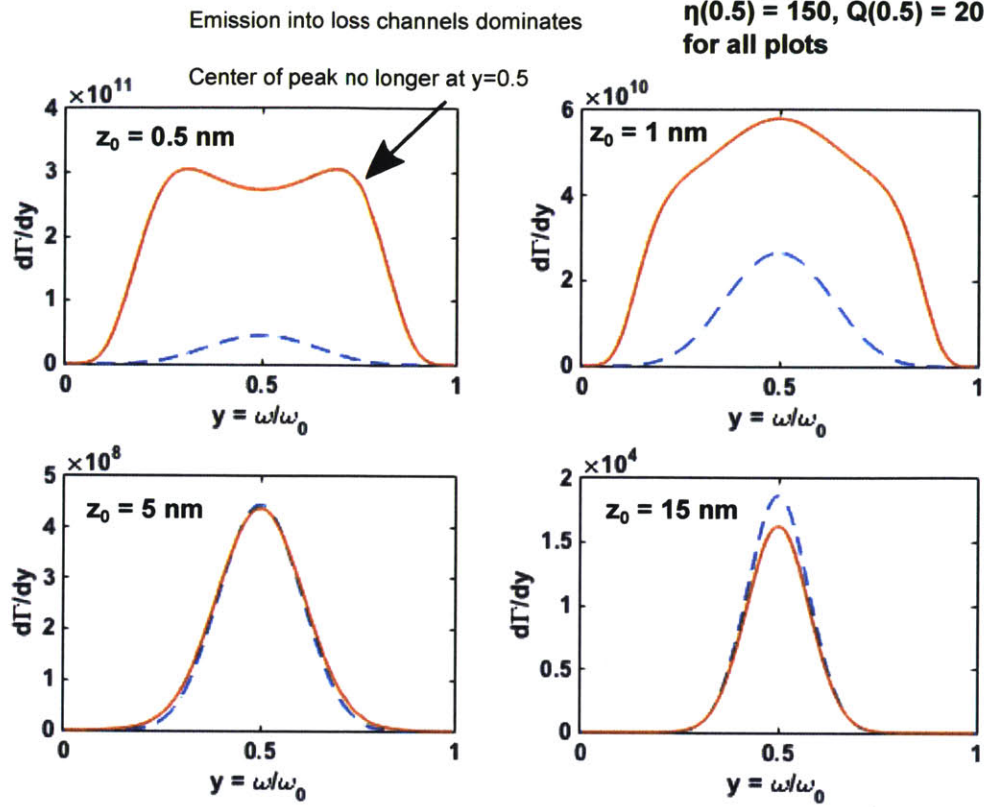


Figure B-4: **Effect of Losses on Two Plasmon Spontaneous Emission:** Differential decay rate  $d\Gamma/dy$  plotted as a function of  $y$  for lossless (dashed blue) and lossy (solid orange) 2D conductors. A Drude model to describe Graphene is assumed. The lossless version of these differential decay plots are plotted for the same transition as Fig. 4b in the main text.

can be significantly altered by the presence of losses.

To conclude our discussion of losses and two-plasmon emission, we present analytical (up to atomic matrix elements) expressions for the differential decay rate when non-radiative decay is a dominant effect. What can be computed exactly and analytically is the ratio of this differential decay rate to the free-space differential decay rate. At short distances, or long wavelengths, i.e;  $q(\omega_0)z_0 \ll 1$  and  $Q \gg 1$  (in practice,  $Q = 3$  is already high enough), each of the integrals in Equation (S24) becomes

$$\frac{1}{\pi Q(\omega)} e^{2q_0(\omega)} (2q_0(\omega)z_0)^{-2},$$

where  $\omega = \omega_0 y$  or  $\omega_0(1 - y)$ . When this happens, the differential decay rate becomes:

$$\frac{d\Gamma}{dy} \Big|_{\text{Lossy}} = \frac{\omega_0 \alpha^2}{4\pi(\epsilon_r + 1)^2} \frac{1}{z_0^4} \times \left[ \frac{y(1-y)\eta(y)\eta(1-y)}{Q(y)Q(1-y)} \right] \times \left| \sum_n z_{gn} z_{ne} \left( \frac{1}{y_i - y_n + y - 1} + \frac{1}{y_i - y_n - y} \right) \right|^2. \quad (\text{B.27})$$

When  $Q \ll 1$ , one of the two integrals in Equation (S24) becomes linear in  $Q$ . The enhancement of the differential decay rate is given by the previous equation divided by the free-space differential emission rate and is independent of atomic parameters. The analysis of Sec. IV. B. can be generalized to arbitrary dispersion relations such as Drude or linear.

Finally, a word of caution about the use of these estimates: when  $z_0$  approaches the emitter size, the dimensionless decay rate approaches 1, indicating the breakdown of perturbative quantum electrodynamics. Therefore, these formulas should not be used in those short-distance cases, but rather should be used to estimate the distance at which perturbation theory breaks down.

## B.5 Summary of Results

In this section, we summarize our results for the various decay rates in purely radiative and purely non-radiative limits.

For electric (En) transitions, the radiative decay rate is:

$$\Gamma_r^{En} = \eta_0^{3+2(n-1)} \times \frac{4\pi\alpha^3\omega_0}{(\epsilon_r + 1)} e^{-2\eta_0 k z_0} C_n.$$

The corresponding non-radiative decay rate is:

$$\Gamma_{nr}^{En} = \eta_0 \times \frac{4(2n-1)!\alpha^3\omega_0}{(\epsilon_r + 1)Q} (2kz_0)^{-(2+2(n-1))} C_n.$$

For spin flip transitions, the radiative decay rate is:

$$\Gamma_r^{Mn} = \eta_0^{1+2(n-1)} \times \frac{\pi\alpha\omega_0}{(\epsilon_r + 1)} \left( \frac{\hbar\omega_0}{m_e c^2} \right)^2 e^{-2\eta_0 k z_0} C_n.$$

The corresponding non-radiative decay rate is (for  $n \neq 1$ ):

$$\Gamma_{nr}^{Mn} = \eta_0 \times (2n - 3)! \frac{\alpha\omega_0}{Q(\epsilon_r + 1)} \left( \frac{\hbar\omega_0}{m_e c^2} \right)^2 (2kz_0)^{-2(n-1)} C_n.$$

For intercombination transitions in the single-contributing intermediate state approximation, the Purcell factor in the lossless limit is

$$F_p^{S \leftrightarrow T} = \frac{3\pi f}{\epsilon_r + 1} \eta_0^3 e^{-2\eta_0 k z_0}$$

For two-plasmon spontaneous emission, the second order differential purcell-factor within the dipole approximation is:

$$\frac{d\Gamma/dy|_{pl}}{d\Gamma/dy|_{fs}} = \eta_0^6 \times 72\pi^2 (e^{-\frac{8\pi\eta_0 z_0}{\lambda_0}}) (y - y^2)^3 e^{\frac{16\pi\eta_0 z_0 y(1-y)}{\lambda_0}},$$

which can be recast into the remarkably simple form:

$$\frac{d\Gamma/dy|_{pl}}{d\Gamma/dy|_{fs}} = \frac{1}{2} F_p(y) F_p(1 - y).$$

# Appendix C

## Supplementary Materials for: Turning Forbidden Transitions into Dominant Transitions

### C.1 Introduction

In this appendix, we derive some results regarding the coupling of atomic emitters to the phonon-polaritons characteristic of polar crystals such as hBN and SiC. In particular, we consider atom-field interactions governed by the non-relativistic Pauli-Schrodinger Hamiltonian  $H$ :

$$H = H_a + H_{em} + H_{int}$$
$$H_a = \left( \sum_i \frac{\mathbf{p}_i^2}{2m_e} - \frac{e^2}{4\pi\epsilon_0 r_i} \right) \quad (\text{C.1})$$

$$H_{em} = \sum_k \int d\mathbf{r} \int d\omega \hbar\omega \left( f_k^\dagger(\mathbf{r}, \omega) f_k(\mathbf{r}, \omega) + \frac{1}{2} \right)$$
$$H_{int} = \sum_i \frac{e}{2m} (\mathbf{p}_i \cdot \mathbf{A}(\mathbf{r}_i) + \mathbf{A}(\mathbf{r}_i) \cdot \mathbf{p}_i) + \frac{e^2}{2m} \mathbf{A}^2(\mathbf{r}_i), \quad (\text{C.2})$$

$H_a$  is the atomic Hamiltonian,  $H_{int}$  is the atom-field interaction,  $\mathbf{A}$  is the vector potential operator, and  $\mathbf{B}$  is the magnetic field operator. The minimal-coupling interaction Hamiltonian presented above is related to the more well-known dipole interaction Hamiltonian:  $-\mathbf{d} \cdot \mathbf{E}$  + self-energy, by a unitary transformation in the long-wavelength (dipole) approximation[79]. The approach that we take takes losses fully into account via the formalism of macroscopic QED. The primary physical difference between QED with losses and QED without losses lies in the elementary excitations. In the lossless formalism, the excitations can be seen as quanta of electromagnetic modes. In the lossy formalism, the excitations cannot be seen as quanta of electromagnetic modes because the modes are ill-defined. Rather, the elementary excitations are dipoles which are induced in the material. These excitations are characterized by position, frequency, and orientation.

The vector potential operator in the framework of macroscopic QED is given by:

$$A_i(\mathbf{r}) = \sqrt{\frac{\hbar}{\pi\epsilon_0}} \int d\omega' \frac{\omega'}{c^2} \int d\mathbf{r}' \sqrt{\text{Im } \epsilon(\mathbf{r}', \omega')} \mathbf{G}_{ij}(\mathbf{r}, \mathbf{r}'; \omega') \hat{f}_j(\mathbf{r}', \omega') + \text{H.c.}, \quad (\text{C.3})$$

where  $\mathbf{G}_{ij}$  is the dyadic Green function of the Maxwell equations, satisfying  $\nabla \times \nabla \times \mathbf{G}_i - \epsilon(\mathbf{r}, \omega) \frac{\omega^2}{c^2} \mathbf{G}_i = \delta(\mathbf{r} - \mathbf{r}') \hat{e}_i$ .  $\hat{f}_j^{(\dagger)}(\mathbf{r}, \omega)$  annihilates (creates) a lossy excitation of frequency  $\omega$ , at position  $\mathbf{r}$ , and in direction  $j$ . It satisfies bosonic commutation relations, namely:  $[\hat{f}_i(\mathbf{r}, \omega), \hat{f}_j^\dagger(\mathbf{r}', \omega')] = \delta_{ij} \delta(\omega - \omega') \delta(\mathbf{r} - \mathbf{r}')$ . When applying the Fermi Golden Rule, the initial state is  $|e, 0\rangle$ , while the final states are of the form  $|g, \mathbf{x}\omega k\rangle \equiv \hat{f}_k^\dagger(\mathbf{x}, \omega) |g, 0\rangle$  [106].

## C.2 Optical Response of Phonon-Polariton Materials

As prescribed by Equation (2), we must compute the Green function of a phonon-polariton supporting system. The simplest computation involves invoking the excellent approximation that the wavevector of the phonon polaritons emitted is much larger than the photon wavelength  $\frac{\omega}{c}$ . This is the electrostatic limit. In such a limit, the electric field is approximately longitudinal, i.e;  $\mathbf{E} = -\nabla\phi$ , where  $\phi$  satisfies the Laplace equation:  $\partial_i\epsilon_{ij}(\omega)\partial_j\phi = 0$ . The Green function for the potential  $G_\phi(\mathbf{r}, \mathbf{r}', \omega)$  is defined by:  $\partial_i\epsilon_{ij}(\omega)\partial_j G_\phi(\mathbf{r}, \mathbf{r}', \omega) = \delta(\mathbf{r} - \mathbf{r}')$  and is related to the Green function for the electric field (defined in the previous paragraph),  $G_{ij}^E(\mathbf{r}, \mathbf{r}', \omega)$ , by:

$$G_{ij}^E(\mathbf{r}, \mathbf{r}', \omega) = -\frac{c^2}{\omega^2}\partial_i\partial_j G_\phi(\mathbf{r}, \mathbf{r}', \omega)$$

We can compute the Green function for an both an anisotropic and an isotropic polar crystal at the same with the same methods. Expressing the Green function for the potential as  $\frac{1}{(2\pi)^2}\int d\mathbf{q} c(q, z)e^{i\mathbf{q}\cdot\rho}$ , where  $\rho \equiv (x, y)$ , and  $c(q, z)$  is of the form indicated in Figure S1. Solving the boundary value problem, and identifying  $c_{2t}$  as  $r_p$ , it can be shown that  $r_p$  is given by:

$$r_p = \frac{e^{2dq}(\epsilon - 1)(\epsilon_s + \epsilon) + (\epsilon + 1)(\epsilon_s - \epsilon)}{e^{2dq}(\epsilon + 1)(\epsilon_s + \epsilon) + (\epsilon - 1)(\epsilon_s - \epsilon)}, \quad (\text{C.4})$$

in the case of an isotropic polar dielectric and

$$r_p = \frac{(\sqrt{r}\epsilon + i)(\epsilon_s + i\sqrt{r}\epsilon)e^{2iq\sqrt{r}t} + (\sqrt{r}\epsilon - i)(\epsilon_s - i\sqrt{r}\epsilon)}{(\sqrt{r}\epsilon - i)(\epsilon_s + i\sqrt{r}\epsilon)e^{2iq\sqrt{r}t} + (\sqrt{r}\epsilon + i)(\epsilon_s - i\sqrt{r}\epsilon)} \quad (\text{C.5})$$

in the case of a hyperbolic polar dielectric in the RS bands where  $r$  is the absolute value of the anisotropy ratio, defined by  $r = \left|\frac{\epsilon_\perp}{\epsilon_\parallel}\right|$ . The location of the poles of the

imaginary part of the reflectivity in  $(\omega, q)$  space gives the dispersion relation  $\omega(q)$ . When losses are present,  $\text{Im } r_p$  is centered around the dispersion relation, as shown in Figure S1.

### C.2.1 Lossless Limit: Effective Mode Expansion

Although all of the decay rates that we compute can be computed through this Green function formalism, it is difficult from this formalism to extract information such as the angular spectrum of emitted polaritons. The reason for this is that concepts like the angular spectrum assume emission into well-defined modes with some propagation direction. But when losses are present, modes are ill-defined. Therefore, we need to make use of a different formalism to capture the emission into propagating phonon polaritons and to thus derive the angular spectrum of entangled photons. It is known that in lossless dielectrics, the vector potential can be expressed in the form of a mode expansion:

$$\mathbf{A} = \sum_n \sqrt{\frac{\hbar}{2\epsilon_0\omega_n}} (\mathbf{E}_n a_n + hc),$$

where the  $\mathbf{E}_n$  are the orthonormal modes of the Maxwell equations, normalized such that  $\int d\mathbf{r} \epsilon |\mathbf{E}|^2 = 1$ . In a manuscript of ours (see Reference 4 of Appendix D), it was shown by taking the Green function formalism in the lossless limit that an effective mode expansion can be derived for polaritons, where the second quantization operators for the modes satisfy canonical commutation relations provided that the field modes are normalized such that:

$$\frac{1}{2\omega} \int d\mathbf{r} \mathbf{E}^*(\mathbf{r}) \cdot \frac{d(\epsilon_r \omega^2)}{d\omega} \cdot \mathbf{E}(\mathbf{r}) = \frac{\hbar\omega}{2\epsilon_0}.$$

With all of this set up, we find that the mode expansion of the vector potential in the lossless limit is given by:



$$\mathbf{A} = \sum_{\mathbf{q}} \sqrt{\frac{\hbar q}{2\epsilon_0 \omega_n N_q}} (e^{i\mathbf{q}\cdot\rho - qz} \hat{\mathbf{e}}_{\theta} a_n + hc); \quad z > 0 \quad (\text{C.6})$$

We use this equation to compute the angular spectrum of emitted radiation in Section IV. I.

### C.3 Macroscopic QED of PhPs at First Order in Perturbation Theory

It [87], it was shown that the decay rate for a transition of any multipolar order including losses is given by:

$$\Gamma = \frac{2e^2}{\hbar\epsilon_0 m_e^2 \omega_0^2} \frac{1}{(2\pi)^2} \int d\mathbf{q} \, q |\langle g | (\hat{\mathbf{e}}(\mathbf{q}) \cdot \mathbf{p}) e^{i\mathbf{q}\cdot\rho - qz} | e \rangle|^2 \text{Im} \, r_p,$$

where  $r_p$  is the p-polarized complex reflectivity of the air-polar dielectric-substrate system.

The calculations for multipolar transition rates presented in the main text are for the case in which the initial and final wavefunctions have their z-projected angular momentum to be zero (i.e;  $m_i = m_f = 0$ ). In this case, the angular integral is simply  $2\pi$ , and we can pick  $\mathbf{q}$  to be in a particular direction, called  $x$ . Frequently, it is the case that in the matrix element in Equation (S5) there is one main contributing term from the series expansion of the exponential. That is to say:

$$\left| \langle e | e^{q(-ix - (z-z_0))} \hat{\mathbf{e}}_{\theta}^* \cdot \nabla | g \rangle \right|^2 = C_n q^{2(n-1)}$$

where  $n = 1$  for dipole (E1) transitions,  $n = 2$  for quadrupole(E2) transitions, and so

on, meaning that the decay rates are given by

$$\Gamma = \frac{e^2}{\pi \hbar \epsilon_0 m_e^2 \omega_0^2} C_n \int dq q^{2n} e^{-2qz_0} \text{Im } r_p(q, \omega_0). \quad (\text{C.7})$$

## C.4 Macroscopic QED at Higher Order in Perturbation Theory: Emission of N Polaritons

In this section, we derive the frequency spectra of spontaneous emission of  $N$  excitations of the lossy electromagnetic field. We then consider as special cases  $N = 2$  and  $N = 3$ . These results fully incorporate losses and elucidate the contribution of quenching and intercombination of quenching and polariton launching to the decay of an excited emitter. The derivation proceeds by application of the Fermi Golden rule at  $N$ -th order in perturbation as applied to transitions between an initial state  $|i_N, 0\rangle$  and a continuum of final states with  $N$  excitations of the lossy electromagnetic field, i.e.,  $|i_0, \mathbf{x}_1 \omega_1 k_1 \dots \mathbf{x}_N \omega_N k_N\rangle$ . The Fermi Golden Rule reads for this process:

$$\Gamma = \frac{2\pi}{\hbar^2 N!} \prod_{i=1}^N \left( \int d\mathbf{x}_i \int d\omega_i \sum_{k_i} \right) \left| \sum_{i_1 \dots i_{N-1}} V_{i_N, i_{N-1}} \prod_{k=1}^{N-1} \frac{V_{i_k, i_{k-1}}}{E_{i_0} - E_{i_k}} \right|^2 \delta \left( \omega_0 - \sum_{i=1}^N \omega_i \right), \quad (\text{C.8})$$

where  $i_0$  denotes an initial electronic state and  $i_N$  denotes a final electronic state. For simplicity, we take the perturbation operator  $V$  to be the dipole operator  $-\mathbf{d} \cdot \mathbf{E}$ . An interesting quantity is the spectrum of radiation, which tells us the probability of emitting an entangled  $N$ -tuple of polaritons at frequencies  $(\omega_1, \omega_2, \dots, \omega_N)$ . Since one of the polariton frequencies is fixed by energy conservation, we have that:

$$\frac{d\Gamma}{d\omega_1 \dots d\omega_{N-1}} = \frac{2\pi}{\hbar^2 N!} \prod_{i=1}^N \left( \int d\mathbf{x}_i \sum_{k_i} \right) \left| \sum_{i_1 \dots i_{N-1}} V_{i_N, i_{N-1}} \prod_{k=1}^{N-1} \frac{V_{i_k, i_{k-1}}}{E_{i_0} - E_{i_k}} \right|^2$$

where it is understood that  $\omega_N = \omega_0 - \sum_{i=1}^{N-1} \omega_i$ . The sum over intermediate states  $i_1 \dots i_{N-1}$  includes both electronic and electromagnetic degrees of freedom. Denoting the atomic degrees of freedom as  $n_i$ , we have that for a fixed set of electronic intermediate states  $\{n_1 \dots n_{N-1}\}$  that there are  $N!$  terms corresponding to the different orderings of the intermediate excitations of the electromagnetic field. This is an important point of simplification because it means that same the electromagnetic terms appear in each term of the sum, even when we can vary the electronic degrees of freedom, meaning that they can be factored out. This is the crucial simplification of this expression because it will allow us to connect the spectrum of N-excitation emission processes to the Purcell factor of a dipole at each frequency by which a photon is emitted.

To proceed, we will use three identities:

1.

$$\begin{aligned} V_{i_j, i_{j-1}} &= \langle n_j, \mathbf{x}_j \omega_j k_j, \mathbf{x}_{j-1} \omega_{j-1} k_{j-1}, \dots, \mathbf{x}_1 \omega_1 k_1 | d_i E_i | n_{j-1}, \mathbf{x}_{j-1} \omega_{j-1} k_{j-1}, \dots, \mathbf{x}_1 \omega_1 k_1 \rangle \\ &= i \sqrt{\frac{\hbar}{\pi \epsilon_0}} d_{i_j}^{n_j, n_{j-1}} \frac{\omega_j^2}{c^2} \sqrt{\text{Im } \epsilon(\mathbf{x}_j), \omega_j} G_{i_j, k_j}^*(\mathbf{r}_0, \mathbf{x}_j, \omega_j), \end{aligned} \quad (\text{C.9})$$

2.

$$\frac{\omega^2}{c^2} \int d\mathbf{r} \text{Im } \epsilon(\mathbf{r}, \omega) (GG^\dagger)(\mathbf{r}_0, \mathbf{r}, \omega) = \text{Im } G(\mathbf{r}_0, \mathbf{r}_0, \omega)$$

3. For a dipole polarized in the z-direction and a material which is uniform in the xy-plane:

$$\text{Im } G_{ij}(\mathbf{r}_0, \mathbf{r}_0, \omega) = \frac{\omega}{3\pi c} F_p(\mathbf{r}_0, \mathbf{r}_0, \omega) D_{ij},$$

where  $D = \text{diag}(1/2, 1/2, 1)$  and  $F_p$  is the Purcell factor for one-photon emission for the z-polarized dipole (frequency  $\omega$  and position  $\mathbf{r}_0$ ) near this material .

Defining the sum over permutations and intermediate states as  $T_{i_1, \dots, i_N}$ , and  $E =$

$\hbar\omega_0 y$ , and using the three facts above, we have finally that

$$\frac{d\Gamma}{dy_1 \dots dy_{N-1}} = \frac{2\pi\omega_0}{N!} \left(\frac{2}{3\pi}\right)^N \alpha^N k_0^{2N} \left[ \prod_{i=1}^N y_i^3 F_p(y_i) \right] \sum_{i_1 \dots i_N} D_{i_1 i_1} \dots D_{i_N i_N} |T_{i_1 \dots i_N}(y_1 \dots y_N)|^2 \quad (\text{C.10})$$

From this result, we can easily read off a general and highly intuitive claim that the enhancement of the spectrum at some set of frequencies is proportional to the enhancement of emission at each of those frequencies.

#### C.4.1 N=2 and the Angular Spectrum of Emitted Radiation.

In the special case where two lossy excitations are emitted, we arrive at:

$$\frac{d\Gamma}{dy} = \pi\omega_0 \left(\frac{2}{3\pi}\right)^2 \alpha^2 k_0^4 y^3 (1-y)^3 F_p(y) F_p(1-y) \sum_{ij} D_{ii} D_{jj} |T_{ij}|^2 \quad (\text{C.11})$$

We focus on the case in which the transition is between two  $s$  states. In that case, only the  $xx$ ,  $yy$ , and  $zz$  terms are relevant of  $T_{ij}$  meaning that the above sum over  $i, j$  becomes  $\frac{3}{2}T_{zz}$ , making emission rate for two lossy excitations:

$$\frac{d\Gamma}{dy} = \frac{2}{3\pi} \omega_0^2 \alpha^2 k_0^4 y^3 (1-y)^3 F_p(y) F_p(1-y) |T_{zz}|^2 \quad (\text{C.12})$$

Using the fact that the free-space differential decay rate is given by [115]:

$$\frac{4}{3\pi} \alpha^2 k^4 y^3 (1-y)^3 |T_{zz}|^2,$$

it follows that the spectral enhancement (defined in the main text) is:

$$\frac{\frac{d\Gamma}{d\omega}}{\frac{d\Gamma_0}{d\omega}} = \frac{1}{2} F_p(\omega) F_p(\omega_0 - \omega) \quad (\text{C.13})$$

The expression for the two lossy excitation differential decay rate derived by taking

the  $N=2$  case of our  $N$ -photon emission formula is consistent with one that we derived in the specific context of two-plasmon spontaneous emission for 2D plasmons [87].

Now, we focus on computing the angular spectrum of radiation of phonon-polaritons emitted by an excited atomic electron. In other words, we want the quantity

$$S(\omega, \theta, \theta') \equiv \frac{d\Gamma}{d\omega d\theta d\theta'}.$$

Because we want to focus only on excitation of propagating polaritons and not loss-excitations, we extract the pole contribution from the imaginary part of the p-polarized reflectivity. This is equivalent to writing field operators in the lossless limit. This was done in Sec. II. A. Writing the second-order Fermi Golden Rule for the transition rate between an initial state  $|e, 0\rangle$  and the continuum of final states  $|g, \mathbf{q}\mathbf{q}'\rangle$ , we see that:

$$\frac{d\Gamma}{d\omega d\theta d\theta'} = \frac{1}{16\pi^3 \hbar^2} \frac{q(\omega)q(\omega_0 - \omega)}{v_g(\omega)v_g(\omega_0 - \omega)} \left| \sum_{i_1} \frac{\langle g, \mathbf{q}\mathbf{q}' | \mathbf{d} \cdot \mathbf{E} | i_1 \rangle \langle i_1 | \mathbf{d} \cdot \mathbf{E} | e, 0 \rangle}{E_i - E_{i_1} + i0^+} \right|^2,$$

where  $v_g$  is the group velocity,  $\frac{d\omega}{dq}$ . Inserting the definition of the operators, we find that the spectrum is given by:

$$S(\omega, \theta, \theta') = \frac{\alpha^2 c^2}{4\pi} \omega(\omega_0 - \omega) \frac{q(\omega)q(\omega_0 - \omega)}{v_g(\omega)v_g(\omega_0 - \omega)} \left| F_{\mathbf{q}}^{*i} F_{\mathbf{q}'}^{*j} T_{ij} \right|^2 \quad (\text{C.14})$$

where

$$T_{ij}(\omega) = \sum_n \frac{x_j^{gn} x_i^{ne}}{\omega_i - \omega_n - \omega} + \frac{x_i^{gn} x_j^{ne}}{\omega_i - \omega_n - (\omega_0 - \omega)} = T_{ji}(\omega_0 - \omega).$$

We now use this to extract the form of the angular spectrum of entangled photons as a function of the electronic orbitals participating in the transition. To give the reader a sense of how much tunability there is in varying the angular spectrum, we consider four cases. In all four, the final states are  $s$  states. But the initial states will be taken to be  $s$ ,  $d_{xy}$ ,  $d_{yz}$ , and  $d_{xz}$  states.

$s \rightarrow s$

In the case where the initial state is an  $s$  state, we have that  $T_{ij} = 0$  if  $i \neq j$ . This is because of the dipole approximation, which fixes the intermediate state to be a  $p$  state. Therefore, if  $i \neq j$ , then  $T_{ij}$  has a sum of terms like  $\langle s|x_i|p_k\rangle\langle p_k|x_j|s\rangle$ , where  $p_k = p_x, p_y, p_z$ . Each of these terms individually vanishes, and so the entire tensor vanishes. Moreover  $T_{xx} = T_{yy} = T_{zz} \equiv T$  because  $\langle p_x|x|s\rangle = \langle p_y|y|s\rangle = \langle p_z|z|s\rangle$ . Therefore:

$$S(\omega, \theta, \theta') = |T|^2 (\cos \theta \cos \theta' + \sin \theta \sin \theta' - 1)^2 = 4|T|^2 \sin^4 \left( \frac{\theta - \theta'}{2} \right) \cdot (s \rightarrow s) \quad (\text{C.15})$$

$d_{xy} \rightarrow s$

In the case where the initial state is  $d_{xy}$ , the only contributing terms are  $T_{xy}$  and  $T_{yx}$ . The argument for this statement makes use of the fact that the  $d_{xy}$  has an angular dependence that can be written in Cartesian coordinates as  $xy$ . We start proving this claim by examining the  $T_{zi}$  components. If one of the indices is  $z$ , then it will either be the case that the intermediate state must be a  $p_z$  state (to have overlap with the  $s$  state), or that there will be a matrix element of the form  $\langle p_i|z|d_{xy}\rangle$ . The first case gives zero because  $d_{xy}$  has no transition dipole moment with  $z$ . The second case also gives zero because  $d_{xy}$  has no  $z$ -polarized dipole moment with any  $p$  orbital. Thus the  $T_{zi}$  components vanish. The  $T_{xx}$  and  $T_{yy}$  components also vanish because  $d_{xy}$  has no  $(x,y)$ -polarized dipole moment with  $p_{x,y}$ . Therefore:

$$S(\omega, \theta, \theta') = (T_{xy}(\omega) \cos \theta \sin \theta' + T_{xy}(\omega_0 - \omega) \sin \theta \cos \theta')^2 \cdot (d_{xy} \rightarrow s) \quad (\text{C.16})$$

$d_{xz} \rightarrow s$  **and**  $d_{yz} \rightarrow s$

A nearly identical argument to the one above (replace all y's with z's or all x's with z's) yields:

$$S(\omega, \theta, \theta') = (T_{xz}(\omega) \cos \theta + T_{xz}(\omega_0 - \omega) \cos \theta')^2. (d_{xz} \rightarrow s) \quad (\text{C.17})$$

$$S(\omega, \theta, \theta') = (T_{yz}(\omega) \sin \theta + T_{yz}(\omega_0 - \omega) \sin \theta')^2. (d_{yz} \rightarrow s) \quad (\text{C.18})$$





# Bibliography

- [1] Chia Wei Hsu, Bo Zhen, A. Douglas Stone, John D. Joannopoulos, and Marin Soljačić. Bound states in the continuum. Submitted.
- [2] von Neumann J. and Wigner E. Uber merkwurdige diskrete eigenwerte. *Phys. Z.*, 30:465–467, 1929.
- [3] Friedrich H. and Wintgen D. Interfering resonances and bound states in the continuum. *Phys. Rev. A*, 32:3231–3242, 1985.
- [4] M. Robnik. A simple separable hamiltonian having bound states in the continuum. *J. Phys. A*, 19(18):3845, 1986.
- [5] J.U. Nockel. Resonances in quantum-dot transport. *Phys. Rev. B*, 46(23):15348, 1992.
- [6] P. Duclos, P. Exner, and B. Meller. Open quantum dots: resonances from perturbed symmetry and bound states in strong magnetic fields. *Reports on Mathematical Physics*, 47(2):253–267, 2001.
- [7] Prodanovic N., Milanovic V., Ikonc Z., Indjin D., and Harrison P. Bound states in continuum: quantum dots in a quantum well. *Phys. Lett. A*, 377:2177–2181, 2013.
- [8] M.L.L De Guevara, F. Claro, and P.A. Orellana. Ghost Fano resonance in a double quantum dot molecule attached to leads. *Phys. Rev. B*, 67(19):195335, 2003.
- [9] G. Ordóñez, K. Na, and S. Kim. Bound states in the continuum in quantum-dot pairs. *Phys. Rev. A*, 73(2):022113, 2006.
- [10] N. Moiseyev. Suppression of feshbach resonance widths in two-dimensional waveguides and quantum dots: a lower bound for the number of bound states in the continuum. *Phys. Rev. Lett.*, 102(16):167404, 2009.
- [11] T Ochiai and K Sakoda. Dispersion relation and optical transmittance of a hexagonal photonic crystal slab. *Phys. Rev. B*, 63(12):125107, 2001.
- [12] Ctyroky J. Photonic bandgap structures in planar waveguides. *J. Opt. Soc. Am. A*, 18:435–441, 2001.

- [13] Watts M. R., Johnson S. G., Haus H. A., and Joannopoulos J. D. Electromagnetic cavity with arbitrary Q and small modal volume without a complete photonic bandgap. *Opt. Lett.*, 27:1785–1787, 2001.
- [14] Kawakami S. Analytically solvable model of photonic crystal structures and novel phenomena. *J. Lightwave Tech.*, 20:1644–1650, 2002.
- [15] V.M. Apalkov and M.E. Raikh. Strongly localized mode at the intersection of the phase slips in a photonic crystal without band gap. *Phys. Rev. Lett.*, 90(25):253901, 2003.
- [16] S.P. Shipman and S. Venakides. Resonant transmission near non-robust periodic slab modes. *Phys. Rev. E*, 71(1):026611–1, 2005.
- [17] R. Porter and D.V. Evans. Embedded Rayleigh–Bloch surface waves along periodic rectangular arrays. *Wave motion*, 43(1):29–50, 2005.
- [18] E.N. Bulgakov and A.F. Sadreev. Bound states in the continuum in photonic waveguides inspired by defects. *Phys. Rev. B*, 78(7):075105, 2008.
- [19] D.C. Marinica, A.G. Borisov, and S.V. Shabanov. Bound states in the continuum in photonics. *Phys. Rev. Lett.*, 100(18):183902, 2008.
- [20] M.I. Molina, A.E. Miroschnichenko, and Y.S. Kivshar. Surface bound states in the continuum. *Phys. Rev. Lett.*, 108(7):070401, 2012.
- [21] C.W. Hsu, B. Zhen, S-L. Chua, S.G. Johnson, J.D. Joannopoulos, and M. Soljačić. Bloch surface eigenstates within the radiation continuum. *Light: Science & Applications*, 2:e84, 2013.
- [22] E.N. Bulgakov and A.F. Sadreev. Bloch bound states in the radiation continuum in a periodic array of dielectric rods. *Phys. Rev. A*, 90(5):053801, 2014.
- [23] F. Monticone and A. Alù. Embedded photonic eigenvalues in 3d nanostructures. *Phys. Rev. Lett.*, 112(21):213903, 2014.
- [24] E. N. Bulgakov and A. F. Sadreev. Robust bound state in the continuum in a nonlinear microcavity embedded in a photonic crystal waveguide. *Opt. Lett.*, 39(17):5212–5215, Sep 2014.
- [25] P.J. Cobelli, V. Pagneux, A. Maurel, and P. Petitjeans. Experimental study on water-wave trapped modes. *Journal of Fluid Mechanics*, 666:445–476, 2011.
- [26] Y. Plotnik *et. al.* Experimental observation of optical bound states in the continuum. *Phys. Rev. Lett.*, 107(18):183901, 2011.
- [27] J. Lee *et. al.* Observation and differentiation of unique high-Q optical resonances near zero wave vector in macroscopic photonic crystal slabs. *Phys. Rev. Lett.*, 109(6):067401, 2012.

- [28] C.W. Hsu *et. al.* Observation of trapped light within the radiation continuum. *Nature*, 499:188–191, 2013.
- [29] G. Corrielli, G. Della Valle, A. Crespi, R. Osellame, and S. Longhi. Observation of surface states with algebraic localization. *Phys. Rev. Lett.*, 111(22):220403, 2013.
- [30] S. Weimann *et. al.* Compact surface Fano states embedded in the continuum of waveguide arrays. *Phys. Rev. Lett.*, 111(24):240403, 2013.
- [31] T. Lepetit and B. Kanté. Controlling multipolar radiation with symmetries for electromagnetic bound states in the continuum. *Phys. Rev. B*, 90(24):241103, 2014.
- [32] J. Fleischer *et. al.* Spatial photonics in nonlinear waveguide arrays. *Optics express*, 13(6):1780–1796, 2005.
- [33] T. Schwartz, G. Bartal, S. Fishman, and M. Segev. Transport and anderson localization in disordered two-dimensional photonic lattices. *Nature*, 446(7131):52–55, 2007.
- [34] B. Freedman, G. Bartal, M. Segev, R. Lifshitz, D.N. Christodoulides, and J.W. Fleischer. Wave and defect dynamics in nonlinear photonic quasicrystals. *Nature*, 440(7088):1166–1169, 2006.
- [35] J.W. Fleischer, M. Segev, N.K. Efremidis, and D.N. Christodoulides. Observation of two-dimensional discrete solitons in optically induced nonlinear photonic lattices. *Nature*, 422(6928):147–150, 2003.
- [36] Mikael C Rechtsman, Julia M Zeuner, Andreas Tünnermann, Stefan Nolte, Mordechai Segev, and Alexander Szameit. Strain-induced pseudomagnetic field and photonic landau levels in dielectric structures. *Nature Photonics*, 7(2):153–158, 2013.
- [37] Mikael C Rechtsman, Julia M Zeuner, Yonatan Plotnik, Yaakov Lumer, Daniel Podolsky, Felix Dreisow, Stefan Nolte, Mordechai Segev, and Alexander Szameit. Photonic floquet topological insulators. *Nature*, 496(7444):196–200, 2013.
- [38] I. Bloch. Ultracold quantum gases. *Nat. Phys.*, 1(1):23–30, 10 2005.
- [39] K. Henderson, C. Ryu, C. MacCormick, and M.G. Boshier. Experimental demonstration of painting arbitrary and dynamic potentials for bose–einstein condensates. *New Journal of Physics*, 11(4):043030, 2009.
- [40] Paul AM Dirac. The quantum theory of the emission and absorption of radiation. In *Proceedings of the Royal Society of London A: Mathematical, Physical and Engineering Sciences*, volume 114, pages 243–265. The Royal Society, 1927.

- [41] Matthew Pelton. Modified spontaneous emission in nanophotonic structures. *Nature Photonics*, 9(7):427–435, 2015.
- [42] MS Tame, KR McEnery, ŞK Özdemir, J Lee, SA Maier, and MS Kim. Quantum plasmonics. *Nature Physics*, 9(6):329–340, 2013.
- [43] RH Friend, RW Gymer, AB Holmes, JH Burroughes, RN Marks, CDDC Taliani, DDC Bradley, DA Dos Santos, JL Bredas, M Lögdlund, et al. Electroluminescence in conjugated polymers. *Nature*, 397(6715):121–128, 1999.
- [44] A Köhler and H Bässler. Triplet states in organic semiconductors. *Materials Science and Engineering: R: Reports*, 66(4):71–109, 2009.
- [45] Maria Göppert. Über die wahrscheinlichkeit des zusammenwirkens zweier lichtquanten in einem elementarakt. *Naturwissenschaften*, 17(48):932–932, 1929.
- [46] Claudio L Cesar, Dale G Fried, Thomas C Killian, Adam D Polcyn, Jon C Sandberg, A Yu Ite, Thomas J Greytak, Daniel Kleppner, and John M Doyle. Two-photon spectroscopy of trapped atomic hydrogen. *Physical review letters*, 77(2):255, 1996.
- [47] Alex Hayat, Pavel Ginzburg, and Meir Orenstein. Observation of two-photon emission from semiconductors. *Nature photonics*, 2(4):238–241, 2008.
- [48] Amir Nevet, Nikolai Berkovitch, Alex Hayat, Pavel Ginzburg, Shai Ginzach, Ofir Sorias, and Meir Orenstein. Plasmonic nanoantennas for broadband enhancement of two-photon emission from semiconductors. *Nano letters*, 10(5):1848–1852, 2010.
- [49] Alex Hayat, Amir Nevet, Pavel Ginzburg, and Meir Orenstein. Applications of two-photon processes in semiconductor photonic devices: invited review. *Semiconductor Science and Technology*, 26(8):083001, 2011.
- [50] Tadaaki Nagao, Torsten Hildebrandt, Martin Henzler, and Shuji Hasegawa. Dispersion and damping of a two-dimensional plasmon in a metallic surface-state band. *Physical review letters*, 86(25):5747, 2001.
- [51] Bogdan Diaconescu, Karsten Pohl, Luca Vattuone, Letizia Savio, Philip Hofmann, Vyacheslav M Silkin, Jose M Pitarke, Eugene V Chulkov, Pedro M Echenique, Daniel Farías, et al. Low-energy acoustic plasmons at metal surfaces. *Nature*, 448(7149):57–59, 2007.
- [52] Yu Liu, RF Willis, KV Emtsev, and Th Seyller. Plasmon dispersion and damping in electrically isolated two-dimensional charge sheets. *Physical Review B*, 78(20):201403, 2008.

- [53] EP Rugeramigabo, T Nagao, and H Pfnür. Experimental investigation of two-dimensional plasmons in a dysi 2 monolayer on si (111). *Physical Review B*, 78(15):155402, 2008.
- [54] Marinko Jablan, Hrvoje Buljan, and Marin Soljačić. Plasmonics in graphene at infrared frequencies. *Physical review B*, 80(24):245435, 2009.
- [55] Sung Jin Park and Richard E. Palmer. Acoustic plasmon on the au(111) surface. *Phys. Rev. Lett.*, 105:016801, 2010.
- [56] AN Grigorenko, Marco Polini, and KS Novoselov. Graphene plasmonics. *Nature photonics*, 6(11):749–758, 2012.
- [57] Zhe Fei, AS Rodin, GO Andreev, W Bao, AS McLeod, M Wagner, LM Zhang, Z Zhao, M Thiemens, G Dominguez, et al. Gate-tuning of graphene plasmons revealed by infrared nano-imaging. *Nature*, 487(7405):82–85, 2012.
- [58] Marinko Jablan, Marin Soljagic, and Hrvoje Buljan. Plasmons in graphene: fundamental properties and potential applications. *Proceedings of the IEEE*, 101(7):1689–1704, 2013.
- [59] KJ Tielrooij, L Orona, A Ferrier, M Badioli, G Navickaite, S Coop, S Nanot, B Kalinic, T Cesca, L Gaudreau, et al. Electrical control of optical emitter relaxation pathways enabled by graphene. *Nature Physics*, 2015.
- [60] Achim Woessner, Mark B Lundeborg, Yuanda Gao, Alessandro Principi, Pablo Alonso-González, Matteo Carrega, Kenji Watanabe, Takashi Taniguchi, Giovanni Vignale, Marco Polini, et al. Highly confined low-loss plasmons in graphene–boron nitride heterostructures. *Nature materials*, 2014.
- [61] Qiming Zhang, Xiangping Li, Md Muntasir Hossain, Yunzhou Xue, Jie Zhang, Jingchao Song, Jingying Liu, Mark D Turner, Shanhui Fan, Qiaoliang Bao, et al. Graphene surface plasmons at the near-infrared optical regime. *Scientific reports*, 4, 2014.
- [62] Zhe Fei, Gregory O Andreev, Wenzhong Bao, Lingfeng M Zhang, Alexander S. McLeod, Chen Wang, Margaret K Stewart, Zeng Zhao, Gerardo Dominguez, Mark Thiemens, et al. Infrared nanoscopy of dirac plasmons at the graphene–sio2 interface. *Nano letters*, 11(11):4701–4705, 2011.
- [63] A Kramida, Yu Ralchenko, J Reader, et al. Nist atomic spectra database (ver. 5.0). *National Institute of Standards and Technology, Gaithersburg, MD*, 2012.
- [64] Jorge R Zurita-Sánchez and Lukas Novotny. Multipolar interband absorption in a semiconductor quantum dot. i. electric quadrupole enhancement. *JOSA B*, 19(6):1355–1362, 2002.

- [65] Jorge R Zurita-Sánchez and Lukas Novotny. Multipolar interband absorption in a semiconductor quantum dot. ii. magnetic dipole enhancement. *JOSA B*, 19(11):2722–2726, 2002.
- [66] Robert Filter, Stefan Mühlig, Toni Eichelkraut, Carsten Rockstuhl, and Falk Lederer. Controlling the dynamics of quantum mechanical systems sustaining dipole-forbidden transitions via optical nanoantennas. *Physical Review B*, 86(3):035404, 2012.
- [67] Mai Takase, Hiroshi Ajiki, Yoshihiko Mizumoto, Keiichiro Komeda, Masanobu Nara, Hideki Nabika, Satoshi Yasuda, Hajime Ishihara, and Kei Murakoshi. Selection-rule breakdown in plasmon-induced electronic excitation of an isolated single-walled carbon nanotube. *Nature Photonics*, 7(7):550–554, 2013.
- [68] Vassilios Yannopapas and Emmanuel Paspalakis. Giant enhancement of dipole-forbidden transitions via lattices of plasmonic nanoparticles. *Journal of Modern Optics*, 62(17):1435–1441, 2015.
- [69] Mads Lykke Andersen, Søren Stobbe, Anders Søndberg Sørensen, and Peter Lodahl. Strongly modified plasmon-matter interaction with mesoscopic quantum emitters. *Nature Physics*, 7(3):215–218, 2011.
- [70] Ivan D Rukhlenko, Dayan Handapangoda, Malin Premaratne, Anatoly V Fedorov, Alexander V Baranov, and Chennupati Jagadish. Spontaneous emission of guided polaritons by quantum dot coupled to metallic nanowire: Beyond the dipole approximation. *Optics express*, 17(20):17570–17581, 2009.
- [71] Prashant K Jain, Debraj Ghosh, Roi Baer, Eran Rabani, and A Paul Alivisatos. Near-field manipulation of spectroscopic selection rules on the nanoscale. *Proceedings of the National Academy of Sciences*, 109(21):8016–8019, 2012.
- [72] A Freddie Page, Fouad Ballout, Ortwin Hess, and Joachim M Hamm. Nonequilibrium plasmons with gain in graphene. *Physical Review B*, 91(7):075404, 2015.
- [73] Guanxiong Liu, Yanqing Wu, Yu-Ming Lin, Damon B Farmer, John A Ott, John Bruley, Alfred Grill, Phaeton Avouris, Dirk Pfeiffer, Alexander A Balandin, et al. Epitaxial graphene nanoribbon array fabrication using bcp-assisted nanolithography. *ACS nano*, 6(8):6786–6792, 2012.
- [74] Ahmad N Abbas, Gang Liu, Bilu Liu, Luyao Zhang, He Liu, Douglas Ohlberg, Wei Wu, and Chongwu Zhou. Patterning, characterization, and chemical sensing applications of graphene nanoribbon arrays down to 5 nm using helium ion beam lithography. *ACS nano*, 8(2):1538–1546, 2014.
- [75] Gleb M Akselrod, Christos Argyropoulos, Thang B Hoang, Cristian Ciraci, Chao Fang, Jiani Huang, David R Smith, and Maiken H Mikkelsen. Probing the mechanisms of large purcell enhancement in plasmonic nanoantennas. *Nature Photonics*, 2014.

- [76] Thang B Hoang, Gleb M Akselrod, Christos Argyropoulos, Jiani Huang, David R Smith, and Maiken H Mikkelsen. Ultrafast spontaneous emission source using plasmonic nanoantennas. *Nature communications*, 6, 2015.
- [77] Alexandre Archambault, François Marquier, Jean-Jacques Greffet, and Christophe Arnold. Quantum theory of spontaneous and stimulated emission of surface plasmons. *Physical Review B*, 82(3):035411, 2010.
- [78] Frank HL Koppens, Darrick E Chang, and F Javier Garcia de Abajo. Graphene plasmonics: a platform for strong light–matter interactions. *Nano letters*, 11(8):3370–3377, 2011.
- [79] Claude Cohen-Tannoudji, Jacques Dupont-Roc, Gilbert Grynberg, and Patricia Thickstun. *Atom-photon interactions: basic processes and applications*. Wiley Online Library, 1992.
- [80] Harry A Atwater. The promise of plasmonics. *Scientific American*, 296(4):56–62, 2007.
- [81] Martin Moskovits. Surface-enhanced spectroscopy. *Reviews of modern physics*, 57(3):783, 1985.
- [82] Martin Moskovits. Surface-enhanced raman spectroscopy: a brief retrospective. *Journal of Raman Spectroscopy*, 36(6-7):485–496, 2005.
- [83] Martti Kauranen and Anatoly V Zayats. Nonlinear plasmonics. *Nature Photonics*, 6(11):737–748, 2012.
- [84] Hans A Bethe and Edwin E Salpeter. *Quantum mechanics of one-and two-electron atoms*. Springer Science & Business Media, 2012.
- [85] A Rubinowicz. Multipole radiation in atomic spectra. *Reports on progress in physics*, 12(1):233, 1949.
- [86] Edward Uhler Condon and George Hiram Shortley. *The theory of atomic spectra*. Cambridge University Press, 1951.
- [87] Nicholas Rivera, Ido Kaminer, Bo Zhen, John D Joannopoulos, and Marin Soljacic. 2d plasmonics for enabling novel light-matter interactions. *arXiv preprint arXiv:1512.04598*, 2015.
- [88] Alex Hayat, Pavel Ginzburg, and Meir Orenstein. Measurement and model of the infrared two-photon emission spectrum of gaas. *Physical review letters*, 103(2):023601, 2009.
- [89] Yasutomo Ota, Satoshi Iwamoto, Naoto Kumagai, and Yasuhiko Arakawa. Spontaneous two-photon emission from a single quantum dot. *Physical review letters*, 107(23):233602, 2011.

- [90] Vladimir Borisovich Berestetskii, Evgenii Mikhailovich Lifshitz, and Pitaevskii. *Quantum electrodynamics*.
- [91] C Sánchez Muñoz, E Del Valle, A González Tudela, K Müller, S Lichtmanecker, M Kaniber, C Tejedor, JJ Finley, and FP Laussy. Emitters of n-photon bundles. *Nature photonics*, 8(7):550–555, 2014.
- [92] R Hillenbrand, T Taubner, and F Keilmann. Phonon-enhanced light–matter interaction at the nanometre scale. *Nature*, 418(6894):159–162, 2002.
- [93] S Dai, Z Fei, Q Ma, AS Rodin, M Wagner, AS McLeod, MK Liu, W Gannett, W Regan, K Watanabe, et al. Tunable phonon polaritons in atomically thin van der waals crystals of boron nitride. *Science*, 343(6175):1125–1129, 2014.
- [94] Xiaoji G Xu, Jian-Hua Jiang, Leonid Gilburd, Rachel G Rensing, Kenneth S Burch, Chunyi Zhi, Yoshio Bando, Dmitri Golberg, and Gilbert C Walker. Mid-infrared polaritonic coupling between boron nitride nanotubes and graphene. *ACS nano*, 8(11):11305–11312, 2014.
- [95] S Dai, Q Ma, MK Liu, T Andersen, Z Fei, MD Goldflam, M Wagner, K Watanabe, T Taniguchi, M Thiemens, et al. Graphene on hexagonal boron nitride as a tunable hyperbolic metamaterial. *Nature nanotechnology*, 10(8):682–686, 2015.
- [96] S Dai, Q Ma, T Andersen, AS McLeod, Z Fei, MK Liu, M Wagner, K Watanabe, T Taniguchi, M Thiemens, et al. Subdiffractive focusing and guiding of polaritonic rays in a natural hyperbolic material. *Nature communications*, 6, 2015.
- [97] Peining Li, Martin Lewin, Andrey V Kretinin, Joshua D Caldwell, Kostya S Novoselov, Takashi Taniguchi, Kenji Watanabe, Fabian Gaussmann, and Thomas Taubner. Hyperbolic phonon-polaritons in boron nitride for near-field optical imaging and focusing. *Nature communications*, 6, 2015.
- [98] Kaijun Feng, William Streier, SM Islam, Jai Verma, Debdeep Jena, Daniel Wasserman, and Anthony J Hoffman. Localized surface phonon polariton resonances in polar gallium nitride. *Applied Physics Letters*, 107(8):081108, 2015.
- [99] Andrea Tomadin, Alessandro Principi, Justin CW Song, Leonid S Levitov, and Marco Polini. Accessing phonon polaritons in hyperbolic crystals by angle-resolved photoemission spectroscopy. *Physical review letters*, 115(8):087401, 2015.
- [100] Edward Yoxall, Martin Schnell, Alexey Y Nikitin, Oihana Txoperena, Achim Woessner, Mark B Lundberg, Félix Casanova, Luis E Hueso, Frank HL Koppens, and Rainer Hillenbrand. Direct observation of ultraslow hyperbolic polariton propagation with negative phase velocity. *Nature Photonics*, 2015.



- [101] Joshua D Caldwell and Kostya S Novoselov. Van der waals heterostructures: Mid-infrared nanophotonics. *Nature materials*, 14(4):364–366, 2015.
- [102] Joshua D Caldwell, Andrey V Kretinin, Yiguo Chen, Vincenzo Giannini, Michael M Fogler, Yan Francescato, Chase T Ellis, Joseph G Tischler, Colin R Woods, Alexander J Giles, et al. Sub-diffractive volume-confined polaritons in the natural hyperbolic material hexagonal boron nitride. *Nature communications*, 5, 2014.
- [103] Joshua D Caldwell, Orest J Glembocki, Yan Francescato, Nicholas Sharac, Vincenzo Giannini, Francisco J Bezares, James P Long, Jeffrey C Owrutsky, Igor Vurgaftman, Joseph G Tischler, et al. Low-loss, extreme subdiffraction photon confinement via silicon carbide localized surface phonon polariton resonators. *Nano letters*, 13(8):3690–3697, 2013.
- [104] Joshua D Caldwell, Lucas Lindsay, Vincenzo Giannini, Igor Vurgaftman, Thomas L Reinecke, Stefan A Maier, and Orest J Glembocki. Low-loss, infrared and terahertz nanophotonics using surface phonon polaritons. *Nanophotonics*, 4(1), 2015.
- [105] Jacob B Khurgin. How to deal with the loss in plasmonics and metamaterials. *Nature nanotechnology*, 10(1):2–6, 2015.
- [106] Ludwig Knöll, Stefan Scheel, and Dirk-Gunnar Welsch. Qed in dispersing and absorbing media. Technical report, 2000.
- [107] Anshuman Kumar, Tony Low, Kin Hung Fung, Phaedon Avouris, and Nicholas X Fang. Tunable light–matter interaction and the role of hyperbolicity in graphene–hbn system. *Nano letters*, 15(5):3172–3180, 2015.
- [108] John D Joannopoulos, Steven G Johnson, Joshua N Winn, and Robert D Meade. *Photonic crystals: molding the flow of light*. Princeton university press, 2011.
- [109] Stefan Scheel and Stefan Yoshi Buhmann. Macroscopic quantum electrodynamics? concepts and applications. *Acta Phys. Slovaca*, 58(5):675–809, 2008.
- [110] Leon Brillouin. *Wave propagation in periodic structures: electric filters and crystal lattices*. Courier Corporation, 2003.
- [111] Lev Davidovich Landau, JS Bell, MJ Kearsley, LP Pitaevskii, EM Lifshitz, and JB Sykes. *Electrodynamics of continuous media*, volume 8. elsevier, 1984.
- [112] John David Jackson. *Classical electrodynamics*. Wiley, 1999.
- [113] Lukas Novotny and Bert Hecht. *Principles of nano-optics*. Cambridge university press, 2012.

- [114] J Shapiro and G Breit. Metastability of 2 s states of hydrogenic atoms. *Physical Review*, 113(1):179, 1959.
- [115] G Breit and E Teller. Metastability of hydrogen and helium levels. *The Astrophysical Journal*, 91:215, 1940.

# Appendix D

## List of Related Publications

**Manuscripts in Review or Preparation** Chapters 2, 3, and 4 are based on papers 1,2, and 3 listed below, making use of results from 4, and being applied to 5 and 6. Asterisk denotes equal contribution.

1. **N. Rivera\***, I. Kaminer\*, B. Zhen, J. D. Joannopoulos, and M. Soljagic. Shrinking Light to Enable Forbidden Transitions on the Atomic Scale. Mar 2016. Under in-depth review at Science.
2. **N. Rivera**, C.W. Hsu, B. Zhen, H. Buljan, J.D. Joannopoulos, and M. Soljagic. Controlling the Directionality and Dimensionality of Radiation by Perturbing Separable Bound States in the Continuum. Mar 2016. In review at Scientific Reports.
3. **N. Rivera**, I. Kaminer, and M. Soljagic. Ultrahigh Efficiency Access to Forbidden Transitions via Phonon Polaritonics. In preparation.
4. L. Xiao\*, **N. Rivera\***, I. Kaminer, J. Lopez, Energy Distribution of Graphene Plasmons. In preparation.
5. F. Machado, I. Kaminer, **N. Rivera**, and M. Soljagic, 2D Polaritonic Vortices to Tailor Selection Rules. In preparation.

6. C. Murdia, I. Kaminer, **N. Rivera**, L. J. Wong, J.D. Joannopoulos, and M. Soljagic, Controlling Radiation through Shaped Electron Wavefunctions: Monochromatic and Directional Bremsstrahlung Radiation. In preparation.

### **Conference Publications**

1. **Rivera, N.**, Hsu, C.W., Zhen, B., Buljan, H., Joannopoulos, J. and Soljagic, M., 2015, October. Controlling Directionality of Radiation Through Separable Bound States in the Continuum. In *Frontiers in Optics* (pp. FTu3G-4). Optical Society of America. **Presented at Frontiers in Optics 2015**
2. **Rivera, N.**, Kaminer, I., Zhen, B., Joannopoulos, J. and Soljagic, M., 2016, June. Collapse of the Selection Rules Through 2D Plasmonics (pp. STh4Q.3 ). Optical Society of America. **To be Presented at Conference on Lasers and Electro-Optics 2016**
3. **Rivera, N.**, Kaminer, I., Zhen, B., Joannopoulos, J. and Soljagic, M., 2016, June. 2D Plasmonics for Nanosecond Generation of Entangled Plasmon Pairs (pp. FTu1B.1 ). Optical Society of America. **To be Presented at Conference on Lasers and Electro-Optics 2016**